Title
ENERGY SPECTRA AND ANGULAR DEPENDENCES OF NEUTRONS FROM THE 31.5-Mev PROTON BOMBARDMENT OF BERYLLIUM-9, NITROGEN-14, AND ALUMINUM-27

Author
Adelson, Harold E.

Publication Date
1958-12-11

UCRL-8568

Cy.2

University of California

Ernest O. Lawrence Radiation Laboratory

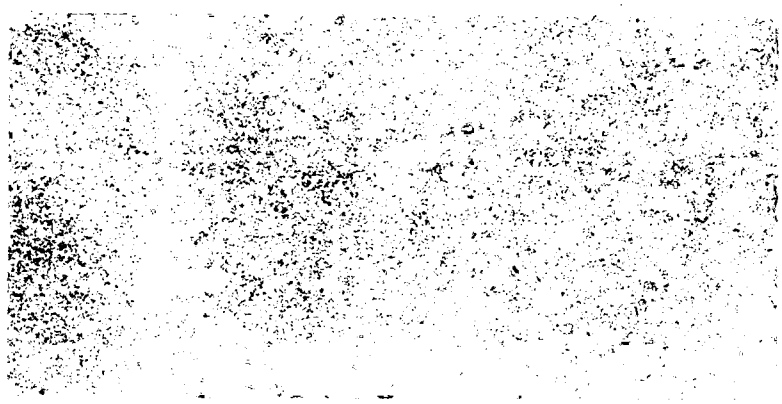

Berkeley, California

DISCLAIMER

UCRL-8568
Physics and Mathematics

UNIVERSITY OF CALIFORNIA

Lawrence Radiation Laboratory
Berkeley, California

Contract No. W-7405-eng-48

ENERGY SPECTRA AND ANGULAR DEPENDENCES OF NEUTRONS FROM THE 31.5-Mev PROTON BOMBARDMENT OF BERYLLIUM-9, NITROGEN-14, AND ALUMINUM-27

Harold E. Adelson

(Thesis)

December 11, 1958

Printed for the U. S. Atomic Energy Commission

Printed in USA. Price $2.75. Available from the
Office of Technical Services
U.S. Department of Commerce
Washington 25, D. C.

Contents

Contents

ENERGY SPECTRA AND ANGULAR DEPENDENCES OF NEUTRONS FROM THE 31.5-Mev PROTON BOMBARDMENT OF BERYLLIUM-9, NITROGEN-14, AND ALUMINUM-27

Harold E. Adelson

Lawrence Radiation Laboratory
University of California
Berkeley, California

December 11, 1958

ABSTRACT

The energy spectra and absolute differential cross sections of neutrons of energy greater than 5 Mev emitted from thin targets of beryllium, nitrogen (melamine), and aluminum bombarded by 31.5-Mev protons were measured at three angles (53°, 90°, and 127°) at the Berkeley linear accelerator. The 4-inch hydrogen bubble chamber was used as a neutron spectrometer. A fast data-reduction system for the analysis of the recoil-proton tracks was developed utilizing a commercial electronic coordinate-measuring device, the IBM punch-card system, and the IBM 650 digital computer. The resolution of the entire spectrometer system was determined by measuring the monoergic (14.1-Mev) neutron spectrum from the $T(d,n)He^4$ reaction. The full width at half maximum of the measured peak was 10% of the peak energy.

The energy spectra from the beryllium and nitrogen bombardments contained structure that may correspond to levels in the residual nuclei of the $Be^9(p,n)B^9$ and $N^{14}(p,n)\,0^{14}$ reactions. Poor statistics did not permit definite level assignments, but several of the possible levels of B^9 correspond to known levels of its mirror nucleus, Be^9.

The angular dependence of the neutron production above 5 Mev from all three targets shows a forward asymmetry. The production from aluminum, which was the heaviest target bombarded, and for which the neutron-production mechanism might be expected to be the compound

model, was in a ratio of 5:3:2 for 53°, 90°, and 127° (lab), respectively. This forward asymmetry is not to be expected from the compound model, and appears to indicate a predominance of the direct-interaction mechanism for the higher-energy neutrons.

I. INTRODUCTION

The investigation of the energy spectra and angular distributions of neutrons resulting from a nuclear reaction is of primary importance in the study of nuclear reaction mechanisms as well as useful in the determination of the properties of nuclear levels. Although it is true that proton spectra are easier to measure and can give valuable insight into the reaction mechanism, it is also true that the Coulomb charge of the proton, which simplifies its detection, at the same time makes the resulting spectra more difficult to interpret. The neutron, on the other hand, has no electrostatic interaction to becloud the fundamental nuclear force effects. It has been only in recent years that neutron spectra in the 10-Mev range have been measured with reasonable resolution. The most accurate work has been conducted with emulsions--with the resulting tedious and lengthy analysis. Recently, electronic counter technique has been used to study elastic and inelastic neutron spectra.

While the energy available for experimentation increased, the theories of reaction mechanisms advanced under the stimulation of the anomalous results of the experiments. The results were in disagreement with the compound-nucleus theory which had been the prevailing and quite successful model of nuclear reactions, especially at resonance energies. This theory, which was first proposed by Bohr,[1] divides the nuclear reaction into two states, (a) the formation of the compound nucleus C, and (b) the disintegration of the compound system into the reaction products. Thus, the reaction may be written $a + A \rightarrow C \rightarrow B + b$, where a is the projectile incident on the target A, B is the residual nucleus, and b is the other reaction product, which is usually detected in the experiment. This separation of the reaction into two parts assumes a short mean free path for the nucleon a inside the nucleus A, so that many nucleon-nucleon collisions occur. The compound nucleus C exists in an excited state whose energy is determined by the binding energy of a to C and the kinetic energy of a. The compound state C will decay eventually when some nucleon b (or group of nucleons such as an alpha particle) accumulates enough energy to be re-emitted. Because of the

time it takes for this energy concentration to occur, the compound system exists for times that are long compared with nuclear traversal time ($\sim 10^{-22}$ second). This theory was successful in explaining nuclear resonance reactions in which the resonance energies were clearly related to nuclear levels of the compound system C. The model predicts that the angular distribution of the reaction products, when the reaction proceeds via a given level in the compound nucleus to a given state in the residual nucleus, will by symmetric around 90°.[2] When one extends the theory to higher energies at which the compound system is excited in a region of many overlapping levels, the statistical approximation is applied,[3] in which it is assumed that the phase relations between the matrix elements of the transitions to and from the compound state are random. This results in an averaging out of the interference terms between different angular-momentum transitions so that the angular distribution of the reaction products is once again symmetric around 90°.[4]

The compound-nucleus theory predicts that for high excitation of the compound system the energy spectrum of nucleon b will have a "Maxwellian" form,[2]

$$I_b(E)dE = \text{const } E\, \sigma_c(E) \exp^{-E/T} dE. \qquad (1)$$

Here $I_b(E)dE$ is the probability of emission of b with energy between E and $E + dE$, σ_c is the cross section for formation of the compound system by the inverse reaction $b + B$, and T is a nuclear "temperature" which characterizes the nuclear level density of the residual nucleus at its maximum excitation. The energy spectrum would be characterized by a peak at energy $E = T$ and would then fall off with increasing particle energy. For medium-weight nuclei and for excitations less than 30 Mev, T is less than 5 Mev.[2]

The discrepancies between experiment and the statistical theory have been summarized in a report on a conference on the statistical model.[5] With higher bombarding energies, a series of experiments indicated that proton reactions prefer to have protons emitted and

neutron reactions result in preferential emission of neutrons.[6-11] This is, of course, in direct contradiction with the theory of separation of formation and decay processes of the compound model. Furthermore, the energy distribution of emitted particles indicated high-energy emission greater than that predicted from a Maxwellian tail.[12,13] Finally, the angular distributions of the high-energy particles were not symmetrical about 90° but were strongly peaked forward.[12,14,15] Thus it was apparent that the compound model was not the complete picture of the nuclear reaction mechanism at the higher energies.

In 1953, Austern, Butler and McManus[16] extended the deuteron stripping theory of Butler[17] to the (n, p) interaction, or by detail balancing to the inverse (p, n) reaction. This theory involves a direct nucleon-nucleon interaction at the surface of the nucleus with the capture of the incoming projectile and the escape of the struck nucleon. This theory was expected to apply in the 10-to 30-Mev range.[16] The theory predicts an angular distribution with sharp maxima near the forward direction. For a reaction of the (p, n) type, the differential cross section is given as

$$\frac{d\sigma}{d\Omega} \sim \sum_{\ell}' A_{\ell}\, j_{\ell}^{2}(qr), \tag{2}$$

where j_{ℓ} is the spherical Bessel function of order ℓ, q is the change in wave number between the incoming proton and emitted neutron, r is the radius of interaction and ℓ, representing the change in orbital angular momentum between the incoming and outgoing particles, is given from conservation of total angular momentum as

$$J_a + J_b + 1 \geqslant \ell \geqslant \left| \vec{J}_a + \vec{J}_b + \vec{1} \right|_{\min.} \tag{3}$$

J_a and J_b are the angular momenta of the initial and final nuclear states. Furthermore, ℓ must be an even or odd integer, depending on whether there was or was not a change in parity between these states.

Although it is difficult to predict cross sections with this model--since it would be necessary to know the amount of overlap of the wave

functions of the initial and final states--this theory does predict that since the core of the nucleus is undisturbed, the reaction will proceed preferentially to the lower excited states of the residual nucleus. This would mean a large yield of high-energy particles.

The original scope of this experiment was an investigation of the energy spectra and angular distributions of neutrons emitted from the 31.5-Mev proton bombardment of several light, medium, and heavy nuclei, as measured by the 4-inch hydrogen bubble chamber. Subsequent experimentation revealed the inadequacy of the bubble chamber for measurements of neutron energies below 5 Mev and hence the impossibility of seeing a peak in the compound-model spectra. Furthermore, the length of time for experimentation and subsequent data analysis made it necessary to decrease the size of the experiment to three targets at three angles. The targets were selected because they yielded a relatively high proportion of high-energy neutrons. The angles selected were 90° and a pair of angles symmetrical about 90° (53° and 127°), and were chosen in order to determine whether the reaction products were produced symmetrically about 90°. Two of the targets, Be^{9} and N^{14}, were light enough to give hope of resolving levels of the residual nuclei B^{9} and O^{14}. Since the (p,n) reaction on a stable target nucleus always has a negative Q value, it is possible, by analysis of the emitted neutrons, to investigate the low-lying levels of the residual nucleus. This residual nucleus is the "mirror" of the target nucleus since it has the number of neutrons and protons interchanged. The investigation of level structure in mirror nuclei is of interest because it bears directly on the assumption of charge independence of nuclear forces. Only a few levels in B^{9} and O^{14} have been investigated,[18] and therefore the proton bombardment of Be^{9} and N^{14} were of interest in relation to nuclear level structure. The third target, Al^{27}, was heavy enough that there would probably not be resolution of the levels in the residual mirror nucleus, Si^{27}. However, the number of nucleons in aluminum was large enough to justify an attempt to interpret the (p,n) reaction mechanism in terms of a compound model.

An important aspect of this experiment was the use of a hydrogen bubble chamber as a neutron spectrometer. For the purposes of this

experiment, a spectrometer having both good resolution and high efficiency was needed. An electronic instrument would have been preferred because of the short data-analysis time required after the experiment. However, electronic neutron spectrometers of good resolution do not have good detection efficiency. An instrument that has come into wide use is a proton-recoil counter using a thin hydrogenous radiator followed by two proportional counters and a scintillator crystal.[19, 20] This type of instrument has been made with efficiencies up to 10^{-4}.[21] Another type of electronic spectrometer uses a coincidence counting method to select the angle of scattering and a scintillating crystal to measure the recoil proton energy. For resolution of about 10%, the efficiency of this type is also 10^{-4}.[22]

In order to measure our spectra in a reasonable time, an efficiency of 10^{-3} or greater was desired. Such an efficiency is found with the cloud chamber and the photographic emulsion. It is also found in a bubble chamber. Because the liquid hydrogen acts both as a recoil-proton indicator and as the recoil-proton detector, the 4-inch instrument can have an efficiency of 5% for 10-Mev neutrons and a resolution of 10% for 14-Mev neutrons. The increase of density of hydrogen gives the bubble chamber an advantage over the hydrogen cloud chamber and the presence of only protons in the bubble chamber makes the events easier to analyze than recoils in an emulsion. In comparing the efficiency of the 4-inch bubble chamber with an electronic neutron counter, one must consider that the bubble chamber can expand only about once every 5 seconds, which means detection of only 1/75 of the neutrons that can be produced at the Berkeley linear accelerator. An electronic counter does not have this duty-cycle factor, so that the ratio of "effective" efficiencies of bubble chamber to electronic counter is really a factor of 10. A factor of 10 in accelerator time was a large enough consideration to make the use of the bubble chamber mandatory despite the great amount of time (8 months) needed to read and analyze the photographs from the experiment.

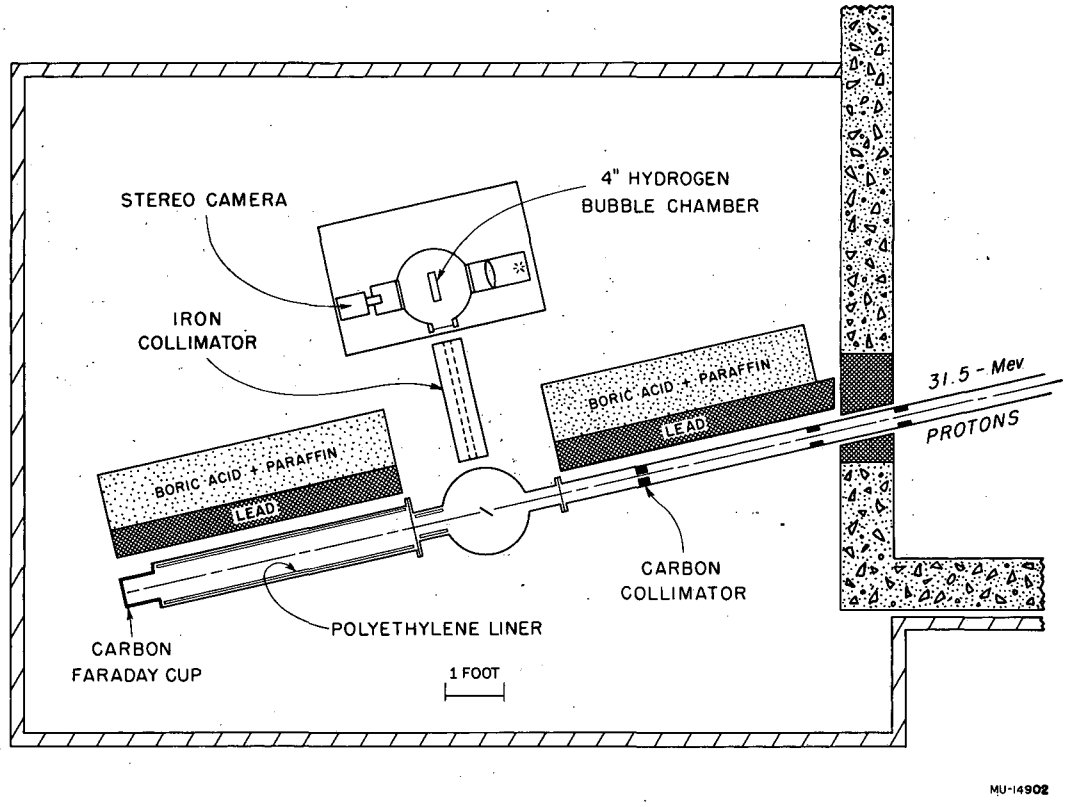

Fig. 2. Schematic diagram of outer bombardment area of Berkeley linear accelerator, showing in detail the beam collimators, target chamber, Faraday cup, iron neutron collimator, and 4-inch hydrogen bubble chamber.

negative-feedback electrometer and was displayed on a Leeds and Northrup Speedomax recorder. Since we used only one beam pulse of 500 microseconds' duration every 5 seconds, the ink recording of the accumulated charge appeared as a step function whose total height (voltage) was proportional to the number of protons incident on the Faraday cup. Knowledge of the capacitance allowed an absolute determination of the proton flux. This number was not necessarily the number of protons incident on the target, since the target would Coulomb-scatter part of the beam into the beam pipe between the target and the Faraday cup. This effect was expected to be small since the targets were relatively thin (less than 1 Mev thick at 32 Mev) and were of low atomic charge ($_{13}Al^{27}$ was the highest). The effect was measured through provision of another beam monitor by placing a 2-mil tantalum wire on a remotely operated flip-up mechanism in the beam pipe upstream from the target. A thin aluminum window was made in the beam pipe so that a small NaI crystal and photomultiplier counter could view the 32-Mev protons elastically scattered from the wire. A 10-channel pulse-height analyzer was used to find the elastic peak. Measurements showed that the number of protons counted in the elastic peak correlated to the beam current as measured on the Faraday cup. Thus the beam-scattering wire setup was a relative monitor of the beam current incident upon the target. Runs were made with the targets in the beam and, alternately, with no target. From the information from the two beam monitors, the transmission coefficients or target-in/target-out ratios (k) were determined. They are listed in Table I. This ratio was between 95% and 100% for all the targets, i.e., less than 5% of the beam was scattered by the target into the beam pipe and hence was not collected on the Faraday cup. In determination of the absolute differential cross sections, corrections were made for the beam transmissivity of each target.

Table I

Specifications of targets

Target	Thickness (mg/cm^2)	Energy thickness for 31.5-Mev proton beam at 30° position (Mev)	Transmission coefficient, k	Isotopic content
$_4Be^9$	23.82	0.42	1.00 ± .02	Monoisotopic
$_{13}Al^{27}$	38.98	0.62	0.97 ± .03	Monoisotopic
Melamine ($C_3N_6H_6$)	39.3	0.82	0.97 ± .03	$\frac{N^{14}}{N^{14}+N^{15}}$ = 99.6%
CH	25.90	0.54	0.95 ± .06	$\frac{C^{12}}{C^{12}+C^{13}}$ = 98.9%

3. Targets and Target Holder

Four targets were bombarded. They were beryllium, aluminum, melamine, and polyethylene. Melamine is a compound of carbon, hydrogen, and nitrogen ($C_3N_6H_6$), and was used, in effect, as a source of solid nitrogen since carbon has a low neutron-production cross section and, of course, no neutrons are produced by the hydrogen. The polyethylene (CH) was used as a carbon target for subtraction from the melamine data in order to get the nitrogen contribution. All the targets except melamine were obtainable as foils of the desired thicknesses. The melamine, a powder, was made into thin targets by evaporating it on a thin foil backing which was later stripped off.[24, 25]

The targets were mounted on a thin brass rectangular frame whose inner dimensions were 1×2-1/2 inches. The target holder was an aluminum ladder which held nine such target mountings. This target holder was mounted vertically in the cylindrical aluminum target chamber, as shown in Fig. 3. The diameter of the chamber was 9.5 inches. The top and bottom of the chamber were lucite discs. Wilson seals were mounted through the lucite and permitted manual changing from outside the vacuum system of the target position as well as the angle of the target to the beam. The targets could be viewed through the lucite at the top and bottom of the chamber or through small lucite windows (not shown in Fig. 3) on the sides of the chamber at beam height.

In the usual running conditions, one of the target positions was mounted with a brass frame without a target ("dummy" target). Another position had an 1/8-inch-thick piece of glass so that a "photograph" of the beam spot could be taken in order to check the size and alignment of the beam. All targets were run at 30° to the beam, since this angle permitted both the proton beam to pass through the target and the resultant neutrons to go toward the bubble chamber without striking the target holder. Table I gives the thickness of each target in milligrams per square centimeter and the energy thickness for a proton beam of 31.5 Mev when the target was placed at 30° to the beam.

4. Shielding

In our first experimental trials we attempted to run without any shielding between the beam pipe and the bubble chamber. However, excessive gamma background, which appeared as electrons in the chamber, necessitated the addition of lead shielding along the beam pipe. Because the lead might act as an elastic scatterer of neutrons from the target into the bubble chamber, we also added, between the lead and the bubble chamber, 16 inches of a paraffin and boric acid mixture sealed in wooden boxes. These boxes had been found particularly useful for neutron degrading and absorption in a previous experiment.[26] With this arrangement (shown in Fig. 2), virtually no neutrons (i.e. $\ll 1\%$ of any target spectrum) entered the bubble chamber when the dummy target was placed in the proton beam.

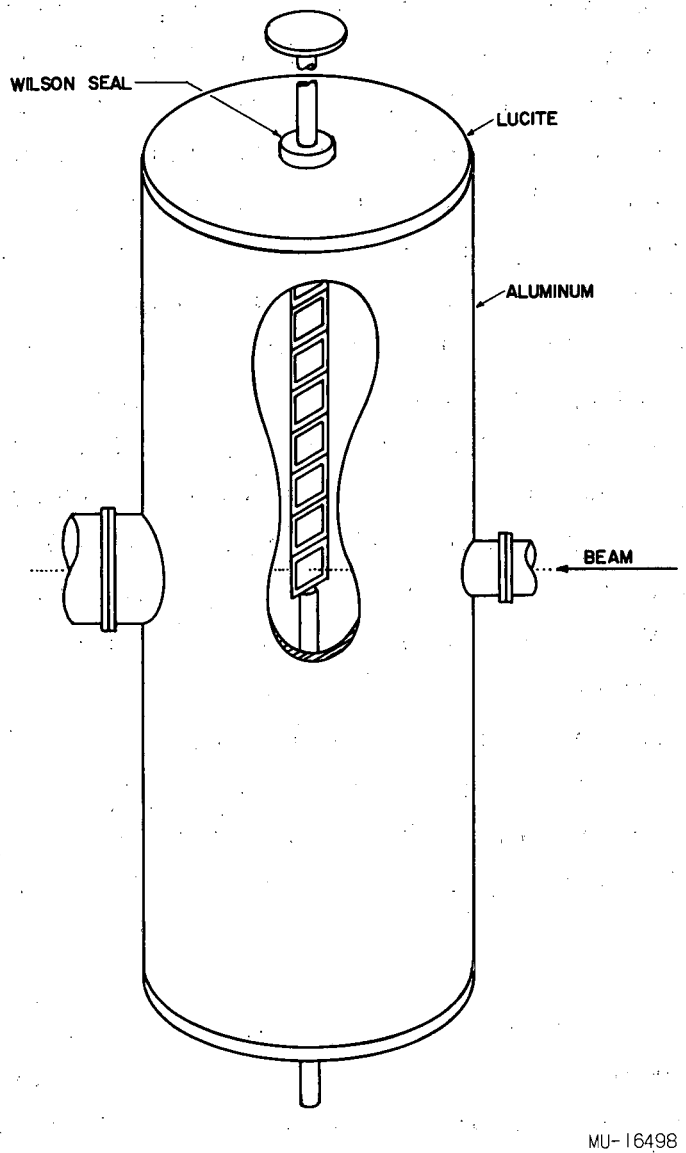

Fig. 3. Sketch of aluminum target chamber showing the nine-position target holder. Not shown in this diagram are the lucite windows cut into the 1/8-in. alumunum walls at beam height. The target position and angle could be controlled manually from outside the vacuum system.

B. Bubble Chamber

1. Description

Figure 4 shows the 4-inch bubble chamber in the actual arrangement at the Linac. (Also shown schematically in Fig. 2.)

The theory and operation of this bubble chamber have been fully described previously.[27] In a bubble chamber, a liquid is maintained in a superheated condition so that an ionizing particle passing through this liquid will, under the proper conditions, form a track composed of bubbles. In the 4-inch hydrogen chamber, this condition of superheat was brought about by quickly dropping the pressure from 5 atmospheres to 1 atmos on liquid hydrogen maintained at a temperature of 26°K. Liquid hydrogen boils at 20°K. The liquid in the chamber boiled spontaneously about 50 milliseconds after the rapid expansion. This allowed ample time for neutrons produced by the 500-μsec proton bombardment of the target to pass through the chamber, producing proton recoils whose bubble tracks grew to a photographable size in about 6 msec.

Figure 5 is a photograph of the cylindrical glass, steel, and copper container for the superheated hydrogen. The inner diameter was 4 inches and the liquid hydrogen filled the 2-inch separation between the glass walls. The steel wall of the container was connected by a copper heat leak to a flask of liquid hydrogen at atmospheric pressure (20°K). The liquid hydrogen flask was surrounded by a liquid nitrogen jacket (77°K) and the whole bubble chamber assembly was placed in a brass cylindrical vacuum jacket. The assembly is shown schematically in Fig. 6. The brass vacuum jacket had a 15-mil stainless steel 4-inch-diameter entrance window, and the sensitive chamber had a window of 7.5-mil mylar 7/8 inch in diameter.

As can be seen in Fig. 4, the entire bubble chamber assembly was mounted on a triangular table whose apex was pivoted on a jack directly under the target. Since there were wheels at the other two corners of the triangle, the 1000 pounds of equipment could be rotated easily around the target without changing the distance between the bubble chamber and the target. In Fig. 4 there can also be seen the beam pipe as it enters the outer bombardment area on the left side of the photograph, the aluminum target chamber in the center, and the after-beam pipe which ended in the

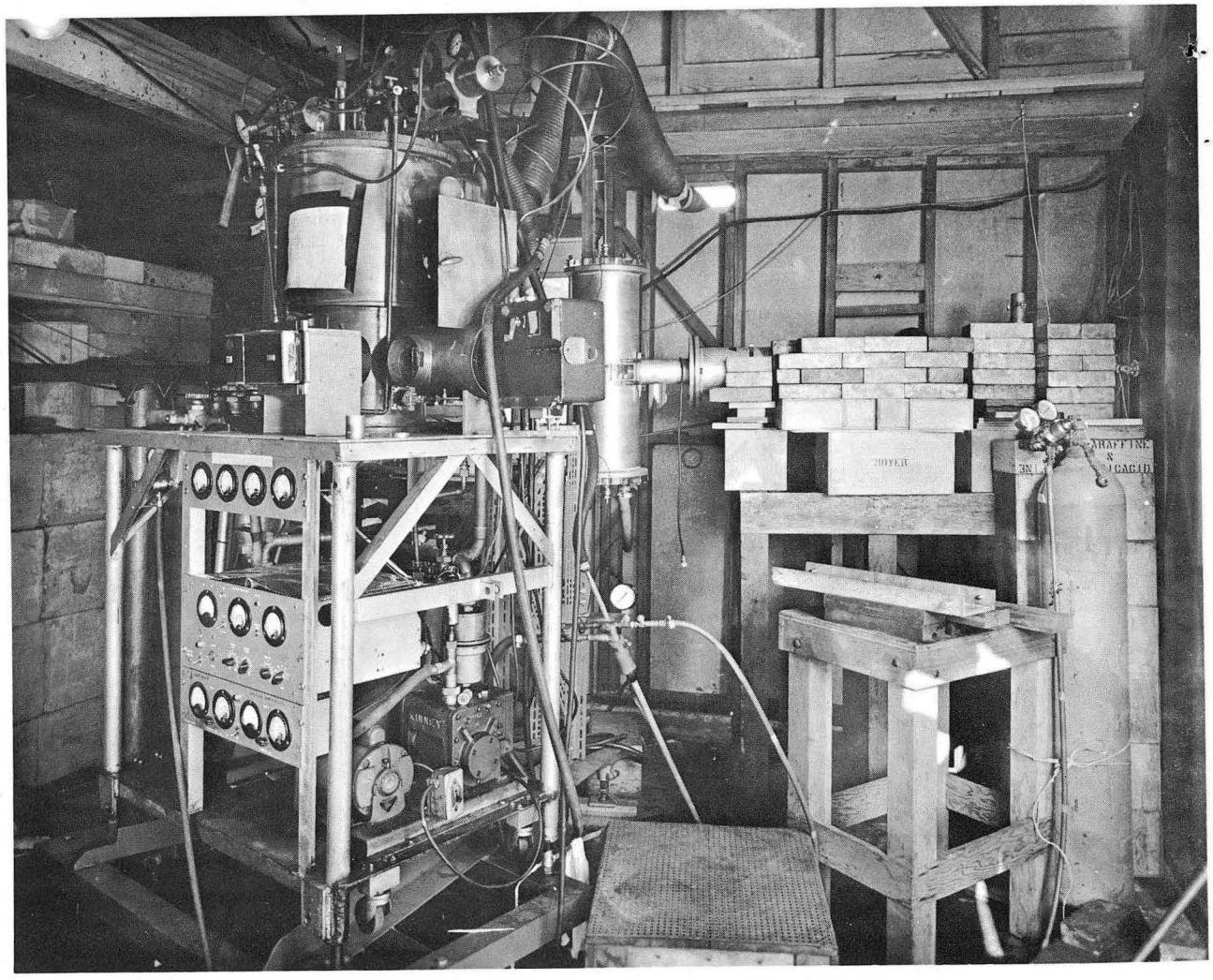

ZN-2101

Fig. 4. **Four-inch liquid hydrogen bubble chamber in the** experimental position in the outer bombardment area. The target-chamber cylinder is connected to the enlarged after-beam pipe, which is hidden behind lead shielding. Most of the paraffin—boric acid blocks have been re**moved.**

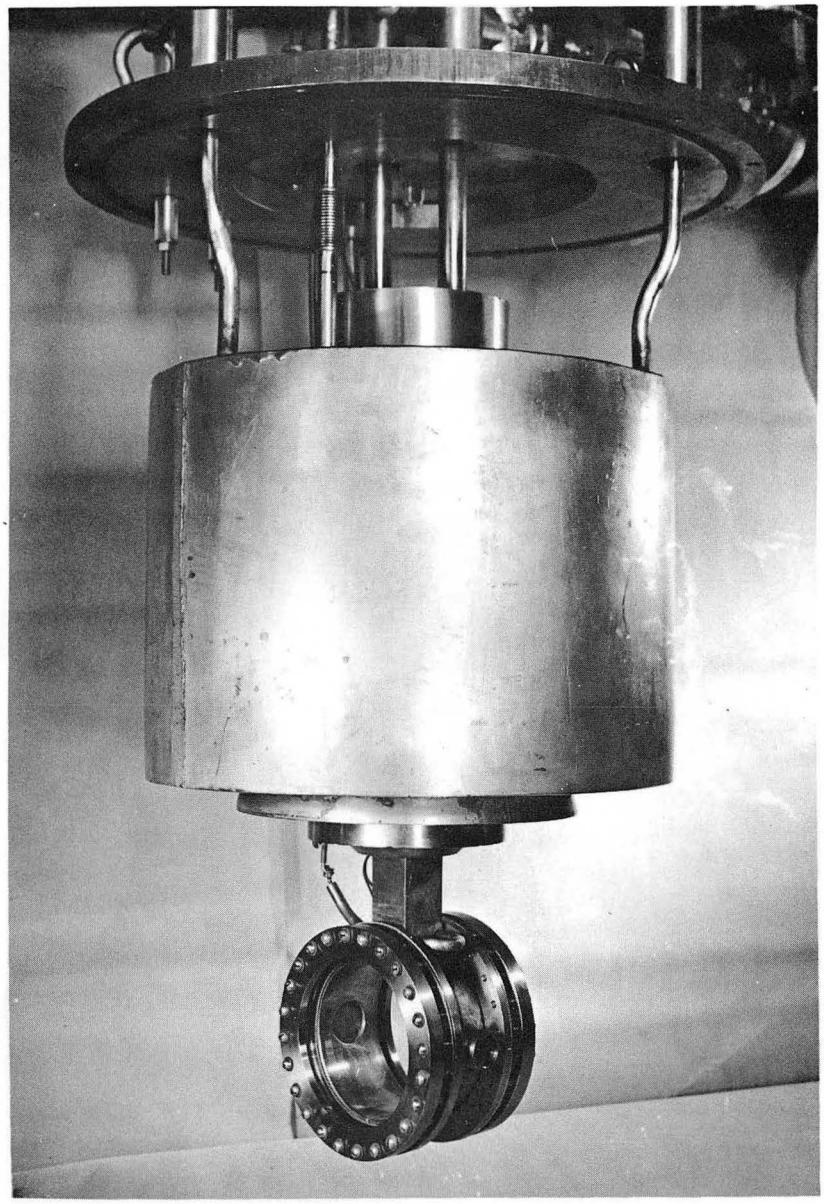

ZN-2100

Fig. 5. Photograph of the 4-inch-diameter hydrogen bubble chamber, showing the glass and copper-steel walls of the 2-inch-wide chamber. The chamber is connected by a copper heat leak to a flask of boiling liquid hydrogen which is surrounded by a large cylindrical jacket of liquid nitrogen. The 7/8-inch-diameter Mylar entrance window can be seen on the chamber. The entire assembly is suspended in a vacuum chamber during operation.

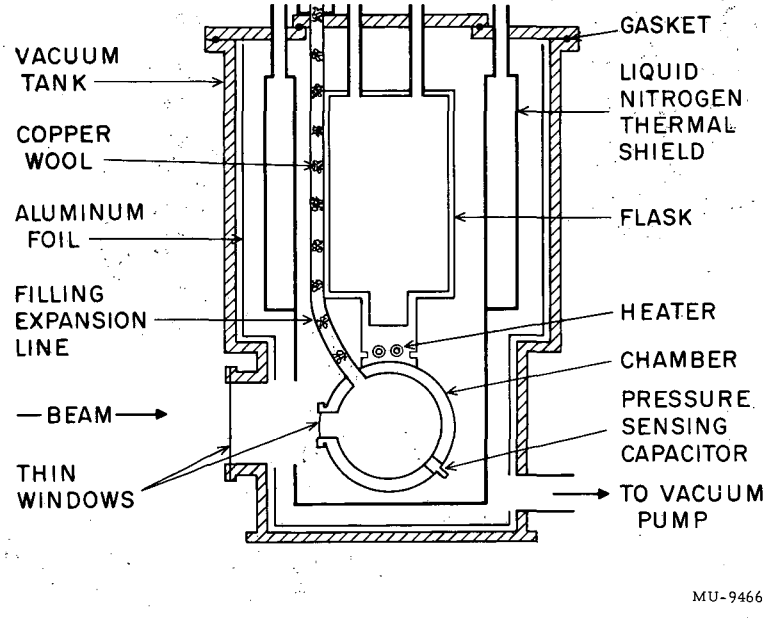

Fig. 6. Schematic drawing of 4-inch hydrogen bubble chamber.

Faraday cup hidden behind the lead shielding. Much of the shielding used in the experiment is not shown in this picture.

2. Thermal Controls

The hydrogen in the senstive disc was maintained at 6°K above the temperature of the boiling hydrogen in the flask by use of electrical heaters inserted in the thermal heat leak. The temperature of the chamber was determined by measuring the vapor pressure of a bulb of hydrogen located in the chamber. At normal operating conditions this vapor pressure, as read on a pressure gauge on the control rack, was about 58 psi. A variation of 1 psi corresponded to a change of 1/10° in temperature.[28]

Stability of temperature was a necessity in this experiment. It was possible to use the temperature of the chamber to regulate its sensitivity to minimum-ionizing bubble tracks. Proton bombardment of the targets produced gamma rays as well as neutrons, and these gammas produced electrons in the chamber or chamber walls. Since no magnet was used in our work because its heating effect would increase the cycling time of the chamber and also because it would have introduced a large neutron-scattering mass near the chamber, it was necessary to use other means to distinguish between recoil protons and electrons. By operating the chamber at a lower temperature than was normal, it was possible to bias out the minimum-ionizing electrons. However, the chamber could not be allowed to become too cool or the recoil-proton tracks would also begin to disappear. We found that a variation in the vapor pressure of only 2 psi could take the chamber from an extremely electron-sensitive condition to a condition of almost complete insensitivity to protons. Eventually we were able to regulate the temperature within 1 psi (or therefore about 1/10°K), which was barely satisfactory. Even with this control, a scanning of a roll of 400 pictures would reveal a gentle cycling of the sensitivity from slightly electron-sensitive to a cool point at which there might be small gaps in proton tracks. Figure 7 is a photograph of the chamber in a fairly electron-sensitive condition, containing several long tracks in the 20- to 25-Mev region.

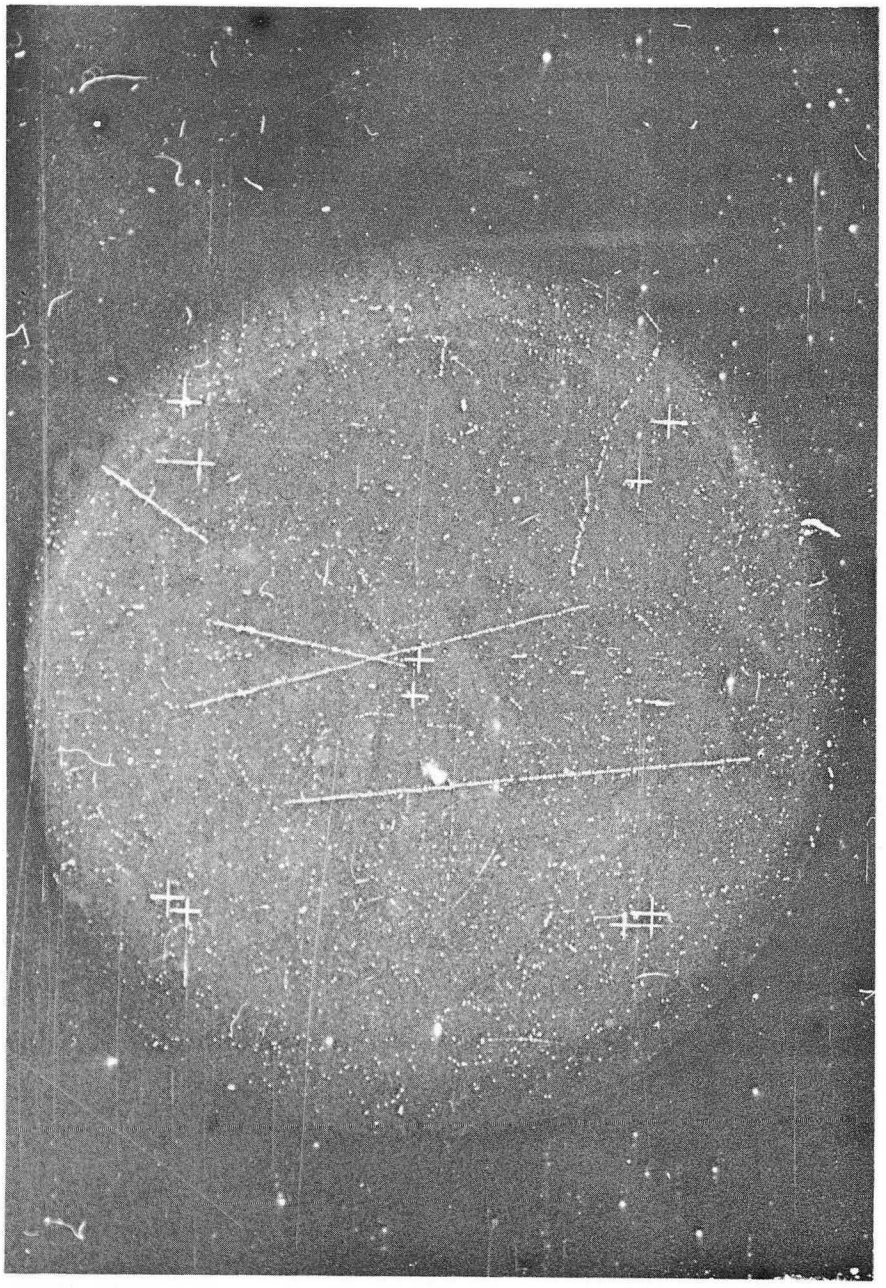

ZN-2102

Fig. 7. Photograph of recoil-proton tracks in the 4-inch hydrogen bubble chamber from neutrons incident from the right. The chamber is in a fairly electron-sensitive condition. The 10 crosses are fiducial marks etched onto the front and back windows of the bubble chamber. Dark-field photography was used.

3. Photography

A parallel-lens "Recordak" stereo movie camera was used to take the stereo pictures of events in the chamber. The camera was run with an open shutter. A dark-field illumination method was used and is illustrated in Fig. 8. The light source was a xenon flash tube. The light was focused by a condenser lens between the two lenses of the camera. Thus no light reached the camera unless a scattering center such as a bubble existed in the chamber. Since this method of illumination yielded good contrast, it was possible to set the lens diaphragms at f/22 and hence have the depth of field large enough to have in focus all tracks throughout the 2 inches of liquid hydrogen. One-hundred-foot rolls of 35 mm panatomic-X film were used, and 400 stereo pairs were taken on each roll. Also photographed on the film was a counter for numbering the photographs and a meter which was used as a beam monitor. Duplicates of this counter and meter appeared on the bubble chamber control rack. This identification information appeared on the film between the stereo pairs.

It was possible to quickly determine the sensitivity of the chamber with the aid of a Land Polaroid camera. The Land camera could photograph the chamber when a remotely controlled mirror was inserted between the bubble chamber and the stereo camera. The chamber sensitivity was checked in this manner every hour.

4. Sequence of Operation

The usual repetition rate of the linear accelerator is 15 beam pulses per second, each of about 500 microseconds' duration. Since the cycling time of the bubble chamber was about 5 seconds, it was necessary to synchronize the expansion of the chamber with one pulse out of about 75. It was also desirable from considerations of background, target heating, and beam measurements to allow only this one beam pulse to enter the bombardment area. This selection of a beam pulse, and synchronization with it, was accomplished with equipment previously used for cloud chamber experiments at the Linac.[29]

During the 5 seconds of "insensitive" time between expansions, the ion-source pulse for the Van de Graaff was generated out of phase with the

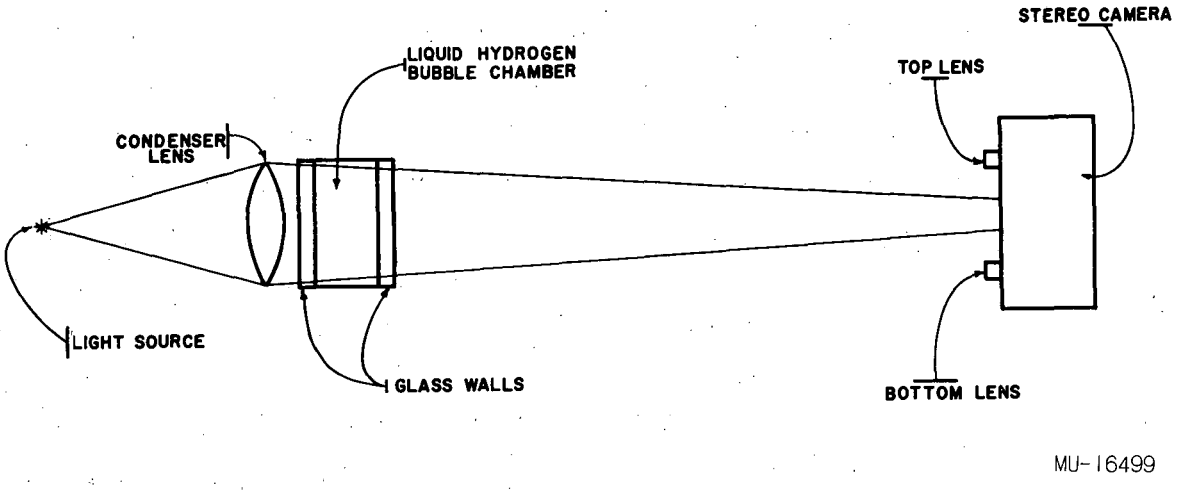

Fig. 8. Sketch of the dark-field photographic method used on the hydrogen bubble chamber. Light reaches the camera lenses only if a bubble is present in the chamber to scatter the light.

rf acceleration of the Linac. No beam pulse could be accelerated through the Linac tank unless a signal was sent, from the timing system of the bubble chamber, that would place the Van de Graaff in phase with the Linac for one pulse. Such an "inphase" signal was developed in the following way. A Flexopulse timer on the bubble chamber control rack indicated when 5 seconds had elapsed since the preceding expansion and recompression. This allowed the timing circuit of the bubble chamber to accept the next equipment pulse, which precedes beam pulses by 20 μsec. Since the latter time was too short to effect an expansion of the chamber, delay circuits were set so that the succeeding beam pulse, 67 msec later, would be placed inphase and the chamber would be expanded when this beam pulse arrived.

In order to set the timing delays correctly, an oscilloscope displaying the relative times of the expansion, the beam pulse, and the light flash was used. A sketch of this display is shown in Fig. 9. The expansion time was indicated by the Linlor pressure-sensitive capacitor microphone[30] in the chamber. A crystal-phototube counter placed in the inner bombardment area indicated the passage of a beam pulse.

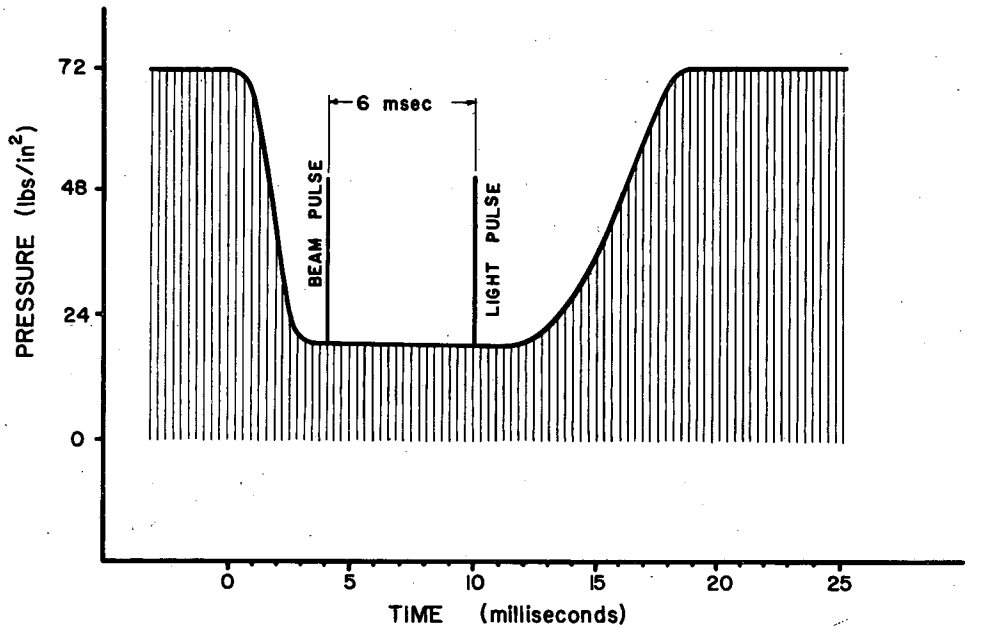

MU-16104

Fig. 9. Sketch of the dual-trace oscilloscope display showing chamber pressure, and the proton beam and photographic light timing pulses during an expansion and recompression cycle of the 4-inch bubble chamber.

C. Neutron Collimation and Resolution

1. Background Measurements

In Fig. 2, the plan view of the outer bombardment area, an iron neutron collimator is indicated between the target and bubble chamber. In our early experimental runs, no collimator was used. An analysis of angular distribution of recoil protons in the chamber indicated a flux of neutrons of about 6 Mev incident upon the chamber from directions other than that of the target.

In order to investigate this background, measurements were taken with the target occluded from the sensitive volume of the chamber by a long cylindrical brass bar. Another type of measurement was made by occluding all regions in the vicinity of the bubble chamber from the target with a large mass of iron. This latter procedure revealed the so-called "room background", i.e., the background resulting from neutrons from the target that recoil from the walls and floor and shielding into the chamber. This was found to be about 5% of the total spectrum. The difference between the first measurement with the long cylindrical rod and the room background was attributed to neutrons that recoiled from the thick glass and steel walls of the chamber itself into the sensitive volume of the chamber. This effect was perhaps two or three times as large as the room background because of the large solid angle subtended by the chamber walls to the sensitive volume of liquid hydrogen.

The obvious way to remove this background was to collimate the neutrons from the target. An iron collimator was designed so that neutrons proceeding toward the center of the sensitive volume would be unhindered while neutrons going toward the walls of the chamber would have to pass through at least 5 inches of iron and perhaps as much as 25 inches. The collimator, partly disassembled, is shown in Fig. 10. It is shown mounted in the running position in Fig. 11. The collimator was mounted on a U beam supported by three jacks so that its height might be adjusted. Two pairs of horizontal screws mounted in opposition afforded lateral positioning. This complete collimator setup sat on a structure which moved with the bubble chamber when the laboratory-system viewing angle was changed.

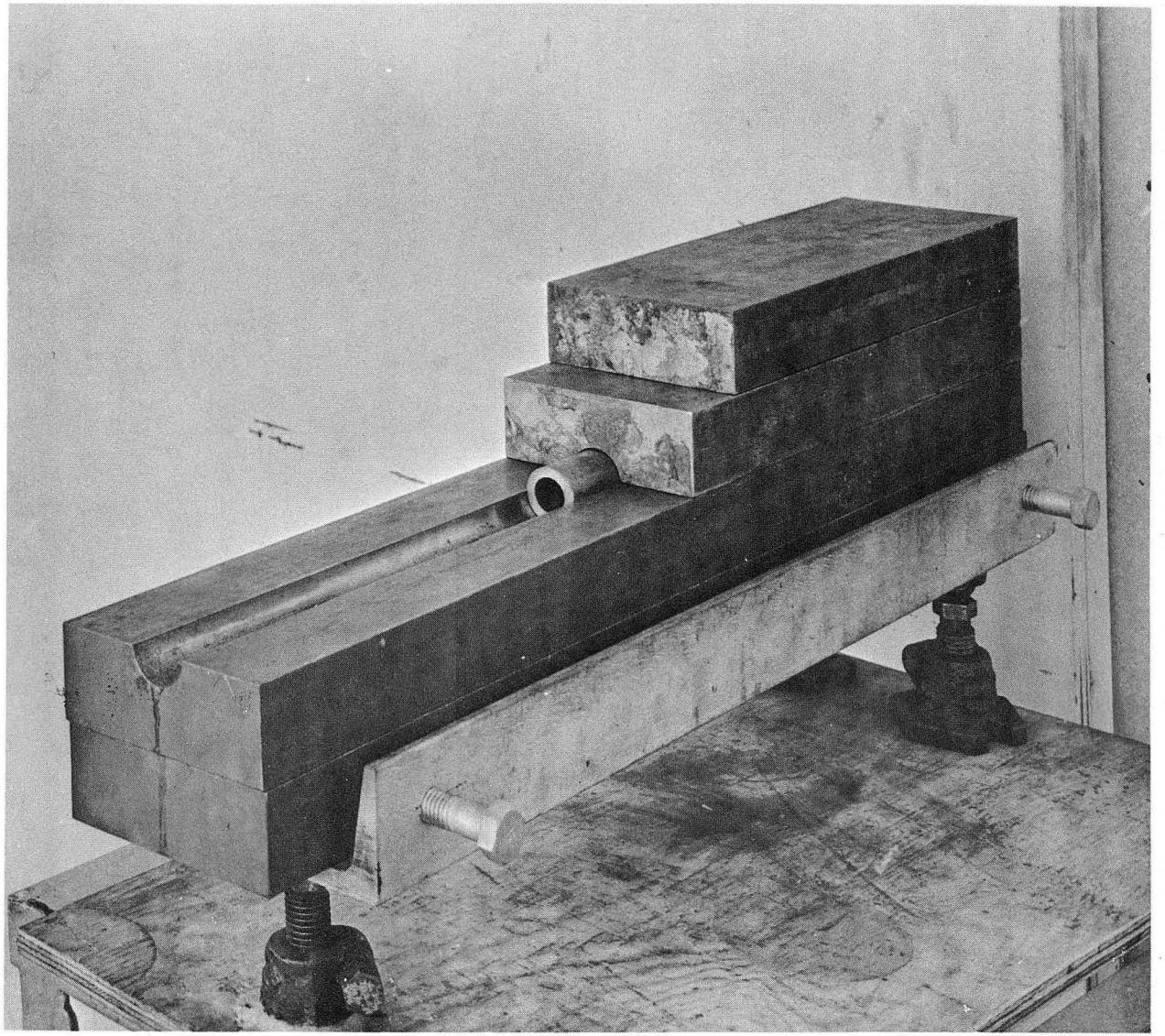

ZN-2050

Fig. 10. The iron neutron collimator shown partially disassembled. The central replaceable collimating cylinder and the jacks for horizontal and vertical alignment of the collimator can be seen.

The collimator was 25 inches long and 4 by 6 inches in cross section. It was made of 4 iron slabs; the top two slabs were cut into two parts for ease of handling. A 1-inch-diameter groove was cut through the center of the collimator. Hence the inner diameter of the collimator could be easily changed by placing cylinders of the desired inner size in the groove. This groove could also be filled with a solid bar in order to make room-background measurements.

Two inner collimators were tried. They were each cylindrical holes, one 7/8 inch in diameter, the other 5/8 inch. A third type, featuring a hole tapering from the edges down to a 3/8-inch-diameter in the center, was discarded early in the experiment because of its distortion of spectra.

2. D-T Reaction and Instrument Resolution

In order to test the effect of these collimators upon our spectra, we used the $T(d,n)He^4$ reaction to generate an almost monoergic neutron beam. A tritiated-titanium target, thick enough to stop a 2-Mev deuteron beam, was procured from the Radiation Laboratory at Livermore. The titanium, which was evaporated onto a tungsten disc, had an areal density of 6.9 mg/cm^2. The ratio of tritium atoms to titanium atoms was 0.787.[31]

When the rf power was turned off (and the Linac was hence as a vacuum pipe), 4-Mev deuterons from the Van de Graaff were available in the outer bombardment area. The cross section for the d-t reaction shows a strong peak at 0.1 Mev deuteron energy,[32] and it was therefore desirable to stop the deuteron beam in the target. Because it was not possible for the Berkeley Van de Graaff to deliver a 2-Mev deuteron beam, it was necessary to degrade the deuterons from 4 Mev down to 2.0 with a gold foil of areal density of 36.7 mg/cm^2 so as to insure the stopping of the deuterons in the target. Gold was chosen for the degrading foil because its high Coulomb barrier would minimize neutron-producing interactions. The foil was placed directly in front of the tritiated-titanium target. A dummy target, consisting of a similar gold foil in

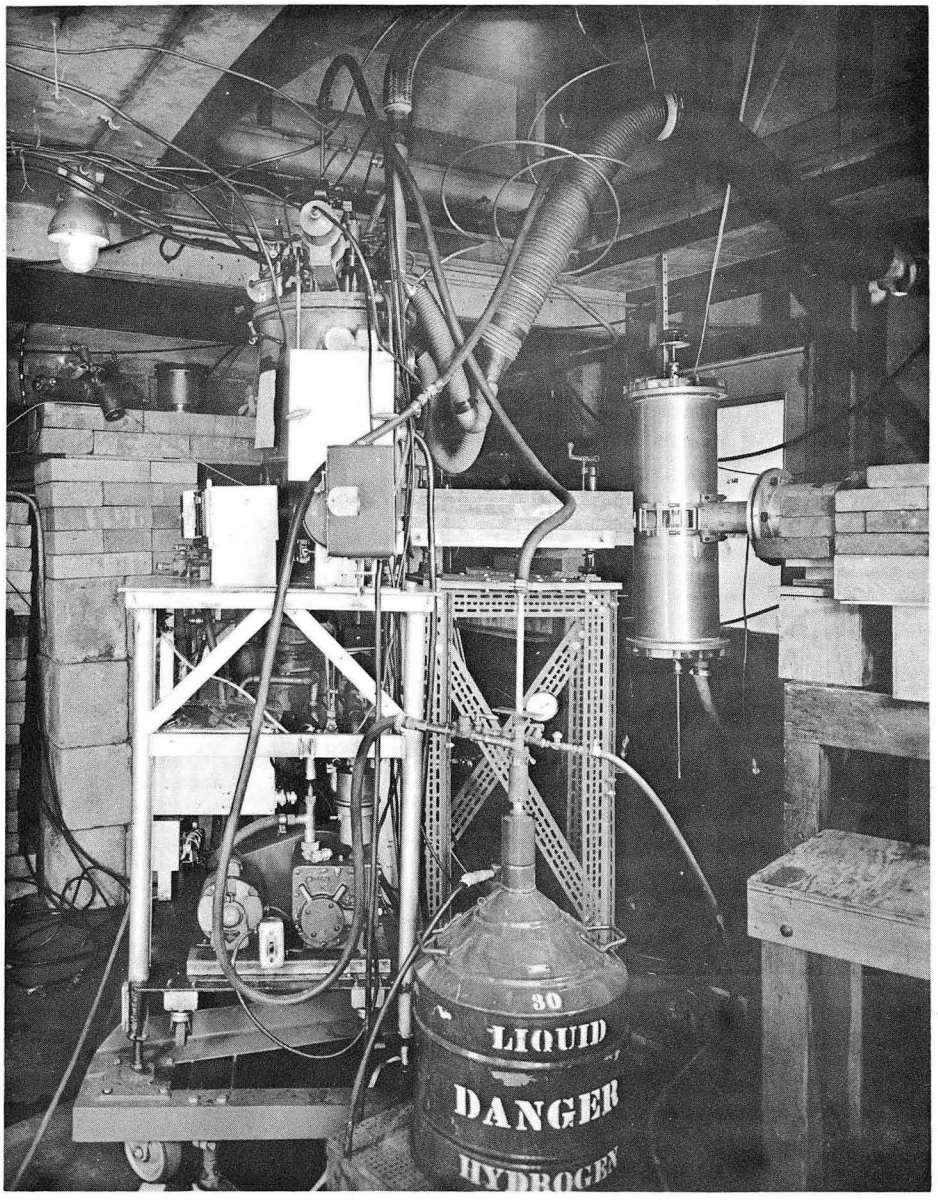

ZN-2049

Fig. 11. Experimental setup in the outer bombardment area showing iron neutron collimator in position between the target chamber and the bubble chamber.

front of titanium that contained no tritium, was also prepared. Deuterons striking this target produced no neutrons and therefore demonstrated that all neutrons observed with the tritium-titanium target were from the d-t reaction.

Accelerating deuterons with the Van de Graaff has always caused a serious safety problem for the accelerator operators because of the copious amount of neutrons produced. Measurements made by the Health Physics Group indicated a neutron background in the control room that was approximately 70 times "tolerance" levels when a 15- pulse-per-second beam was used. Since our operating conditions required only one beam pulse per 5 seconds, our beam-synchronization method was changed so that the Van de Graaff ion source was pulsed directly by the bubble chamber timing equipment and only when the chamber was in an expanded and sensitive condition. But it was still necessary to run steady "deuteron" beams in order to adjust the steering and strong-focusing magnets. Beam line up was effectively accomplished without the severe background, when hydrogen gas was in the ion source, by using the large H_2^+ ion beam that is always produced with the H^+ beam. Since H_2^+ ions have virtually the same e/m ratio as D^+ nuclei, the magnets could be correctly set for deuterons and no steady beams were necessary when deuterium gas was used in the ion source.

Measurements of the d-t neutron spectrum were made with the two collimators with the bubble chamber at 90° to the direction of the incident deuteron beam. At this angle a spectrum consisting of virtually monoergic neutrons of 14.06 Mev is expected. Figures 12, 13, and 14 show the results for the 7/8-inch collimator, 5/8-inch collimator, and no collimator, respectively. Table II summarizes the results for each condition.

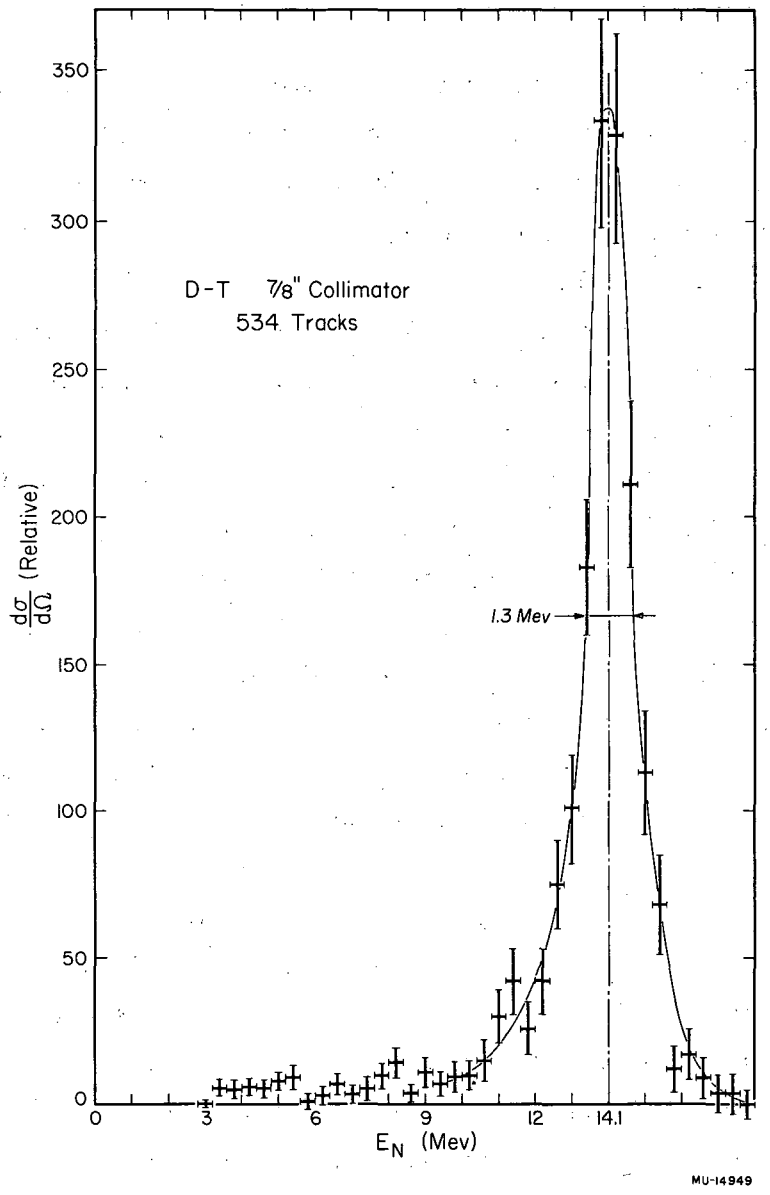

Fig. 12. Measured spectrum of neutrons from the $T(d,n)He^4$ reaction observed at 90^o with the 7/8-inch neutron collimator.

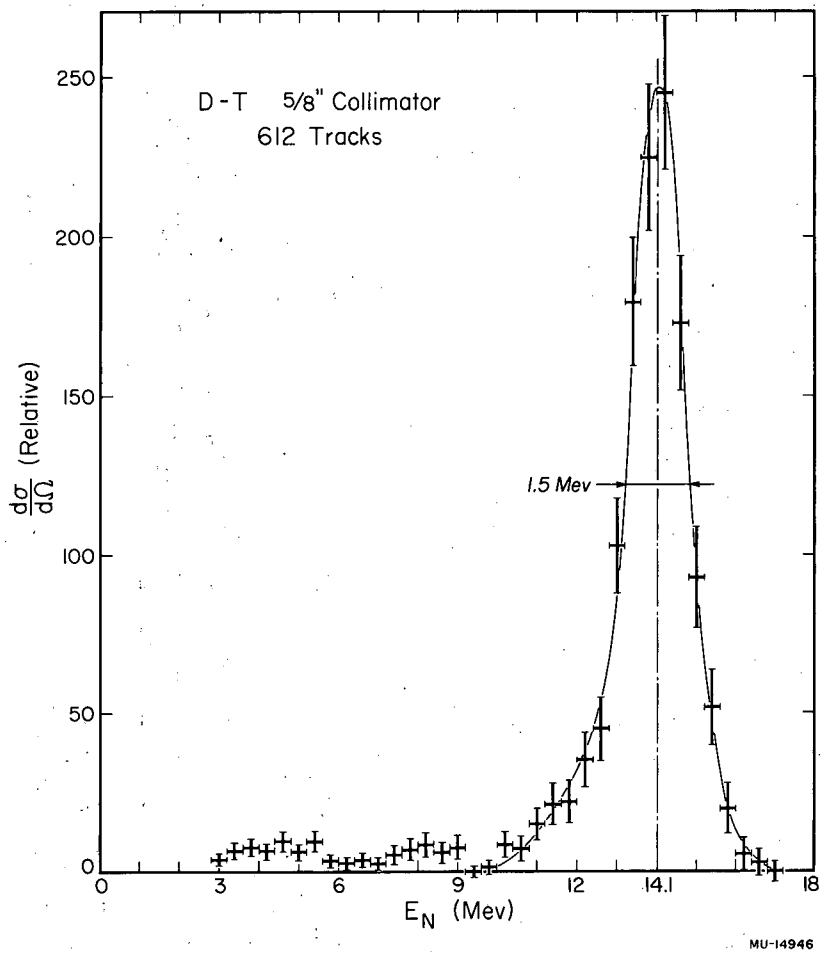

Fig. 13. Measured spectrum of neutrons from the $T(d,n)He^4$ reaction observed at 90^o with the 5/8-inch neutron collimator.

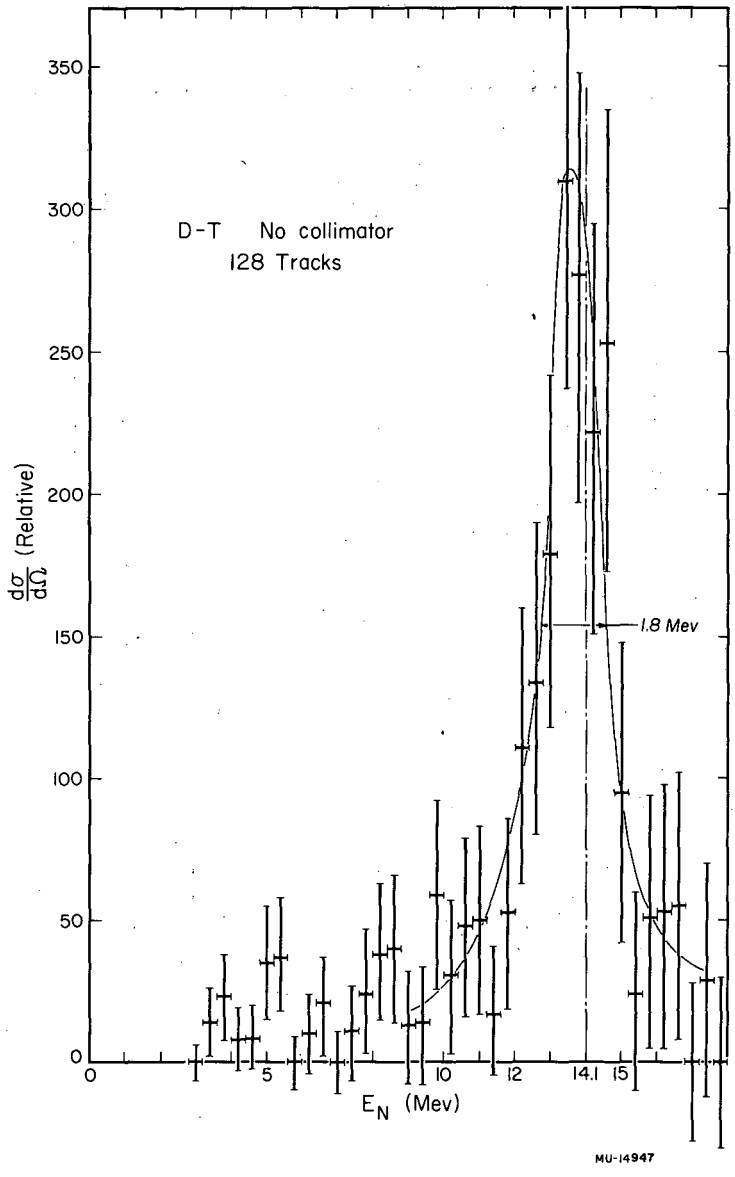

Fig. 14. Measured spectrum of neutrons from the $T(d,n)He^4$ reaction observed at 90^o without the neutron collimator.

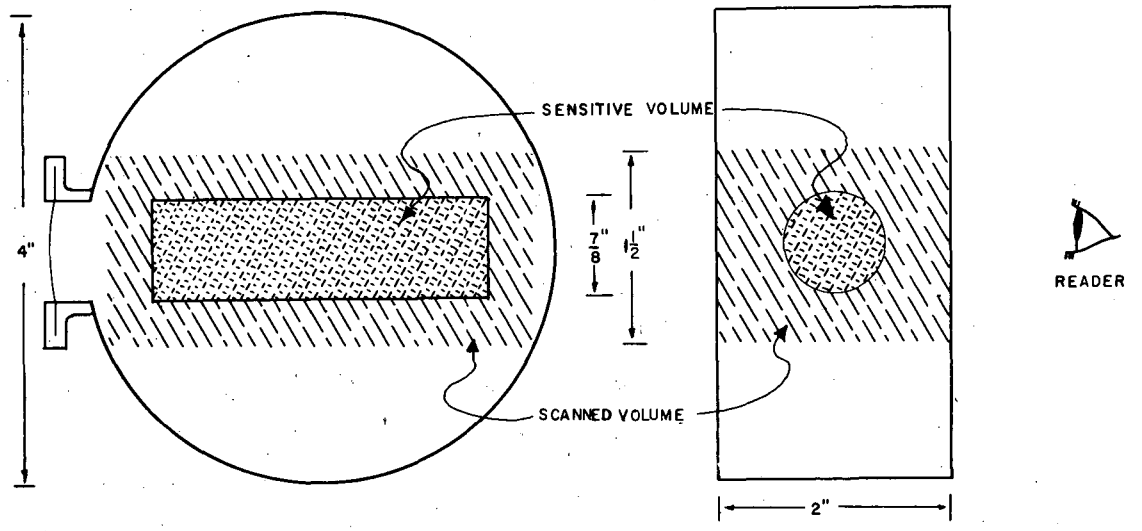

Fig. 15. Sketch of cross section of bubble chamber, illustrating the volume of bubble chamber scanned by the reader and the "sensitive volume" of the chamber in which tracks had to originate in order to be acceptable.

Table II

Results of collimators for d-t spectrum

Collimator	Full width at half maximum (Mev)	% of total spectrum below 12 Mev
7/8-inch	1.3	9
5/8-inch	1.5	13
None	1.8	24

Although the width of the peak for no collimator was not much worse than with collimation, the low-energy tail was substantially increased. The 5/8-inch collimator with its 1.5-Mev full width at half maximum was chosen to be used for data-taking with the proton bombardment of the targets. The reason is illustrated in Fig. 15. Because of the large amount of iron surrounding the 7/8-inch mylar window on the chamber, it was decided to accept recoils that occurred from neutrons entering the chamber through this window only, i.e., recoils beginning in a central cylinder 7/8 inch in diameter. The film reader, however, in scanning the film could not visually determine the depth of a recoil track and recorded all tracks in a region with a cross section of 2 by 1.5 inches. The 5/8-inch collimator allowed fewer neutrons into the unacceptable region than did the 7/8-inch collimator, so that reading time for the same amount of accepted tracks was 1/3 less.

The spectra shown for these collimators were derived from the acceptance of recoils at angles no greater than 30°. The full width at half maximum was larger for acceptance of angles up to 45°. This was because a given error in the determination of the recoil angle caused a larger error in the calculation of the incident-neutron energy for larger recoil angles, as is seen from Eq. (9) (Section III B). Data for the portion

from 30 to 45° in comparison with the 0- to-30° spectrum for the 5/8-inch collimator is shown in Fig. 16. In order to retain good resolution, and also to maximize the ratio of neutrons from the target to background neutrons in the accepted spectrum, it was decided to use recoils from 0° to 30° only in our proton bombardments.

As is shown in Fig. 13, the full width at half maximum for the 5/8-inch collimator was 1.5 Mev. If one calculates the expected spectrum due to 2.0-Mev deuterons stopping in the tritiated-titanium target, the spectrum shown in Fig. 17, Curve A is expected. It would have a full width of less than 0.1 Mev. However, this computation does not include the effects of multiple scattering, either in the target or in the gold foil preceding the target. The energy of the outgoing neutron in the d-t reaction depends upon the angle the neutrons make with respect to the incident-deuteron direction. Multiple scattering of the incident deuterons can drastically change this angle from the assumed 90° and lead to an appreciably wider peak. As indicated in Appendix A, it is the projection of the mean-square scattering angle on the plane formed by the beam line and bubble chamber axis that determines the distortion of the neutron spectrum. The root-mean-square projected scattering angle $\sqrt{\overline{\theta^2}_p}$ of the deuterons (after they emerge from the gold foil in which they were degraded in energy from 4 Mev to 2 Mev) was 10°. By the time the deuteron was degraded in the tritium-titanium foil down to 0.1 Mev, at which energy the d-t interaction has its maximum cross section, $\sqrt{\theta^2}_p$ was 17.5°. A computation including multiple-scattering effects yielded the spectrum shown in Fig. 17, Curve B. Here the full width was 0.6 Mev. This computation is outlined in Appendix A.

If one assumed that the source spectrum (0.6 Mev full width), the measured spectrum (1.5 Mev full width), and the resolution function of the complete system (including the reading system) all had Gaussian shapes, then the full width at half maximum of the resolution function would be given by

$$R_{1/2} = \sqrt{(1.5)^2 - (0.6)^2}$$

$$= 1.37 \text{ Mev.}$$

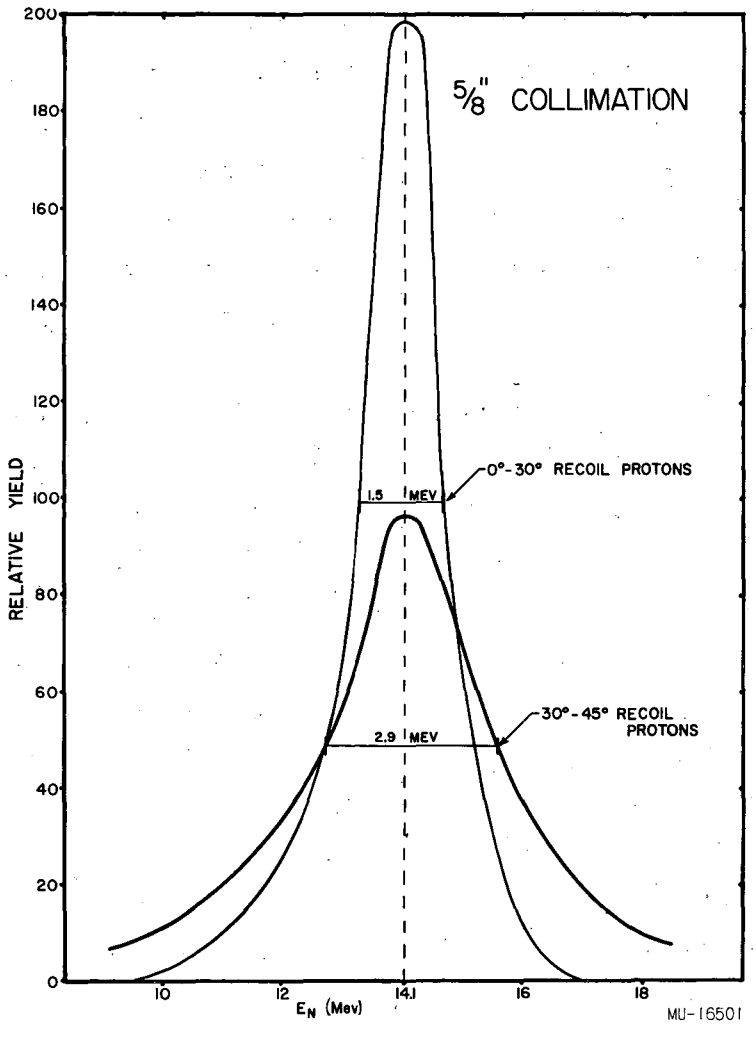

Fig. 16. Comparison of the measured neutron spectrum from the $T(d,n)He^4$ reaction at 90° with the 5/8-inch collimator as obtained by accepting 0°-30° recoil protons with the spectrum for 30°-45° recoil protons.

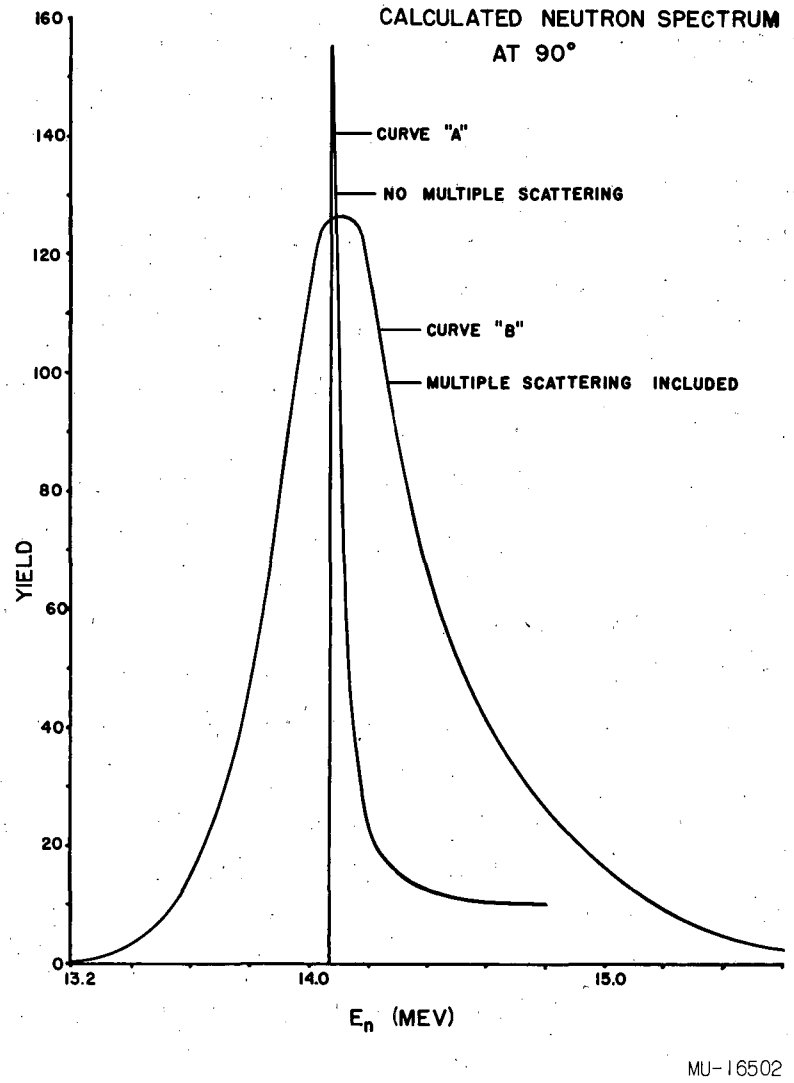

Fig. 17. Curve A is the calculated neutron spectrum at 90° if no multiple scattering of the deuterons occurred. The full width at half maximum is less than 0.1 Mev. Curve B shows the effect of multiple scattering of the deuterons in the gold foil and the tritium-titanium target. The full width at half maximum is 0.6 Mev.

For energies less than 10 Mev, the differential n-p scattering in the center-of-mass system is isotropic:

$$\frac{d\sigma}{d\Omega_{cm}} = \frac{\sigma_T(E_n)}{4\pi} , \qquad (5)$$

where $\sigma_t(E_n)$ is the total n-p scattering cross section. It then follows that the differential scattering per unit angle in the laboratory system is

$$\frac{d\sigma}{d\theta} = \sigma_t(E_n) \sin 2\theta . \qquad (6)$$

Thus the distribution of the proton recoils is symmetric about 45° in the laboratory system.

Above 10 Mev, these relationships are still certainly good approximations, but interference between S and D waves leads to a nonisotropic distribution that is still symmetric around 90° in the center-of-mass system. In our analysis, a semiempirical formulation by Gammel[21] was used above 10 Mev:

$$\frac{d\sigma}{d\theta}(\theta, E_n) = \sigma_t(E_n) \sin 2\theta \left\{ \frac{1 + 2\left(\frac{E_n}{90}\right)^2 \cos^2 2\theta}{1 + 2/3\left(\frac{E_n}{90}\right)^2} \right\} . \qquad (7)$$

For the angular range between 0° and 30°, the correction to the sin 2θ distribution by the terms in the parenthesis was less than 5% at energies less than 30 Mev.

From the assumption of isotropy in the center-of-mass system, it can be shown that for a given neutron energy E_n, the number of recoils N_p per unit proton energy is constant up to the maximum proton energy ($E_p = E_n$):

$$\frac{dN_p}{dE_p} = \frac{N_0}{E_n} , \qquad (8)$$

where N_0 is the number of incident neutrons of energy E_n. With the aid of this formula, much information about reader detection efficiency can be obtained from a study of the recoil proton energy spectra.

In determining sources of errors in the calculated neutron energy, the calculated neutron energy, the effect of an error $\Delta\theta$ in the angle θ is given by

$$\frac{\Delta E_n}{E_n} = -2 \tan \theta \, \Delta \theta \, . \qquad (9)$$

Thus the same absolute angular error occurring for larger recoil angles resulted in a larger proportional error in the neutron energy.

C. Analysis of the Photographs

In the bubble chamber, a neutron which was assumed to have come from the target collided with a proton, causing a straight recoil bubble track. The length of the track determined the energy of the proton. A range-energy relationship for protons in liquid hydrogen was developed from the data of Aron et al.[33] by use of the value of 0.059 g/cm^3 for the density of liquid hydrogen at 26°K.[34] This relationship can be expressed as

$$R_p = a E_p^x \, , \qquad (10)$$

where

$a = 0.0126$,

$x = 1.84$,

R_p = range of protons (in centimeters),

E_p = energy of proton (in Mev).

In liquid hydrogen, a 10-Mev proton travels approximately 0.9 cm. The angle θ that the track makes with the assumed neutron direction and the energy E_p of the proton are related to the energy of the neutron E_n by Eq. (4). Thus, the minimum information necessary for data analysis was the length and angle of the recoil track. Since stereo pictures were

taken of the chamber, this information could be calculated from the projected X-Y coordinates of the end points of the track in both stereo views.

Further information, is desired however, since the acceptance criteria listed in Section IV A demand a knowledge of the position of the track with respect to the entrance window of the bubble chamber. Thus an absolute coordinate system had to be set up for each picture. This was accomplished by also measuring the coordinates of a fixed point in the chamber, a fiducial mark scratched on the front glass wall of the bubble chamber.

D. Reading Equipment

The Benson-Lehner OSCAR Model N-2 is a general-purpose data-reduction machine for measurement of oscillograph trace and film records. The machine provided direct digital readout of X and Y Cartesian coordinates. The coordinate output had a range from 0000 to 9999, where 1 unit corresponds to approximately .05 millimeter. The output was wired into an IBM 026 readout punch, and the coordinates appeared directly on IBM cards. The OSCAR has a square frosted-glass projection screen 20 inches wide. Across this screen move two transparent lined cursors for the measurement of X and Y positions. The reference cross hairs are placed in position by turning cylindrical controls and a readout is made by pressing a foot switch. The reading equipment is shown in Fig. 18.

For our purposes, the OSCAR had to be adapted to stereo projection. This required removal of the single-lens projector with which the OSCAR was equipped, the addition of a large front surface mirror, and the mounting of a stereo projector. We used a common home stereo projector that was modified so that it could project our nonstandard stereo pairs, which were separated by 3.5 inches on the 35-millimeter film. This projector was further modified by individual solenoid-operated shutters placed in front of each lens and by having the lenses mounted so that they could be moved vertically and horizontally with respect to each other. A remotely controlled film-advance system was also added. All these controls plus a focus control appeared near the reader observing the projection screen. Figure 19 shows the optical modifications.

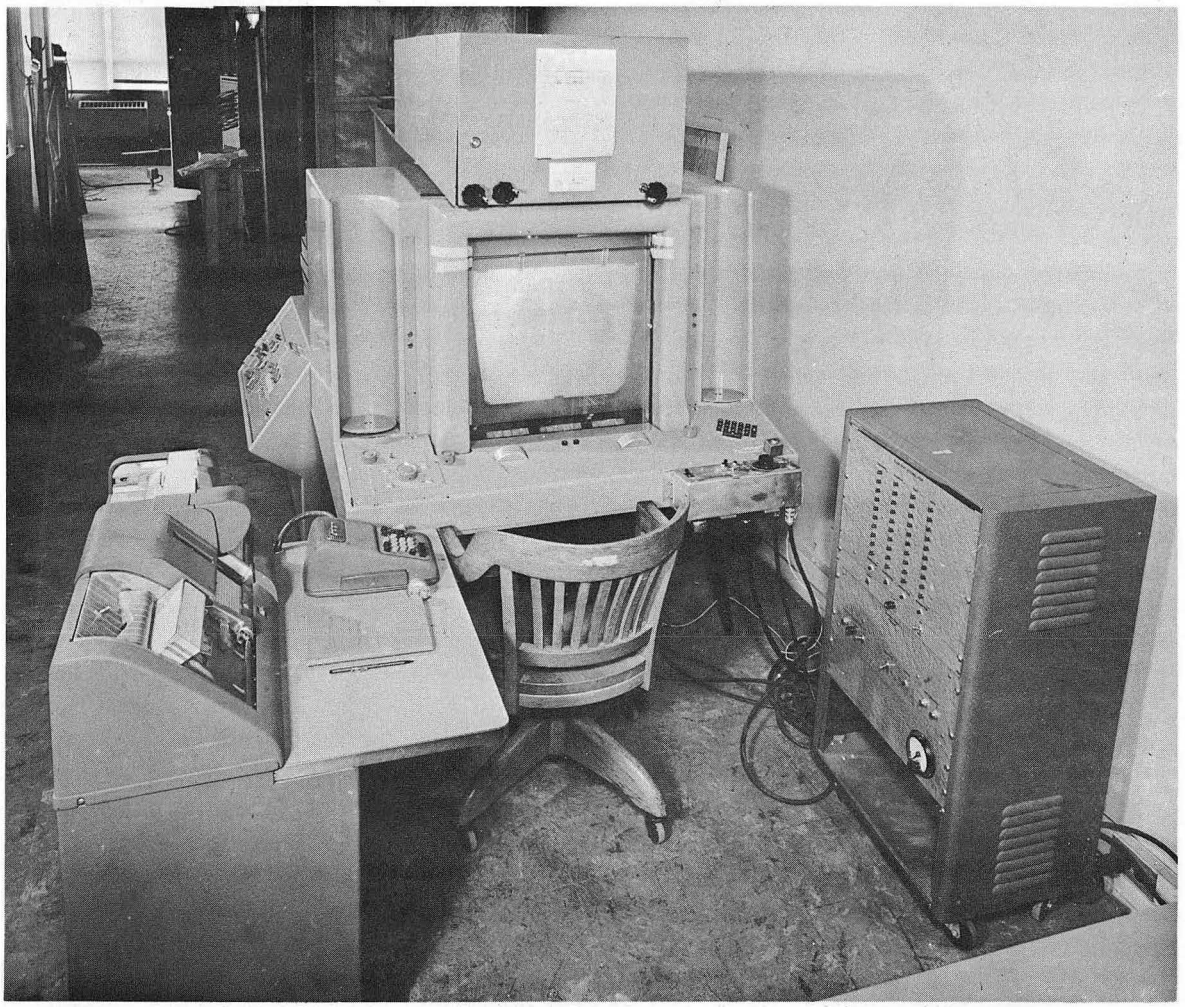

ZN-2052

Fig. 18. Track-measurement equipment; left to right, IBM-026 card punch, Benson-Lehner "OSCAR," and the view-sequencing and track-accumulator chassis.

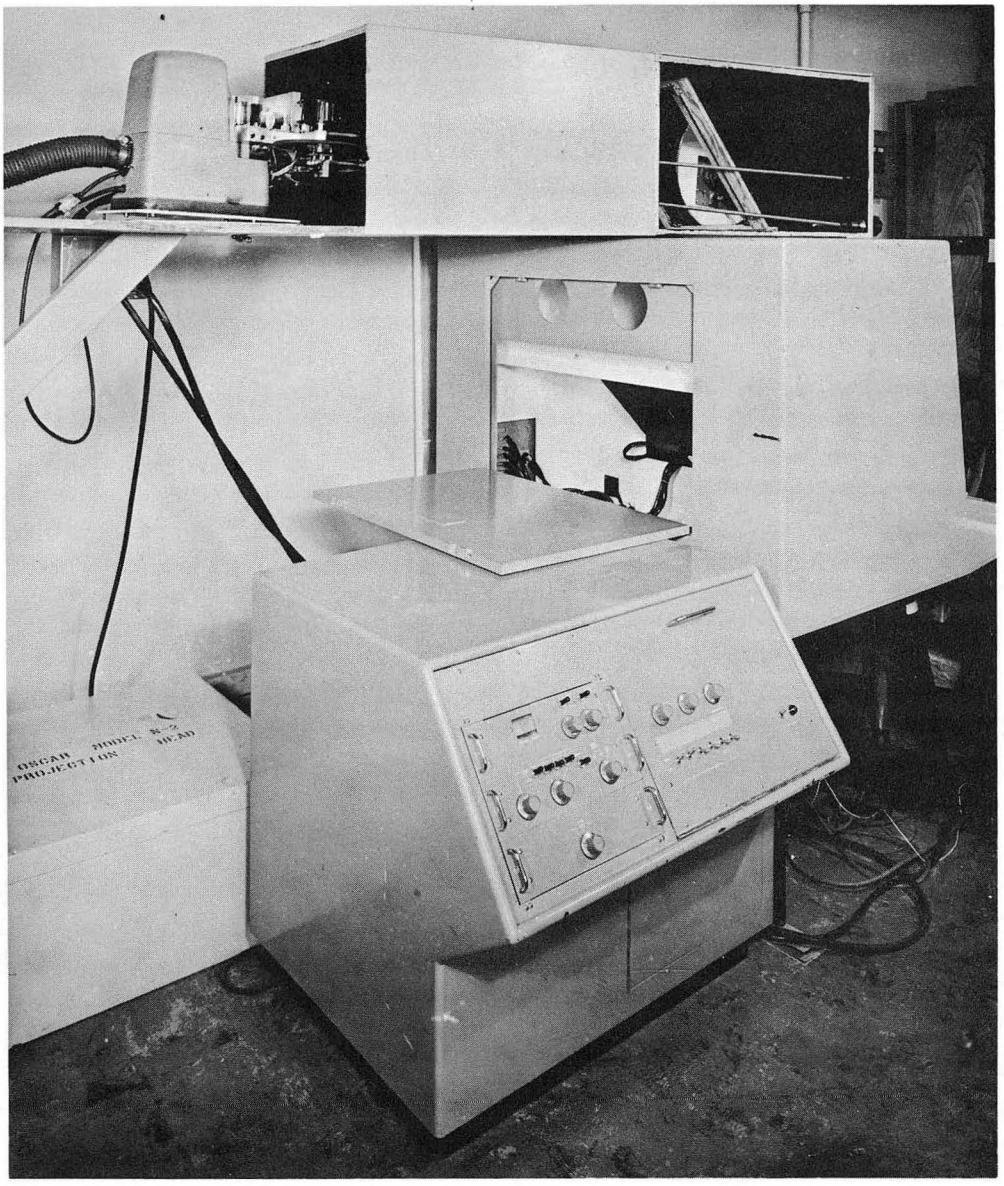

ZN-2053

Fig. 19. Side view of the "OSCAR", showing the optical modification and control mechanisms for stereo projection.

Since the reading procedure was fixed, a shutter-control chassis was built so that the proper view appeared on the screen at all times. This chassis, whose operation is described in detail in the next section, is also seen in Fig. 18 to the right of the OSCAR.

E. Reading Procedure

As previously explained, it was necessary to measure the end points of each track in each view. This meant that every track had four sets of four digit X-Y coordinates describing it. For identification purposes, each track also had an 11-digit identification number which was made up of a 4-digit run number that determined the experimental conditions such as target and angle for this roll of film, a 3-digit picture number that located this particular stereo pair on the roll of film, and a 4-digit track number that indicated how many tracks had already been read in this picture. An IBM card containing this 11-digit identification number with a track number greater than zero and also containing four sets of X-Y coordinates was called a "track card" and completely described one track.

Since it was necessary to establish an absolute coordinate system in the chamber for each picture, another kind of IBM card was also punched. This coordinate system was established by recording the position of a particular fiducial mark as it appeared in both stereo views. This card was called a "master card" and was identified by the fact that the track number of the identification number was 0000. This card had only two sets of X-Y coordinates punched on it. A master card was made for any picture containing tracks and always preceded the track cards for that picture.

The reader used the following procedure in recording the tracks in a picture. After placing View I of a stereo pair on the screen and observing the existence of tracks in this picture he was ready to begin measuring. The first card punched was the master card for this picture. He would first enter the identification number. The run number was stored electronically on the OSCAR memory and was entered on the master card by pressing a particular switch. The picture number was recorded on the

film between the stereo pairs and was entered manually on the card by using the typewriter key of the IBM 026 punch. Immediately following the entering of the picture number, an electronic accumulator chassis entered the track number--which would be 0000, since this was a master card. The reader was now ready to record the fiducial mark in View I (see Fig. 20). After placing the cross hairs on the fiducial mark he entered the coordinates by pressing the foot switch. While the coordinates were being punched, an automatic-sequencing chassis which controlled the shutters on the projector changed the picture to View II of the stereo pair. The reader entered the fiducial mark in that view and the master card was then complete. The viewer automatically reversed to View I so that the reader would be ready to enter tracks in the picture. Also automatically, the master card was released and a new IBM card was identified with a track number of 0001 from the accumulator chassis. The reader located a track, placed the cross hairs on the origin of the track (Point a in Fig. 20), and entered the coordinates of Point a. The view did not change until he had also entered the coordinates of the end of the track, Point b. Then, the view changed automatically to View II and the reader entered the coordinates of c and d in that order. This completed the reading of track No. 1 in this picture. The view changed back to View I and a new IBM card had the identification number with picture number 0002 automatically entered. The reader was now ready to enter the coordinates of track No. 2 in this picture. This procedure continued until the last track in this picture. When the reader entered the last coordinate (Point d) of the last track, he used a different foot switch, which indicated the termination of this picture. The view would then change back to View I but the new IBM card would have no identification number entered. This new card would be the master card for the next picture that contained tracks, and its identification number was entered in the same manner as that for the preceding master card.

Because of differences in running conditions, there may have been from 0 to 20 tracks in a picture. A reader could produce a track card in less than 10 seconds. The reader, after entering the identification number on the master card, had no other duty except to place the cross hairs at the proper position for each point. Views were changed automatically at the proper time and identification numbers were entered automatically.

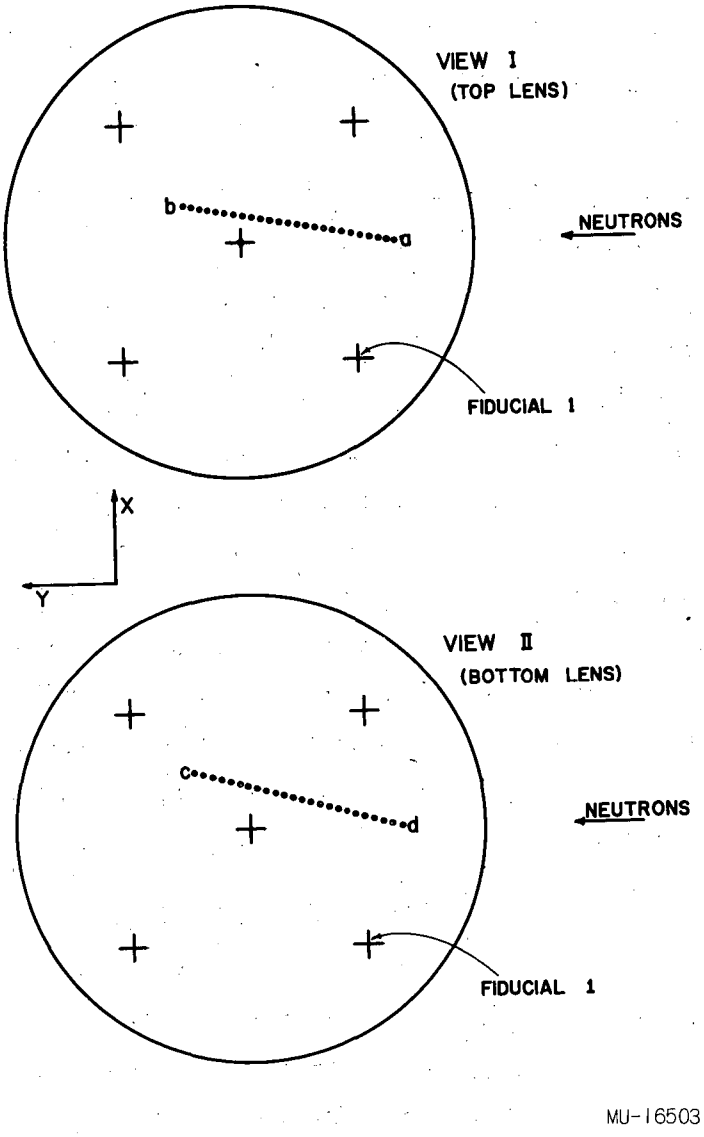

Fig. 20. Sketch of a stereo photograph of the bubble chamber. Reader measured the coordinates of fiducial mark No. 1 in both views in order to set up an absolute coordinate system. The end points of the recoil track were measured in the order a, b, c, d.

F. Computer Calculations

The master cards and track cards formed the data input to the IBM 650 digital computer, which calculated the following quantities for each acceptable track:

l = length of recoil proton track in cm.

E_p = corresponding energy of proton,

θ = polar angle of track with respect to assumed neutron direction,

ϕ = azimuthal angle of track,

E_n = energy of incident neutron,

d = absolute y coordinate of beginning of track.

This calculation, which by hand would have taken several hours, was accomplished in 2 seconds per track. The output data were punched on an "answer card" which contained the 11-digit track-identification number and the above six quantities. Appendix B contains an outline of the calculation of the above quantities from the projected X-Y coordinates.

Since the complete description of each event appeared on an IBM answer card, it was easy to obtain any spectral information about the above six quantities by using the IBM 650. Several programs were written to determine the energy spectra as well as angular distributions in order to check the data.

G. Checks of the Data

In using an instrument in a new manner, or in using new equipment or systems, it is desirable to test the system on a known problem. The study of the d-t neutron spectrum was the main test of our neutron spectrometer system. The results were a check of the range-energy relationship used for protons in liquid hydrogen and also were a test of the track-reconstruction calculation made by the IBM 650.

Since the human element was present in the measurement of all tracks, it was mandatory that the readers be tested to insure that they were being careful when measuring track end points. When the readers' work was repeated without their knowledge, it was found that the difference in successive measurements of the same data resulted in a mean error

no larger than 0.3 Mev in resultant neutron energy. If the readers were given a single track and asked to carefully measure it 10 times, the average error was less than 0.1 Mev. It seemed reasonable to expect the increase in the error in measurement of tracks during normal reading because it was hard to be extremely careful in reading and still measure at a reasonable rate. If we attribute a 0.3-Mev neutron-energy error to an error in the angle measurement alone of the recoil, we find from Eq. (8) ($\frac{dE_n}{E_n} = -2 \tan\theta \, d\theta$) that for a 10-Mev track at 20°, the error in the angle measurement is only about 2°. If the error of 0.3 Mev is attributed to an error in the measurement of the length R alone, then we find from the relationship

$$\frac{dR}{R} = 1.84 \frac{dE_n}{E_n}, \qquad (11)$$

which follows from Eq. (4) and (10), that for a 10-Mev track at 20°, the error in the measurement of the length of the recoil is 0.4 mm in real space or 1.6 mm on the projection screen. These errors appeared to be reasonable for our work.

It was also of importance to find out at which energy the tracks became too short for the readers to measure with 100% efficiency. This lower-energy cutoff was determined in two ways. The first was to have the readers unknowingly measure the same data and then compare the number of tracks observed by each reader in different energy regions. The readers agreed to within 3% down to 7 Mev neutron energy. However, below this energy serious disagreement arose between readers and it appeared that tracks in this energy range were being read with less than 100% efficiency.

The second check on the low-energy cutoff was afforded by a knowledge of the center-of-mass angular distribution of the recoils. Since the c.m. distribution should have been flat, a decrease in efficiency would have been manifested by a falling off of the distribution as the center-of-mass angle increased and as the proton tracks therefore became shorter. Accordingly, an angular analysis in the center of mass was made with the aid of the IBM 650. Into this analysis were put 26,000

tracks available at that time. The angular distributions of the recoils whose neutron energies were between 5 and 7 Mev and 7 and 10 Mev are shown in Fig. 21 A and B, respectively. The horizontal line in the graphs represents the expected flat distribution based on the number of recoils between 0° and 60° in the center-of-mass system (0° and 30° in the laboratory system). The 7- to 10-Mev data were flat out to 90° but the 5- to 7-Mev data appeared to show a monotonically decreasing trend before 60°. Since we were accepting recoils up to 60° in the center-of-mass system, it appeared that the data between 5 and 7 Mev were not complete. Since it was felt that this decrease of reader efficiency would be gradual, the energy spectra were plotted down to 5 Mev in order to look for structure in the spectra. The detection efficiency for this region was estimated to be about 90%.

A reason for acceptance of recoils at angles no larger than 60° c.m. is illustrated in Fig. 21 C and D. The angular distribution of a large sample of target data of neutron energy between 7 and 30 Mev is given in Fig. 21 C. The distribution was fairly flat out to 84°. At about 90° a slight rise appeared. This rise was explained by the data in Fig. 21 D, which shows the results from background data taken with the collimator plugged up (background data). These data indicated a large rise which peaked at 96°, suggesting low-energy neutrons ($\sim$ 6 to 7 Mev) entering the bubble chamber from angles other than the target direction. Most of the background recoils appeared at angles greater than 60° c.m. and thus our acceptance of recoils up to 60° c.m. or therefore 30° lab, was justified.

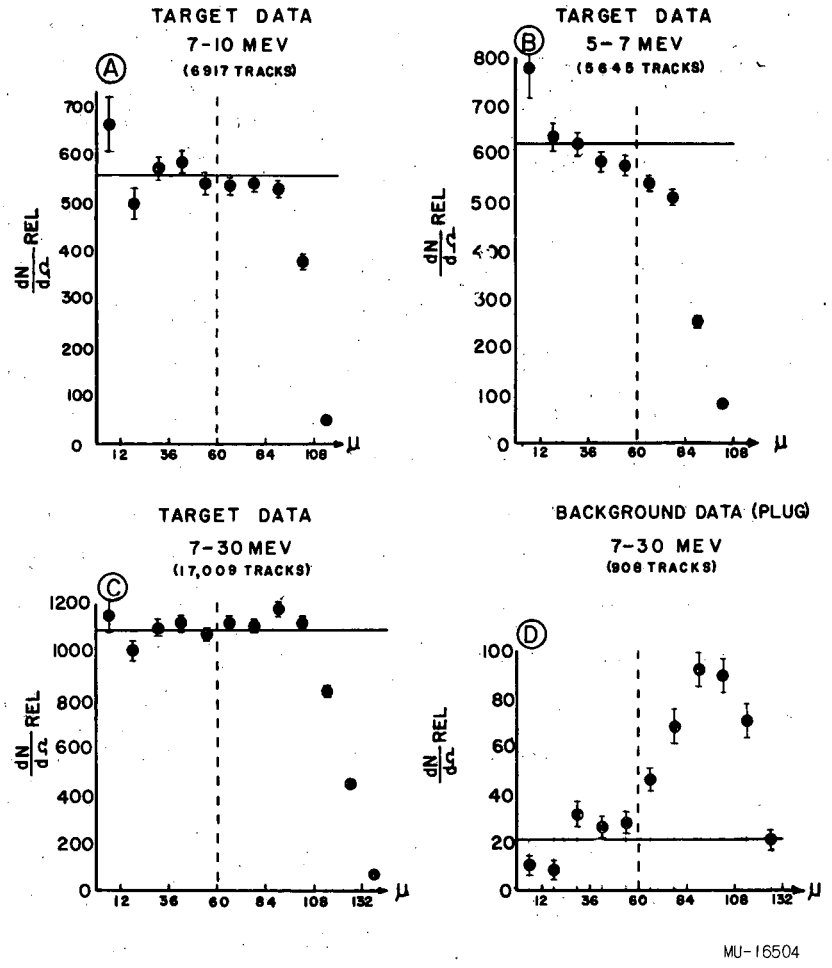

Fig. 21. Angular distributions in c.m. system of recoil protons in the bubble chamber for selected neutron-energy ranges. The horizontal line is the expected distribution on the basis of the number of recoils between 0° and 60° c.m. (30° lab). In determining the energy spectra, we used only tracks recoiling between 0°-and-60° c.m.

IV. CORRECTIONS TO THE DATA

A. Acceptability of Tracks

It has already been indicated that only tracks from neutrons that entered the bubble chamber through the 7/8-inch-diameter entrance window were considered for the final spectra. Figure 22 is a sketch of the chamber and indicates the "sensitive volume" cylinder. The length of cylinder was determined by consideration of the region of good illumination in both views. For a track to be accepted, it had to begin within the "sensitive volume" cylinder. For this reason, Tracks 1 and 2 in Fig. 22 would have been rejected. In the 650-computer program, such a track would have had no answer card calculated for it. On the other hand, a track also had to end before the plane KL so that we would be sure it ended in the chamber. Thus, Track 3 would have been rejected even though it began within the sensitive volume. However, this track would have had an answer card computed, although the card would have had a rejection code number added after the identification to indicate its rejection. Track 4 would have been accepted, since it started within the sensitive volume and ended before line KL. Track 4 would have been rejected, however, if the angle θ were greater than 30°. Its answer card would then have contained a specific rejection number. Thus, any track which began in the sensitive volume had an answer card computed for it, but answer cards representing rejected tracks had rejection code numbers punched on them. Hence, in the final selection of tracks for the compilation of energy spectra, it was easy to sort out the rejected tracks.

The reader in effect looked through 2 inches of hydrogen when he scanned the film, and he could not tell whether or not a track began in the 7/8-inch-diameter sensitive volume (see Fig. 15). He was therefore instructed to read all tracks in the central portion of the chamber. The IBM 650 did the actual rejection and selection of tracks. Approximately one out of every five tracks that were read was finally accepted.

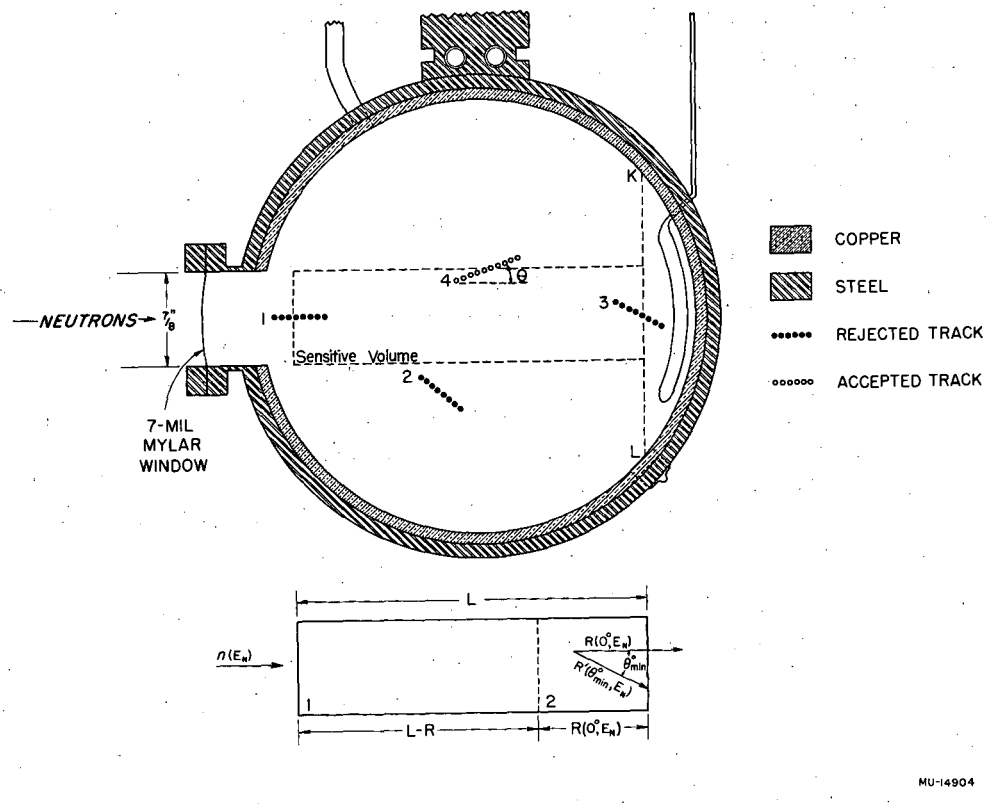

Fig. 22. Diagram of the cross section of the bubble chamber illustrating the region of acceptability ("sensitive volume") of the recoils. The lower sketch illustrates the division of the sensitive volume into two sections for the calculation of the efficiency of the chamber.

B. Instrument-Efficiency Correction

In calculating the absolute efficiency of the bubble chamber for the detection of neutrons of various energies, it was necessary to take into account the variation of the n-p cross section with energy, the decrease of the neutron flux in passage through the hydrogen, the angular acceptance limits of 0° to 30°, and the loss of recoils that started in the sensitive-volume cylinder but ended beyond its limits.

The variation of the n-p cross section is well known, and goes approximately as $1/E$ with energy.[2] The angular distribution of the recoils is approximately $\sin 2\theta$ (lab), which means that one-fourth of all the recoils was between 0° and 30°. Above 10 Mev, the angular distribution of the recoils in the center-of-mass system becomes increasingly non-isotropic, and a semiempirical formula constructed by Gammel[21] was used to describe the angular distribution (see Eq. (7)).

The calculation of the absolute efficiency for a given neutron energy E_n was carried out by dividing the sensitive-volume cylinder into two sections, as is shown in Fig. 22. Section 2 was chosen of length $R(0^\circ, E_n)$ equal to the range of a forward-going proton. Thus Section 1 had a length L-R, so that any recoil that began in this section would stop before the end of the chamber (plane KL). Recoils in Section 2, however, might extend beyond the end boundary if their angle were less than some angle θ_{min} which was a function of position in Section 2. The length of Section 2 became about 25% of the entire length of the chamber (7.20 cm) at 15 Mev, and at this energy the decrease of efficiency because of loss of the recoils that extended beyond the end boundary of the cylinder was no longer negligible. The complete formulation of the efficiency calculation is given in Appendix C.

Figure 23 is a graph of the absolute efficiency versus neutron energy for the detection of neutrons by the 4-inch bubble chamber as it was used in this experiment. The curve has roughly a $1/E$ dependence, but departs from this above 15 Mev because of the loss of tracks that extend beyond the end of the sensitive volume. In order to convert the measured "raw" energy spectrum into the final source spectrum, an IBM 650 computation multiplied the number of recoils in each neutron-energy bin of 0.4-Mev width by the reciprocal of the efficiency for that energy. This computation program also computed the statistical error for each point of the spectrum.

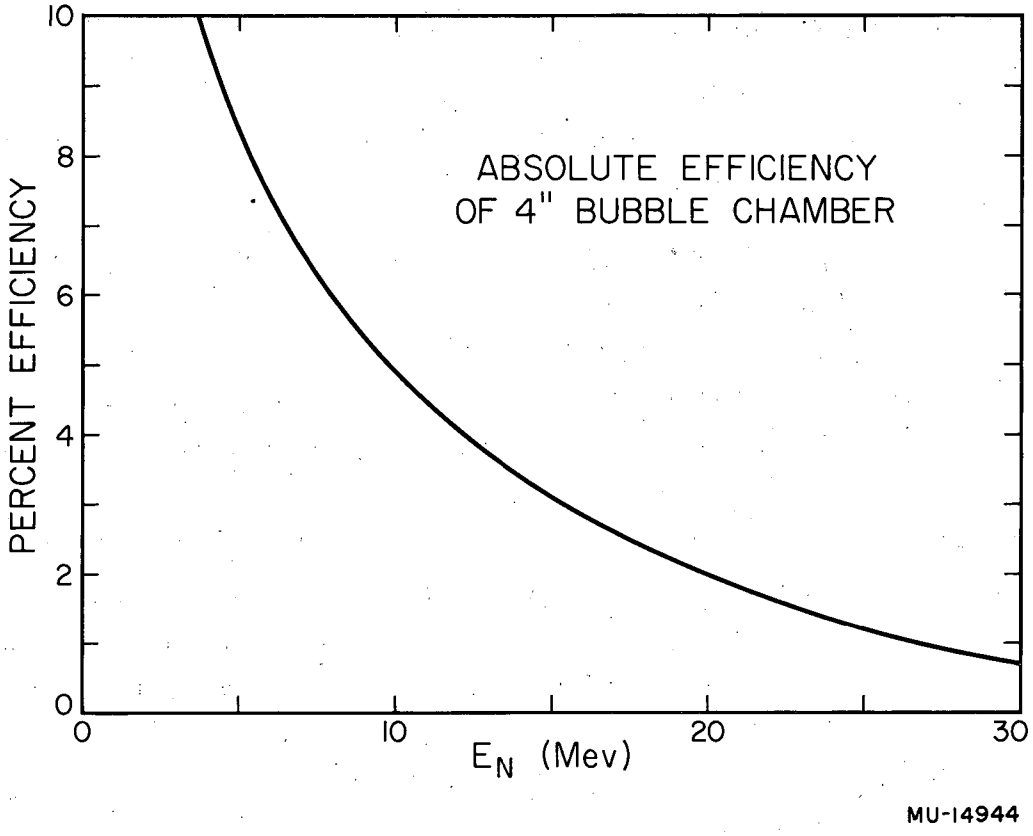

Fig. 23. Absolute efficiency for the detection of neutrons by the 4-inch bubble chamber as it was used in this experiment.

C. The Computation of the Differential Cross Section

The laboratory-system differential cross section per unit energy interval and per unit solid angle for obtaining neutrons of laboratory energy E_n at laboratory angle α from the proton bombardment of thin targets is given by the expression

$$\frac{d^2\sigma}{d\Omega dE_n}(E_n, \alpha) = \frac{N_n(E_n\alpha)}{P\,D\,\Delta\Omega\Delta E_n} \quad , \tag{12}$$

where $N_n(E_n, \alpha)$ is the number of neutrons of energy E_n in energy bite ΔE_n produced in solid angle $\Delta\Omega$ at angle α,

P is the number of protons incident on the target,

D is the number of target nuclei per square centimeter,

and $\Delta\Omega$ is the solid angle subtended by the sensitive volume of the bubble chamber at the target.

P can be determined from the charge collected on the Faraday cup and from the empirical transmission coefficient (k) measured for each target. If C is the beam integrating capacitance in farads and V is the total voltage, then the number of protons that passed through the target is

$$P = \frac{CV}{ek} \quad , \tag{13}$$

where e is the charge of an electron in coulombs.

Since all targets were positioned with their normals at 30° to the beam direction, the number of nuclei per cm^2 for each target was given by

$$D = \frac{TL}{a \cos 30} \quad , \tag{14}$$

where T is the target thickness in g/cm^2,

L is Avogadro's number,

and A is the molecular weight of the target material. The solid angle $\Delta\Omega$ subtended from the target by the sensitive-volume cylinder is given by the product of the cross-sectional area A of the cylinder of 7/8 inch diameter and the average value of the reciprocal of the square of the distance R between the target and the extended cylinder,

$$\Delta\Omega = A\overline{(R^{-2})}.$$

If r_1 and r_2 are the distances between the target and the extremities of the cylinder, then

$$\overline{R^{-2}} = \frac{\int_{r_1}^{r_2} r^{-2}\,dr}{r_2 - r_1} = \frac{1}{r_1 r_2};$$

therefore,

$$\Delta\Omega = \frac{A}{r_1 r_2} = 3.89 \times 10^{-4} \text{ steradian for our geometry.}$$

The number $N_p(E_n, a)$ of acceptable proton recoils generated by neutrons in the sensitive-volume cylinder of the bubble chamber is given by

$$N_p(E_n, a) = \mathcal{E}(E_n)\, N_n(E_n, a) \qquad (15)$$

where $\mathcal{E}(E_n)$ is the absolute efficiency of the bubble chamber for the detection of neutrons of energy E_n.

Substituting Eq. (13), (14), and (15) into Eq. (12), we have

$$\frac{d^2\sigma}{d\Omega dE_n}(E_n, a) = \left\{\frac{eAk \cos 30}{CLT\, \Delta\Omega \Delta E_n}\right\} \frac{N_p(E_n, a)}{V\, \mathcal{E}(E_n)}. \qquad (16)$$

If we designate the quantity in the parenthesis, which was a constant for a given target, as K, then we have

$$\frac{d^2\sigma}{d\Omega dE_n}(E_n, a) = K\, \frac{N_p(E_n, a)}{V\, \mathcal{E}(E_n)}. \qquad (17)$$

An IBM 650 program was used to sort into energy bins the answer cards for all acceptable tracks from a given target at a given angle. The number $N_p(E_n, a)$ of recoils in each bin $E_n + \Delta E_n$ was then multiplied by the reciprocal of the efficiency $\mathcal{E}(E_n)$ for that energy, and by the factor K, and then divided by the total voltage accumulated in these target runs. This yielded the target differential cross section from which the background was subtracted to yield the final differential cross section.

D. Background Subtraction

Background measurements were made by inserting a brass bar into the neutron collimator hole. The data were read and computed exactly as the target data. A cross section was computed in the same manner as the target data. The energy spectra were fairly flat and did not extend above 15 Mev for most of the background data. The magnitude of the background from 5 Mev to 15 Mev was no greater than 10% of the target spectrum. An interesting example of the relative magnitudes and shapes of the target and background spectrum is shown in Fig. 24 for Be^9 at 53°. In this case, because the yield of neutrons from the target increased at higher emission energies, the background reflected this yield with neutrons of energy as high as 26 Mev.

In order to determine the actual cross sections it was necessary to subtract the background spectra from the target spectra. This subtraction implied that the background was beam-dependent. This assumption followed from previous considerations that showed the background was primarily neutrons from the target that were scattered into the bubble chamber by objects in the bombardment area. The spectra given in Section V are those for which the background was subtracted. Before the background was subtracted it was averaged, because it was believed that the background would have a smooth energy distribution. Thus, the subtraction of background from the total yield data did not introduce any structure in the final energy spectra.

In order to determine the nitrogen cross section from the melamine results, it was also necessary to substract the carbon contribution. The melamine data were treated in the following way. We computed the total target cross section $\frac{d^2\sigma_T}{d\Omega dE}_n$, which was defined by the relationship

$$N_n = PD_{14} \left(\frac{d^2\sigma_T}{d\Omega dE_n}\right) \Delta\Omega\Delta E_n \quad , \qquad (18)$$

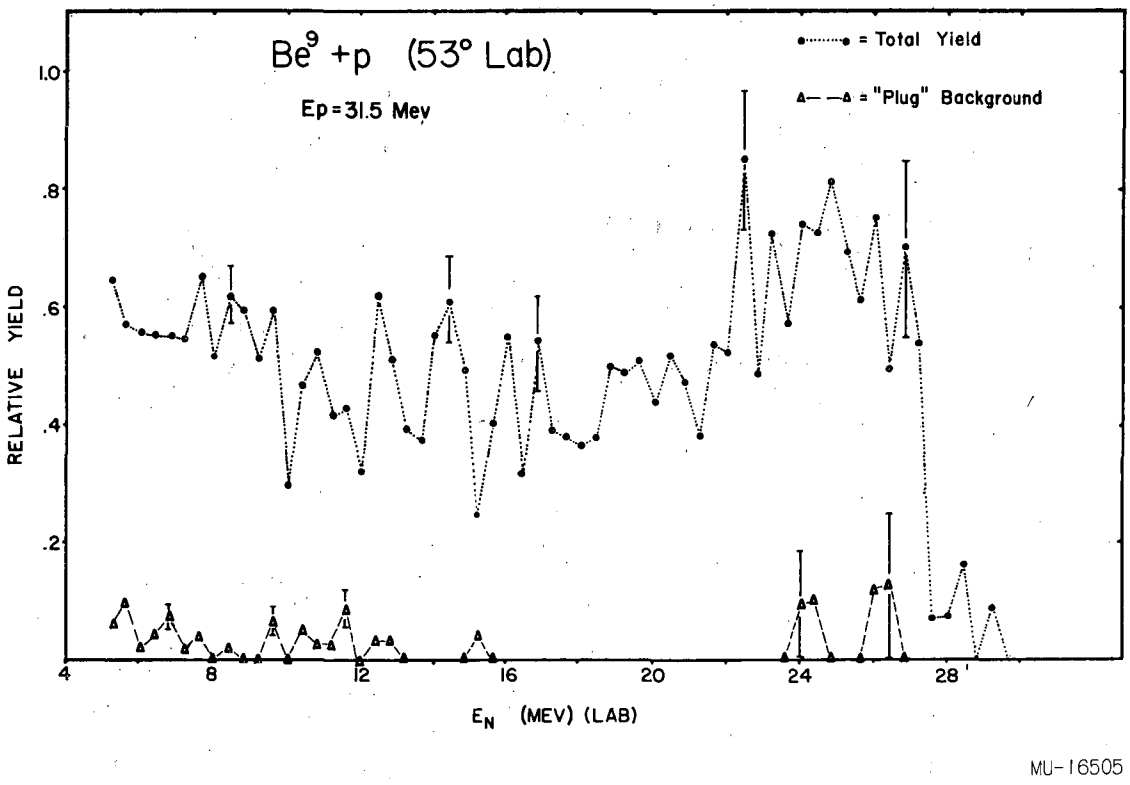

Fig. 24. Comparison of measured target spectrum and "plug" background spectrum for beryllium at 53° lab.

where N_n = total number of neutrons produced in the solid angle $\Delta\Omega$ in ΔE_n,

P = total number of protons passing through the target,

and D_{14} = density of nitrogen-14 nuclei in the target.

The relationship between N_n and the cross sections for neutron production by carbon, $\frac{d^2\sigma_C}{d\Omega dE_n}$, and nitrogen, $\frac{d^2\sigma_{14}}{d\Omega dE_n}$, was

$$N_n = P\left\{D_{14}\left(\frac{d^2\sigma_{14}}{d\Omega dE_n}\right) + D_C\left(\frac{d^2\sigma_C}{d\Omega dE_n}\right)\right\}\Delta\Omega\,\Delta E_n . \qquad (19)$$

From Eqs. (18) and (19) we have

$$D_{14}\left(\frac{d^2\sigma_T}{d\Omega dE_n}\right) = D_{14}\left(\frac{d^2\sigma_{14}}{d\Omega dE_n}\right) + D_C\left(\frac{d^2\sigma_C}{d\Omega dE_n}\right), \qquad (20)$$

and finally

$$\left(\frac{d^2\sigma_{14}}{d\Omega dE_n}\right) = \left(\frac{d^2\sigma_T}{d\Omega dE_n}\right) - \frac{1}{2}\left(\frac{d^2\sigma_C}{d\Omega dE_n}\right), \qquad (21)$$

since D_C/D_{14}, the ratio of the number of carbon nuclei to the number of nitrogen nuclei in melamine ($C_3H_6N_6$), is 1/2. Therefore, in order to obtain the differential cross section of nitrogen-14, it was necessary to subtract one-half the differential cross section of carbon from the total target cross section. The carbon cross section was determined from the polyethylene data in the usual manner.

E. ERRORS

Equation (16) for the differential cross section may be written

$$\frac{d^2\sigma}{d\Omega\, dE_n}(E_n, a) = \frac{k N_p(E_n, a)}{T} \left(\frac{e\, A \cos 30}{\mathcal{E}(E_n)\, C\, L\, V\, \Delta\Omega \Delta E_n} \right).$$

The principal error in the calculation was caused by the uncertainty in the three quantities outside the parenthesis. The quantities inside the parenthesis either were constants or were measurements in which the uncertainty was less than 1%. For the principal errors we have:

a. The error in target thickness T. This varied with the target. For carbon (polyethylene), beryllium, and aluminum, the error was less than 1%, since the targets were cut from foils. For melamine, however, which was an evaporated- and-condensed target, there was an uncertainty of about 5% because the area of the target was slightly irregular.

b. The error in the empirical transmission factor, k, which was about 5%.

c. The error in the determination of the number of recoils, N_p. Here, there are two considerations. There is, of course, the usual counting statistics. There is also the probability that a reader did not observe all recoils. Tests on the readers were made in which they reread data previously completed by themselves and by the other readers. The results showed that for recoils from neutrons of energies about 7 Mev, there was an error no larger than 3% due to unobserved recoils. Between 5 and 7 Mev, the error was estimated to be about 10%. (See Section III G.)

On the basis of these considerations, we concluded that the absolute differential cross section obtained for beryllium and aluminum had an uncertainty, neglecting counting statistics, of less than 10%, while for nitrogen the error was less than 15%. The relative differential cross sections for a given target at the three angles would have smaller errors attached to them.

The final results for the absolute differential cross section were plotted with the probable error resulting from counting statistics shown for each point. When background subtraction was necessary, the final error on each point was determined as the square root of the sum of the squares of the separate counting errors.

F. Center-of-Mass Transformations

Because the targets that were bombarded were light, the center-of-mass system and the laboratory system differed greatly, and conversion of the laboratory-system data was necessary in order to make a meaningful analysis. The formulas for the lab-to-c.m. conversion of energy, angles, and cross section are well known and are only listed here.

Consider the reaction $p + A \rightarrow B + n$. Let the incident energy in the lab system be E_0 for the proton and E_n for the emitted, neutron, and the emission angle of the neutron in the lab system be θ. Designate these quantities in the c.m. system with primes. Then, the following relationships can be derived by applying conservation of energy and linear momentum:

$$\text{(a)}\quad E_n' = E_n + U - 2\cos\theta\,(UE_n)^{1/2}, \tag{22}$$

$$\text{(b)}\quad \sin\theta' = (E_n/E_n')^{1/2}\sin\theta, \tag{23}$$

$$\text{(c)}\quad \frac{d^2\sigma}{d\Omega' dE_n'} = (E_n'/E_n)^{1/2}\,\frac{d^2\sigma}{d\Omega dE_n}, \tag{24}$$

and

$$\text{(d)}\quad \frac{d\sigma}{d\Omega'} = \frac{E_n'}{E_n}\left(1 - \frac{U}{E_n'}\sin^2\theta\right)^{1/2}\frac{d\sigma}{d\Omega}, \tag{25}$$

where

$$U = \frac{M_p M_n}{(M_p + M_A)^2}\,E_0 .$$

V. RESULTS AND DISCUSSION

A. Nitrogen-14

The experimental cross sections for the production of neutrons at the laboratory-system angles of 53°, 90°, and 127° by the 31.5-Mev proton bombardment of N^{14} are plotted versus laboratory-system neutron energy in Fig. 25. While the data extend down to 5 Mev neutron energy (lab), it is believed that the absolute values of the differential cross section may be as much as 10% low between 5 and 7 Mev because of incomplete detection by the reader of the shorter recoil tracks. (See Section III G.)

The production of neutrons from N^{14} was strongly peaked forward, and structure can be seen in the energy spectra. The (p,n) reaction on N^{14} leads to O^{14} with a Q value of -5.952 Mev.[18] This reaction was investigated with 17.3-Mev protons and nuclear emulsions by Ajzenberg and Franzen at 30°, 60°, 90°, and 150°.[35] In their work, they were able to detect neutron groups corresponding to broad nuclear levels in O^{14} at excitation energies of 6.2, 7.5, and 9.3 Mev as well as a weakly produced ground-state group. Absolute cross sections were not determined. Their work represented the only information on the level structure of O^{14}.

Our bombarding energy allowed investigation of O^{14} up to an excitation of 18 Mev. In order to facilitate the examination of the energy spectra for level information, the energy spectra were replotted on a center-of-mass neutron energy scale. These data are shown in Fig. 26. The vertical lines labeled g.s., 1, 2, and 3 represent the expected positions for neutron groups leading to the ground state and the first, second, and third excited states of O^{14} on the basis of the previous investigation.[35] Also indicated is the threshold for the (p,pn) reaction leading to N^{13}. The neutron spectrum from this reaction, which leads to a three-body final state, would be expected to rise smoothly with decreasing neutron emission energy.

Neutron groups leading to the first, second and third excited states of O^{14} were observed at all three angles. The 17-Mev neutron group (first excited state) appeared strongly at 53° but relatively weakly at 90° and 127°. The second and third groups were not separated at 53°, while they

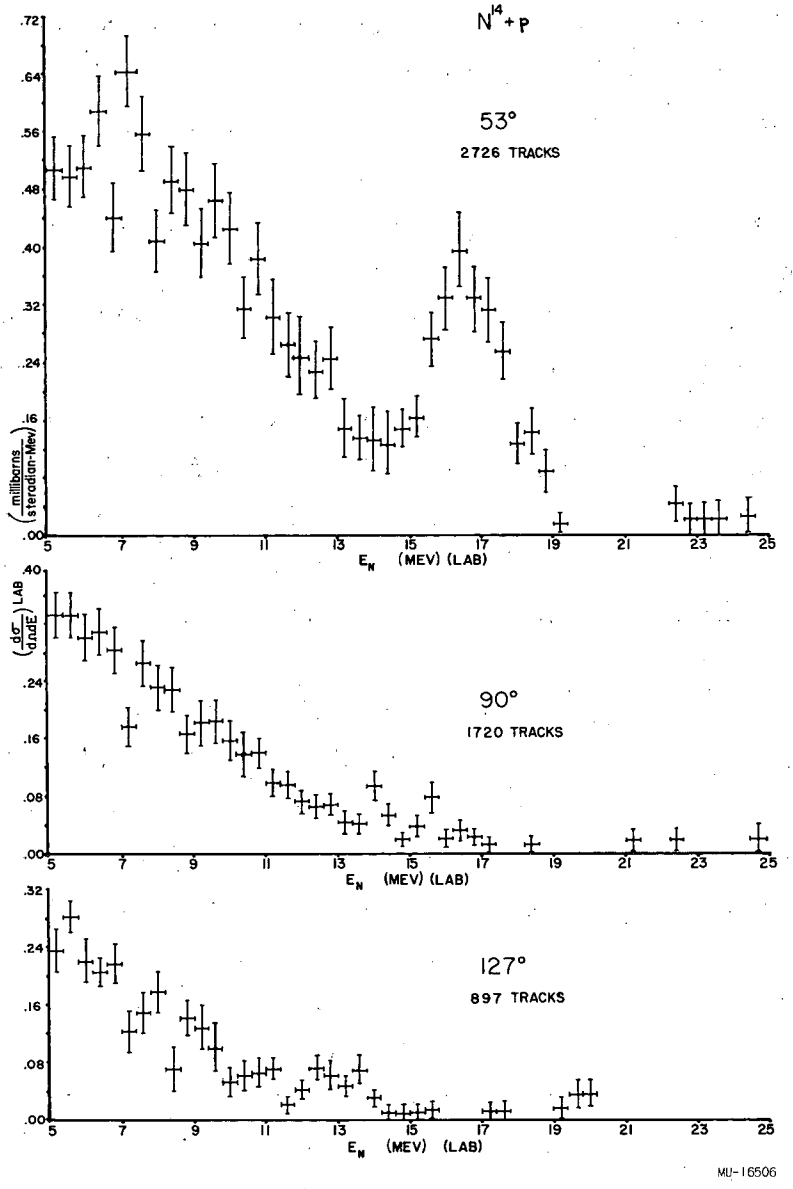

Fig. 25. Differential cross sections for the production of neutrons at 53°, 90°, and 127° (lab) by the 31.5-Mev proton bombardment of N^{14}. Errors shown are statistical probable errors.

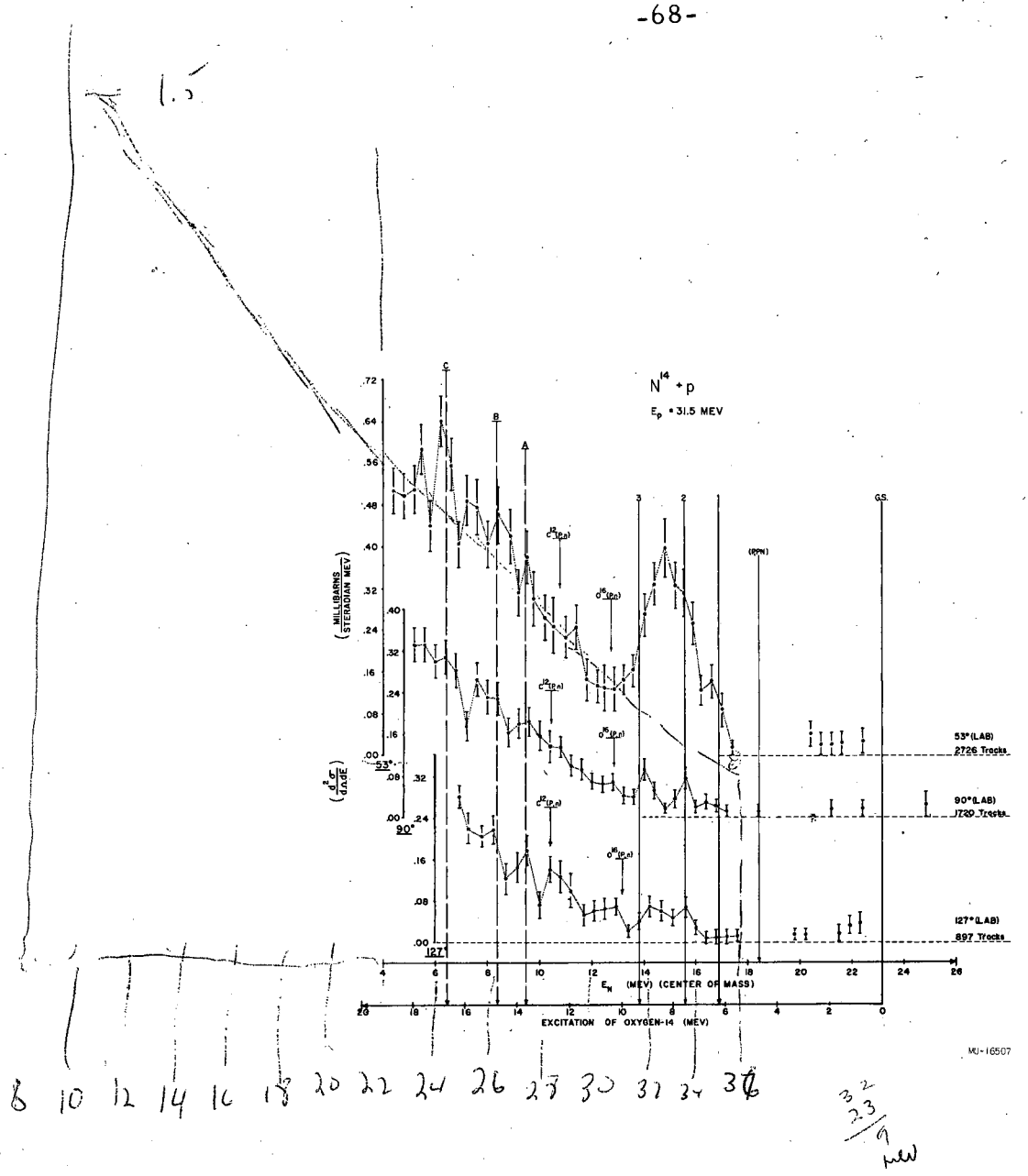

Fig. 26. Neutron energy spectra at the three angles of observation from the 31.5-Mev proton bombardment of N^{14}. The spectra are plotted versus the center-of-mass energy of the emitted neutron.

were at 90° and 127°. It is possible that a neutron group leading to an unknown level between the second and third was produced strongly at 53°, but this cannot be determined from the data. The energy of 9.3 Mev assigned to the third level of O^{14} by Ajzenberg and Franzen seems from our work to be about 0.2 Mev too high, but the difference is not significant.

No neutron group appeared correlated to the ground state although some scattered production appeared at a few Mev lower. It is not believed that these neutrons belong to the ground-state group. If they did, it would indicate either that the Q for the (p, n) reaction of -5.952 Mev is in error by 1 Mev or more, or that there was at least a 5% error in our range-energy relationship for protons in liquid hydrogen. It is extremely doubtful that the Q value is in error, since the previous (p, n) work,[35] several beta-decay results,[36-38] and a recent $C^{12}(He^3, n)O^{14}$ threshold experiment[39] agree quite well in their determination of the mass defect of O^{14}. It is also doubtful that our range-energy relationship could be in error by more than 1%, since the peak of the neutron group from the d-t reaction was measured at 14.1 ± 0.1 Mev, in good agreement with the expected energy. Examination of energy spectra from proton recoils occurring anywhere in the bubble chamber and at angles up to 45° leads us to believe that the ground-state group was not produced with sufficient strength to be observed. This would mean that the differential cross section for the production of neutrons leading to the ground state of O^{14} at the laboratory angles observed was less than 0.01 millibarn per steradian.

Estimates were made of the differential cross sections for the production of these neutron groups at the three angles. Because of the poor separation of these groups, the values assigned have probable errors from 20% to 40%. When the neutron groups were not separated, profiles of width corresponding to the measured resolution of the system were drawn about the energy of the expected group corresponding to a given level, and the areas under these curves were calculated. All neutron production was assumed to have come from the (p, n) reaction. The energy range in consideration was near the (p, pn) threshold, at which

point little (p, pn) neutron production was expected. Table III lists the center-of-mass differential cross section for the production of these levels as well as the center-of-mass angle of measurement.

Table III

Center-of-mass differential cross section and angle of observation for $N^{14} + p \rightarrow n + 0^{14*}$, $E_p = 31.5$ Mev

	*Level of 0^{14}			
Angle (lab system)	Ground state (mb/sterad)	1st(6.2 Mev) (mb/sterad)	2nd (7.5 Mev) (mb/sterad)	3rd (9.3 Mev) (mb/sterad)
53°	<0.01 (55°)	0.12 (57°)	0.42 (57°)	0.37 (58°)
90°	<0.01 (92°)	0.03 (93°)	0.05 (93°)	0.07 (93°)
127°	<0.01 (131°)	0.02 (131°)	0.08 (131°)	0.08 (132°)

There are two contaminant (p, n) reactions that might appear in the data. They are $C^{12}(p,n)N^{12}$ (Q = - 18.5 Mev) from the carbon in the melamine ($C_3H_6N_6$), and $0^{16}(p,n)F^{16}$ (Q = - 16.7 Mev) from oxygen which seems always to be present when one does nuclear spectroscopy. Although a polyethylene target was bombarded in order to make a carbon subtraction from the total yield of the melamine target and thus obtain the nitrogen contribution, the amount of carbon data obtained was small (100 to 200 tracks at each angle). Hence the carbon data were first averaged and then subtracted. This would permit some structure from the $C^{12}(p,n)$ reaction to remain in the $N^{14}(p,n)$ yield if the carbon reaction proceeded strongly. However, it was expected from Millburn's measurement of total neutron production from the bombardment of thick targets by 32-Mev protons[23] that the production from carbon would be only 1/5 of that from nitrogen, and because there were twice as many nitrogen nuclei as carbon nuclei in melamine, the effective yield of carbon relative to nitrogen should have been about 10%. The average laboratory-system cross sections for

the production of neutrons above 5 Mev for carbon were 0.100 mb/sterad-Mev, 0.064 mb/sterad-Mev, and 0.047 mb/sterad-Mev for 53°, 90°, and 127° respectively. Using Eq. (21), one had only to subtract one-half the average values for carbon from the total melamine yield in order to obtain the nitrogen contribution. The threshold for the $C^{12}(p,n)$ reaction is indicated in Fig. 26, at each angle. It does appear that there is a neutron group near the threshold at each angle. However, the production seems to be too strong to be a carbon contribution alone. It may be possible that there is structure from the $N^{14}(p,n)$ reaction in this region coinciding with the carbon threshold, but the data are not good enough to resolve this question. Such a transition would correspond to an O^{14} excitation of about 12.4 Mev.

The other contaminant reaction, $O^{16}(p,n)F^{16}$, was expected to produce few neutrons compared with the nitrogen contribution because it was believed that there would be little oxygen contamination in the melamine target and because Millburn's work indicated that the thick-target (18 to 32-Mev) cross section for oxygen was less than one-tenth the value for nitrogen. The target probably contained some oxygen because of an acrylic that had been sprayed on it to give it strength. The $O^{16}(p,n)$ thresholds at the three angles are shown in Fig. 26. There appears to be some production at 127°, which may correspond to the oxygen reaction.

The three neutron groups in Fig. 26 labeled with letters are believed to represent transitions to previously unknown levels in O^{14}. A neutron group was considered to signify a possible transition to a level in O^{14} when it appeared at two angles at the proper center-of-mass energy. Table IV lists these three groups with their obser ed center-of-mass energies and the corresponding excitations of O^{14}. Since the data points had an energy width of 0.4 Mev, the error assigned to the energy of each level was ± 0.2 Mev. In terms of nuclear spectroscopy, these levels must be considered broad because of instrument resolution and poor statistics. Group C seems well established from the data at 53° and 90°, although the energy spectrum at 127° ends before this group because of the center-of-mass shift.

Table IV

Neutron groups corresponding to possible levels in O^{14};

$$N^{14} + p \rightarrow n + O^{14*}, \quad E_p = 31.5 \text{ Mev}$$

Group	E_n (Center of Mass) (Mev)	Excitation of O^{14} (Mev)
A	9.5	13.6
B	8.4	14.7
C	6.5	16.6

The total cross sections for the production of neutrons of energy greater than 5 Mev in the laboratory system at the three angles of observation were calculated and are listed in Table V for all three targets. The statistical error was less than 4%.

Table V

Cross sections for production of neutrons of energy > 5 Mev by 31.5-Mev proton bombardment of N^{14}, Be^9, and Al^{27}

	Differential cross sections (mb/sterad)			Estimated total cross section (E_n>5 Mev) (mb)	Thick-target total cross section (18 to 32 Mev) (Millburn) (mb)
N^{14}	4.56	1.68	1.05	32	108
Be^9	11.7	2.9	2.6	78	339
Al^{27}	5.2	3.0	1.19	39	234

An estimate of the total cross section for neutron production at energies greater than 5 Mev was made by assuming that the 53° data represented the average differential cross section for the forward hemisphere while the 127° data were the average for the backward sphere. This estimate for all three targets is also listed in Table V. On the basis of this assumption, the total cross section ($E_n > 5$ Mev) for N^{14} was about 32 millibarns. This represented about one-third the total production of neutrons determined by Millburn for a thick target (18 to 32 Mev).[23]

In 1937, Wigner introduced the concept of isotopic spin T of nucleons.[40] This quantity would be a "good quantum number" if nuclear forces were charge-independent, i.e., if the n-n, p-p, and n-p forces were equal. The principle of charge independence now seems well established.[2] Application of this principle through the concept of isotopic spin allows predictions to be made about the energy levels of isobaric nuclei.

The isotopic spin T (sometimes called isobaric spin[41]) of a nucleon is defined as a vector quantity in a manner completely analogous to the spin angular momentum of fermions. A nucleon has isotopic spin $T = 1/2$. The Z projection of the vector T in isotopic spin space represents the charge of the nucleon and is defined so that T_z is $+1/2$ for the neutron and $-1/2$ for the proton.* Thus a nucleus composed of Z protons and A-Z neutrons would have

$$T_z = 1/2(A-2Z). \qquad (26)$$

It follows from conservation of charge that T_z is conserved in a nuclear reaction. The scalar quantity T^2 is conserved if the Hamiltonian is charge-independent. While this cannot be strictly true, because of the Coulomb charge associated with protons, it is a good approximation for light nuclei.

*This is the formalism prevalent in nuclear spectroscopy.[41] The opposite assignments of $T_z = +1/2$ for the proton and $-1/2$ for the neutron are made in high-energy nuclear physics.

For isobaric nuclei of even-A mass number, the possible values of T are integral and the simplest cases would have T = 0 or 1. Such a case is the mass-14 triad, C^{14}:N^{14}:O^{14}. Figure 27 presents the energy-level scheme of this triad (first-order electrostatic energy differences and the intrinsic (N-H) mass differences removed). The data are from Lauritsen and Ajzenberg-Selove.[42] Also shown for O^{14} are the possible levels (labeled with letters) observed in our work. N^{14} (7 protons, 7 neutrons) is a $T_z = 0$ nucleus while C^{14} has $T_z = +1$ and O^{14} has $T_z = -1$. It is plausible to assume that the ground state of each nucleus will assume the lowest possible I-spin value. Hence, the ground state of N^{14} should be a $T = 0$ state, while the ground states of C^{14} and O^{14} should be $T = 1$ states since $|T_z| = 1$ for the latter two nuclei.

It follows from the assumption of charge symmetry of nuclear forces that there are exactly the same number of levels with the same excitation energies (neglecting electrostatic energy and the n-H mass difference) in the mirror nuclei $T_z = \pm 1$. (Mirror nuclei are those for which the numbers of protons and neutrons are interchanged.) Furthermore, from the assumption of charge independence of nuclear forces, all the levels of the $T_z = 1$ nucleus will also occur in the $T_z = 0$ nucleus. However, the $T_z = 0$ nucleus has additional levels (isobaric spin singlets) without equivalents in the $T_z = \pm 1$ nuclei because of the Pauli exclusion principle. For our case, the levels in C^{14} and O^{14} must have total isobaric spin values greater than zero, while N^{14} has not only those levels but also $T = 0$ levels. Thus the ground state of N^{14}, which is a (1^+) $T = 0$ level, is an isobaric singlet state and has no analog in O^{14} and C^{14}. But the 2.31-Mev level in N^{14} is the corresponding isobaric triplet member of the (0^+) $T = 1$ ground states of O^{14} and N^{14}. The first three excited states of C^{14} appear to correspond to odd-parity levels of N^{14}, [42] and it is probable that the first excited state (6.2 Mev) of O^{14} is an analog of one of these, as may also be the 7.5-Mev level. This possibility may be a clue to explaining the relatively strong (p, n) transition to the excited states of O^{14} as compared to the ground-state transition. The ground-state transition for the

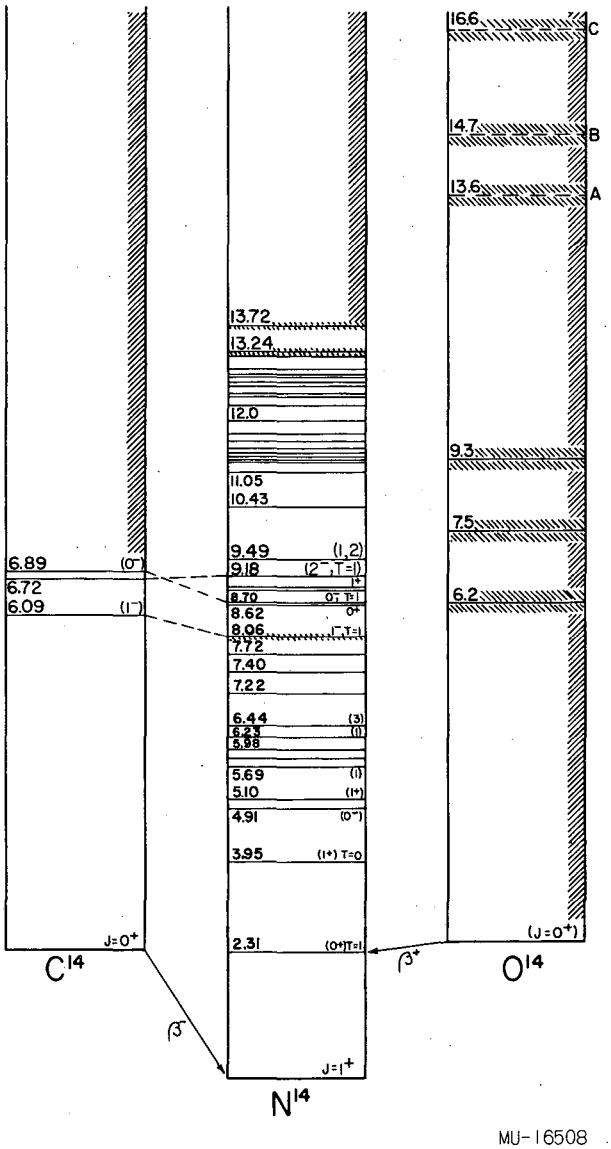

Fig. 27. The energy-level scheme of the C^{14}-N^{14}-O^{14} triad. The Coulomb energy differences and the (N-H) mass differences have been removed. The data are from Lauritsen and Ajzenberg-Selove.[43] Also indicated for O^{14} are the possible levels A-C observed in this experiment.

$(J = 1^+)$ N^{14} ground state to the $(J = 0^+)$ 0^{14} ground state would involve no parity change between the initial and final nuclear states, while the transition to the excited levels may involve a parity change. The direct-surface-interaction theory of Austern et al. predicts an angular distribution of the (p,n) reaction of the form[9]

$$\frac{d\sigma}{d\Omega} \sim \sum_{\ell} A_{\ell} \left(j_{\ell}(qr)\right)^2 , \qquad (27)$$

where ℓ, the orbital angular momentum absorbed by the nucleus, is given by

$$J_0 + J_F + 1 \gg \ell \gg \left| \vec{J}_0 + \vec{J}_F + \vec{1} \right|_{min} , \qquad (28)$$

and J_0 and J_F are the total-angular-momentum states of the initial and final nuclei. The change in wave number, q, between the incoming proton and outgoing neutron is given by

$$q = k_p^2 + k_n^2 - 2k_p k_n \cos\theta .$$

The effective radius at which the interaction occurs is represented by r, and j_{ℓ} is the spherical Bessel function of order ℓ. Conservation of parity further restricts the value of ℓ to odd integers for a change in parity between initial and final nuclear states, and to even integers for no change in parity.

Thus in our ground-state transition the lowest allowed ℓ value would be $\ell = 0$ while, for transitions to the first excited level, $\ell = 1$ would be the minimum. The theoretical angular distributions have been plotted for the ground-state transition and the first-excited-state transition by using the above ℓ values and a radius r arbitrarily chosen at $1.4\ A^{1/3}$ fermis. The distributions are shown in Fig. 28. Curve A is the distribution for the excited-state transition; it has been normalized to the observed 53° differential cross section. Curve B is the angular distribution for the ground-state transition. It has been normalized so as to make the total production of this transition equal to the total production of the excited-state transition, which was calculated to be 1.57 millibarns under the

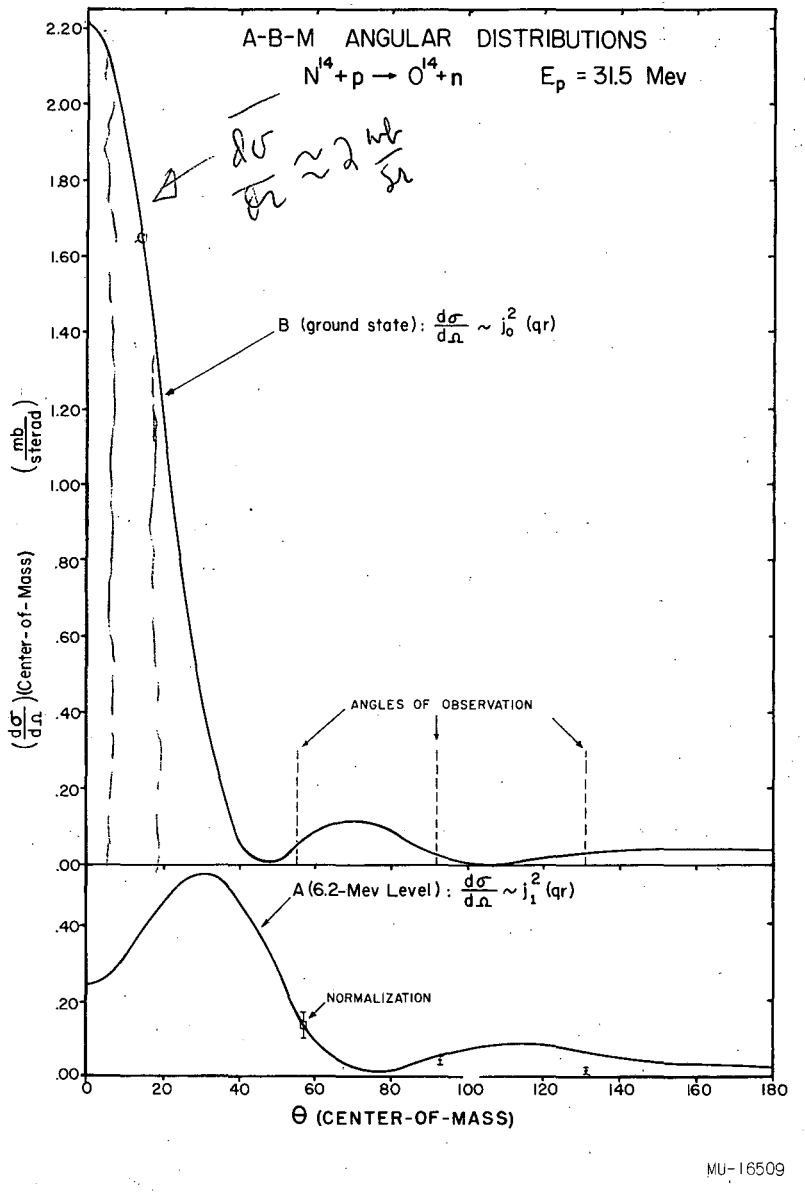

Fig. 28. Comparison of the angular distributions from the Austern-Butler-McManus direct-interaction theory for the reaction $N^{14}(p,n)\,O^{14}$. The radius of interaction r used was $1.4A^{1/3}$ fermis.
Curve A: A-B-M distribution for transition to first excited state (6.2 Mev) of O^{14}. The curve is normalized to the 53^{o}(lab) measurement.
Curve B: A-B-M distribution for transition to ground state of O^{14}. This curve is normalized so that total production described by this curve is equal to total production described by Curve A (1.57 mb).

assumption that the angular distribution was given by Curve A. It can be seen that the ground-state angular distribution is near its minimum at the forward experimental observation angle of 57° (c.m.). However, the j_1^2 distribution for the excited-state transition has a value well above its minimum at the measured forward angle. On the basis of this argument, it would appear that our observation at 53° was not forward enough to detect the major portion of the ground-state transition. Furthermore, the neutrons found near the expected position of the ground-state group might have resulted from scattering of the forward-produced ground-state group from, say, the target holder.

B. Beryllium

The experimental neutron-production cross section versus laboratory neutron energy for the 31.5-Mev proton bombardment of Be^9 is shown for the three observation angles of 53°, 90°, and 127° (lab) in Fig. 29. The spectra indicate considerable structure, and the yield at the forward angle at high neutron-emission energies is quite large. The (p,n) reaction of Be^9 leads to the residual nucleus B^9. Because this is the only reaction that leads to a two-body final state in which neutrons are produced, it is plausible to relate the structure in the energy spectra to levels in B^9. The Q for the (p,n) reaction is -1.851 Mev.[18] Neutrons can also be produced by the (p,pn) reaction (Q = 1.666 Mev)[18] and the (p,αn) reaction (Q = - 3.37 Mev).[42] However, the latter two reactions result in three-body final states and are not likely to produce neutron groups at the same c.m. energy at the different angles of observation.

Our knowledge of the level structure of B^9 is small. A (p,n) experiment utilizing nuclear emulsions and 6.59-Mev protons indicated an excited state at 2.37 Mev as well as yielding the ground-state neutron group.[43] A later (p,n) experiment,[44] using the "counter ratio" technique to determine the threshold energy for the production of a level, indicated a broad maximum in the yield of neutrons which could be due to the three-body breakup reaction Be^9 (p,pn)Be^8 or to a broad even-parity state in B^9 at 1.4 Mev. The 2.3-Mev level was also observed. Thus only one certain level and one possible level in B^9 are known.

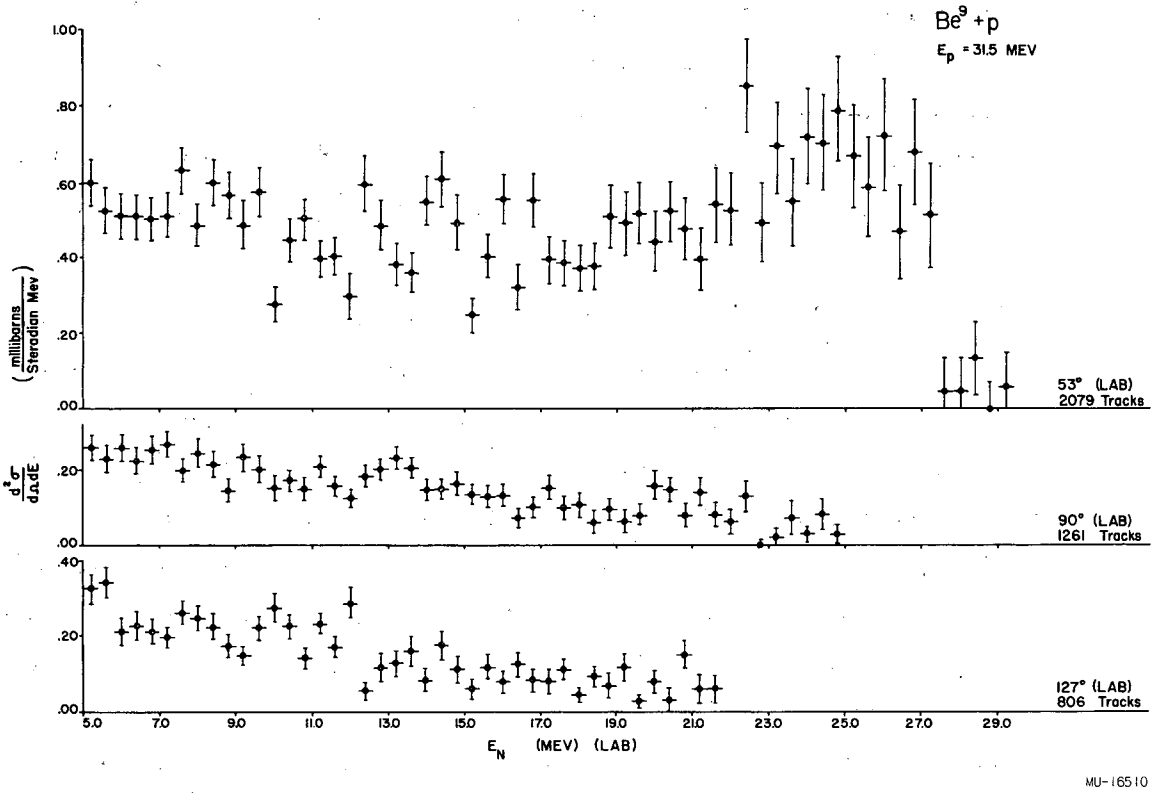

Fig. 29. Differential cross sections for the production of neutrons at 53°, 90°, and 127° (lab) by the 31.5-Mev proton bombardment of Be^9. Errors shown are statistical probable errors.

The experimental energy spectra have been replotted versus the center-of-mass energies of the neutrons in Fig. 30. The expected position of neutron groups leading to the ground state and the first and second excited states of B^9 are marked by vertical lines. No neutron group appears correlated to the ground-state transition; it is possible that a weak production of the 1.41-Mev "level" occurred at 53°. The transition to the 2.37-Mev level was produced quite strongly at 53° and occurred weakly at 90° and 127°.

The contaminant reaction $O^{16}(p,n)F^{16}$ should be considered, since the beryllium target undoubtedly had a covering of the oxide. Millburn's measurements[23] indicated that the thick-target (18- to 32-Mev) total neutron-production cross section for oxygen was only 20% of the beryllium value. Hence it was not believed that the contaminant would affect the spectra greatly. The threshold for the $O^{16}(p,n)$ reaction (Q = - 16.7 Mev)[18] is indicated for each angle in Fig. 30. Although there appears to be a peak correlated at each angle with this threshold, it also appears that the strong 53° and 90° groups may be correlated to a strong 127° group which is not from the $O^{16}(p,n)$ reaction. It is believed that these 53° and 90° groups were produced primarily by a $Be^9(p,n)B^{9*}$ transition.

A neutron group was considered to signify a transition to a possible level in B^9 when the group appeared at two angles at the same center-of-mass energy. Since the data carry large statistical errors, these level assignments are uncertain and, consequently, we have referred to them only as "possible" levels. These selected groups are marked in Fig. 30 with dashed vertical lines labeled with letters. The selected neutron groups and the corresponding excitations in B^9 are listed in Table VI. Since the data points have an energy width of 0.4 Mev, the assignment of energies to these levels carries an error of at least ± 0.2 Mev. In terms of nuclear spectroscopy, all these levels must be considered broad because of the instrument resolution and the poor statistics. However, the levels of B^9 probably are broad since they are expected to have short lifetimes because the ground state itself is proton unstable.

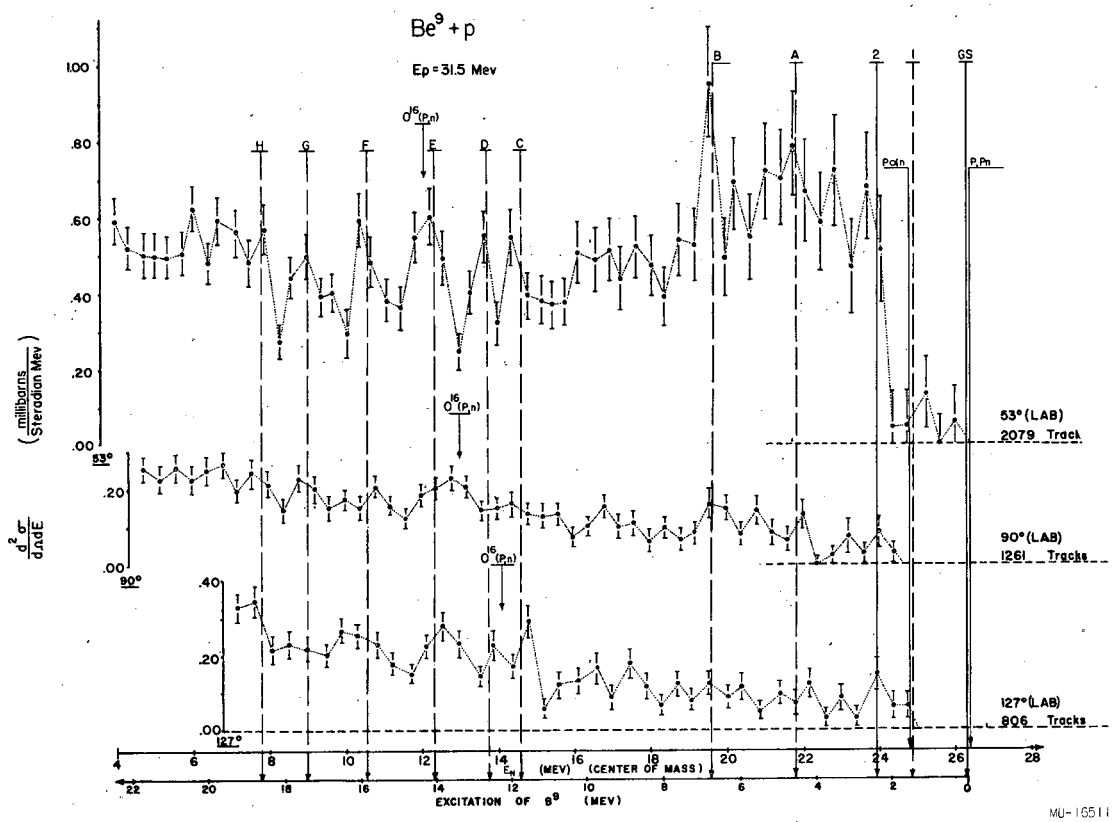

Fig. 30. Neutron energy spectra at the three angles of observation from the 31.5-Mev proton bombardment of Be^9. The spectra are plotted versus the c.m. energy of the emitted neutron.

Table VI

"Possible" Levels of B^9

Neutron Group	E_n(c.m.) (Mev)	B^9 excitation (Mev)
A	21.9	4.4
B	19.6	6.7
C	14.6	11.7
D	13.7	12.6
E	12.3	14.0
F	10.6	15.7
G	8.9	17.4
H	7.8	18.5

B^9 (5 protons, 4 neutrons) is the $T_z = -1/2$, mirror nucleus of Be^9 (4 protons, 5 neutrons; $T_z = +1/2$). Since the number of neutron-proton pairs in each of these nuclei is the same, it is necessary only to assume a charge symmetry (i.e., n-n = p-p) and not a charge independence (n-n = n-p = p-p) of nuclear forces in order to obtain correspondence of the nuclear states of these mirror nuclei. The energy-level scheme of B^9, including the observed "possible" levels is shown in Fig. 31 along with the known level scheme of Be^9 and the position of the ground state ($T = 3/2$, $T_z = -3/2$) of Li^9. The electrostatic energy and the n-H mass differences have been removed in this representation of the mass-9 isobaric nuclei. These data were taken from a review of the levels of light nuclei by Lauritsen and Ajzenberg-Selove.[42] Also plotted in Fig. 31 is the intermediate-model level scheme for mass-9 nuclei from work by Kurath.[45]

The intermediate model is essentially an interpolation between the extremes of the jj-coupling shell model and the LS-coupling model.[41] In the jj-coupling model, the orbital angular momentum ℓ and the spin s of each nucleon are coupled to give a total angular momentum number j of the individual nucleon which is a "good quantum number" and which adds vectorially with the j values of the other nucleons to yield the total angular momentum J of the nucleus. In the LS-coupling scheme or "Russell-Saunders Coupling," as it is known in the analogous atomic problem, the orbital angular momentum ℓ of each nucleon adds to yield a total orbital angular momentum L as does the spin s of each nucleon to give a total spin angular momentum S of the nucleus. L and S are both "good quantum numbers" and couple to give the total angular momentum J of the nucleus. In the intermediate model, a parameter "a" is used to measure the strength of spin-orbit coupling (jj model), and the parameter "K" is used to measure the "exchange integral" of the nucleus and thus determines the amount of LS coupling. The ratio of a/K determines the degree of interpolation of the intermediate model between the two extremes. A ratio of $a/K \approx 0$ represents pure LS coupling while $a/K \gtrsim 10$ is pure jj coupling. The theoretical energy-level scheme for mass-9 nuclei shown in Fig. 31 was computed with an a/K value of 1.5, which is close to the pure LS coupling extreme. This value gave the best fit to the existing data.[45]

The 2.43-Mev level in Be^9 and the 2.37-Mev level in B^9 are probably isobaric pairs.[42] The level in Be^9, on the basis of recent data,[46] has the probable spin and parity assignment of $5/2^-$. The energy and spin of this level appear to be in good agreement with the intermediate coupling model. Several of the "possible" levels of B^9 observed in this experiment are in good energy agreement with known levels in Be^9. Level C at 11.7-Mev excitation of B^9 corresponds quite well with the 11.3-Mev state of Be^9. The 17.4-Mev (G) level, the 18.5-Mev (H) level, and the 6.7-Mev (B) level appear to correspond to known states of Be^9. Level F at 15.7-Mev excitation of B^9 lines up exceedingly well with the expected position of the T = 3/2 analog, with the ground state of Li^9, and with its predicted position on the intermediate-model scheme. The

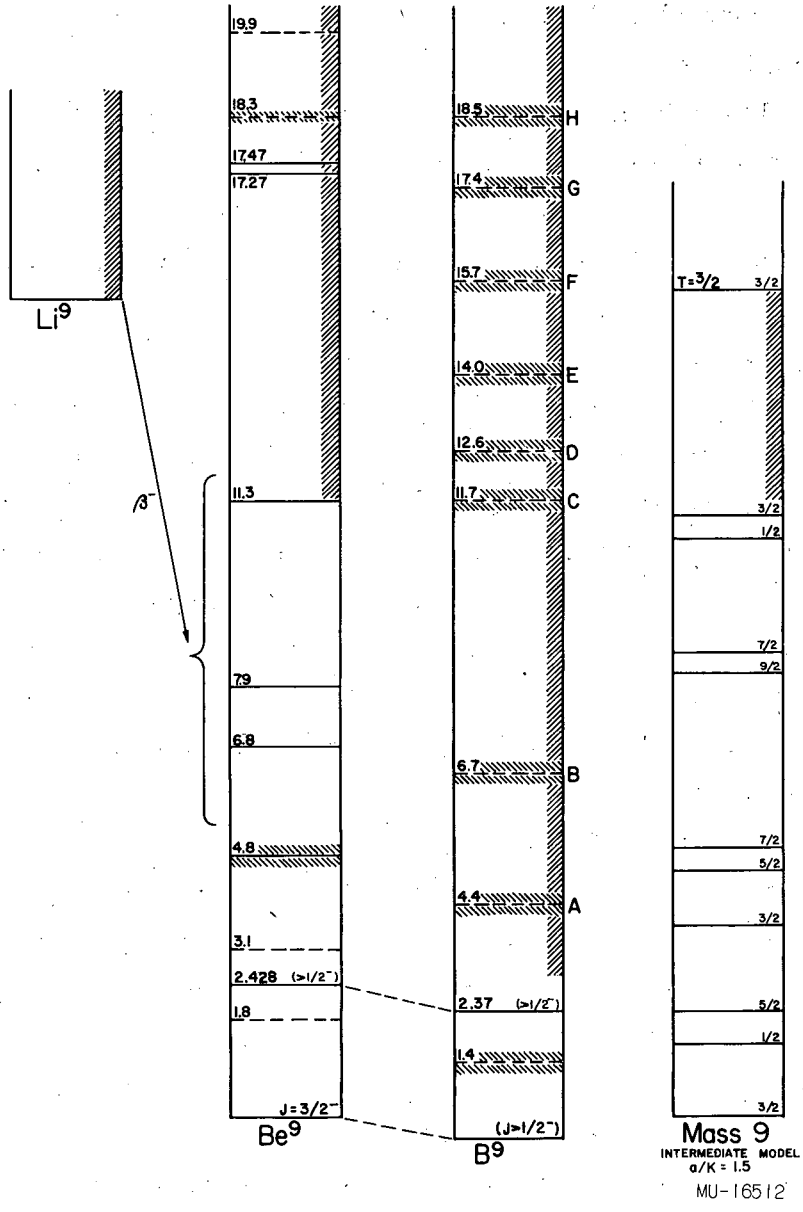

Fig. 31. Energy-level scheme for the mass-9 polyad. The Coulomb energy differences and the n-H mass differences have been removed. The data are from Lauritsen and Ajzenberg-Selove.[42] Also shown is the intermediate coupling model predictions by Kurath[45] for the level scheme of the mass-9 nuclei. The "possible" levels of B^9 (A through H) observed in this experiment are also shown.

theoretical equivalence of this pair of levels would be based on charge independence and not charge symmetry of nuclear forces, since the number of n-p pairs in Li^9 is not the same as the number in Be^9 and B^9. No corresponding level has been found in Be^9, but the region has not been fully explored.

The angular distribution of the emitted neutrons is peaked forward at all neutron energies, probably indicating a direct-interaction mechanism. The differential cross sections for the production of neutrons of laboratory-system energy greater than 5 Mev at the three angles of observation are listed in Table V. If one assumes that the 53° figure represents the average value for the forward hemisphere and the 127° data represent the average value for the backward hemisphere, then one can calculate the total cross section for the production of neutrons of energy greater than 5 Mev to be about 78 millibarns. This would be about one-fourth the total thick-target (18- to 32-Mev) cross section measured by Millburn.

The shape of the forward-angle energy spectrum is quite different from that usually observed for neutron-emission spectra. The yield at the forward angle apparently increases with neutron-emission energy, which once again might indicate a direct surface interaction in which the core of the target nucleus is not highly excited. Consequently, the reaction would proceed preferentially to the lower levels of the residual nucleus (B^9). It should be noted, however, that the ground-state transition was not observed. If one assumes that the 2.37-Mev level of B^9 has the same spin and parity ($5/2^-$) as the 2.43-Mev level of Be^9, then the ground-state transition and the 2.37-Mev level transition both involve no parity change. From a direct-interaction viewpoint, the selection rule (Eq. (28)) would allow j_0^2 and higher terms in the angular distribution for both these transitions, and thus it would appear that the angular distribution alone could not explain the enhancement of the 2.37-Mev transition over the ground-state transition at our angles of observation.

Aluminum

The experimental results for the aluminum bombardment are plotted versus laboratory-system neutron energy in Fig. 32. On this graph the calculated position for the contaminant reaction $O^{16}(p,n)$ is shown at each angle. There does not seem to be significant production by the contaminant. Also indicated in Fig. 32 is the expected position for neutrons produced in the $Al^{27}(p,n)Si^{27}$ ground-state reaction. The Q for this reaction is -5.610.[16] It is apparent that this group was produced at all three angles, and quite strongly at the forward angle. The appearance of this group at the approximately correct energy lends weight to our belief that our range-energy relationship for liquid hydrogen was correct and that the ground-state transitions for the other two reactions, $Be^{9}(p,n)B^{9}$ and $N^{14}(p,n)O^{14}$, were not observed.

Because the level separation of a nucleus as heavy as Si^{27} was expected to be much smaller than the resolution of our spectrometer system, no attempt was made to interpret the structure of the energy spectra in terms of specific energy states of Si^{27}. However, aluminum contains enough nucleons to allow a compound-nucleus analysis at our bombarding energy, since the average excitation of each nucleon ($\sim$ 1 Mev) was much less than the energy necessary for a neutron to escape from the compound nucleus ($\sim$ 15 Mev). Accordingly, one could expect the energy spectrum of emitted neutrons to be given by[2]

$$I_N(E)dE = \text{Const } E\ \sigma_c(E)\ W_B(E_{max}-E)dE, \qquad (29)$$

where $I_N(E)dE$ is the probability of emitting a neutron of energy between E and E + dE, $\sigma_c(E)$ is the cross section for the inverse reaction, and $W_B(E_{max}-E)$ is the level density of the residual nucleus B at excitation energy $E_x = E_{max}-E$. By making a Taylor expansion of the logarithm of the level density around the maximum energy ($E_x = E_{max}$) by which the residual nucleus B can be excited, Blatt and Weiskopf[2] obtain an approximate expression for the level density,

$$W(E_{max}-E) = \text{const} \exp -\frac{E}{T}, \qquad (30)$$

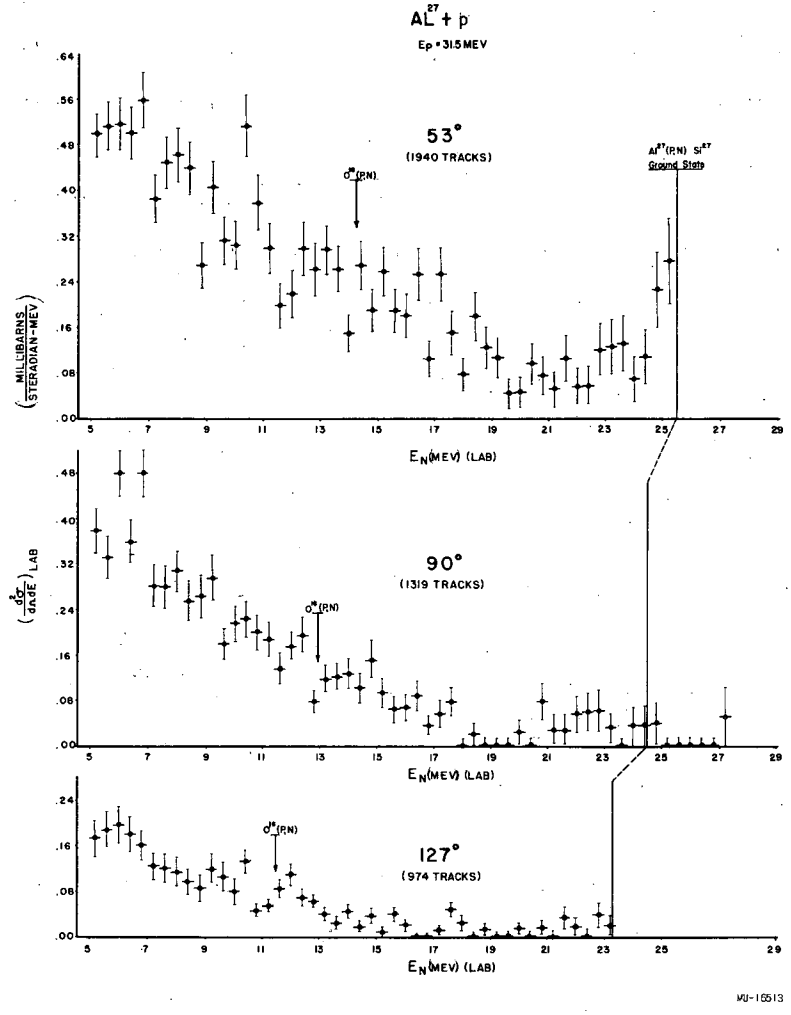

Fig. 32. Differential cross sections for the production of neutrons at 53°, 90°, and 127° (lab) by the 31.5-Mev proton bombardment of Al^{27}. Errors shown are the statistical probable errors.

where T is defined by the relationship

$$T^{-1} = \frac{d \ln W(E)}{dE} \tag{31}$$

The quantity T, which has the units of energy, can be interpreted as a nuclear "temperature", since the logarithm of the level density may be considered the entropy of the residual nucleus at excitation E.[9] Using the above formula for the level density, we can obtain the "Maxwellian" formula for the energy distribution,

$$I_n(E)dE = \text{const } E\sigma_c(E) \exp(-E/T)dE \ . \tag{32}$$

The thermodynamic analogy between T and an actual temperature has in the past been taken seriously enough to attempt to predict the dependence of T on the excitation of the nucleus where the nucleus is pictured as, say, a degenerate Fermi "gas" of nucleons. More recently, T has come to signify only the functional relationship of Eq. (31). The "temperature" T can be determined from an emission spectrum by plotting the relation $I_n(E)/E\sigma_c$ versus E on semilog paper. If the spectrum is of "Maxwellian" form, then the data will lie on a straight line whose negative inverse slope will be T. Semilog graphs of this relation for our aluminum-bombardment data at the three angles are shown in Figs. 33, 34, and 35. The energy width of the data points was doubled to 0.8 Mev in order to remove some of the structure in the spectra. The straight lines were fitted to the data between 5 and 12 Mev. The temperatures determined for the three angles were 4.3 Mev at 53°, and 3.3 Mev at both 90° and 127°. While the temperature was the same at 90° and 127°, the production of neutrons was not; the 90° yield was much larger than the 127° yield. The cross sections for the production of neutrons of energy greater than 5 Mev at the three observation angles in the laboratory system are listed in Table V; the ratio, from forward to backward angles, was approximately 5:3:2. This strong forward asymmetry is in direct contradiction to the predictions of a compound-nucleus model. Wolfenstein has shown that for high excitations of the

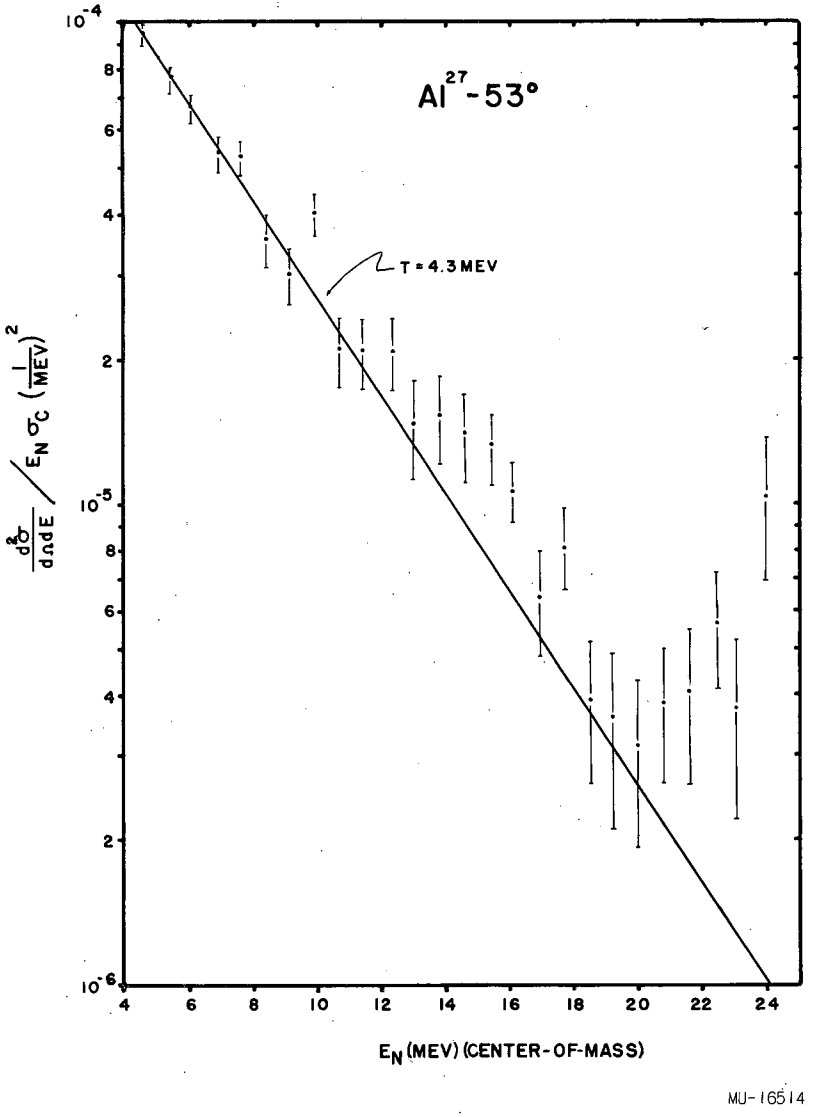

Fig. 33. Plot of $\ln (d^2\sigma/d\, dE/E_N\sigma_C$ versus neutron energy for Al^{27} at 53° (lab). Values for σ_C were taken from Blatt and Weisskopf, using a value of $R = 1.3 \times 10^{-13} A^{1/3}$ cm. Errors shown are statistical probable errors. The slope was determined from the data between 5 and 12 Mev.

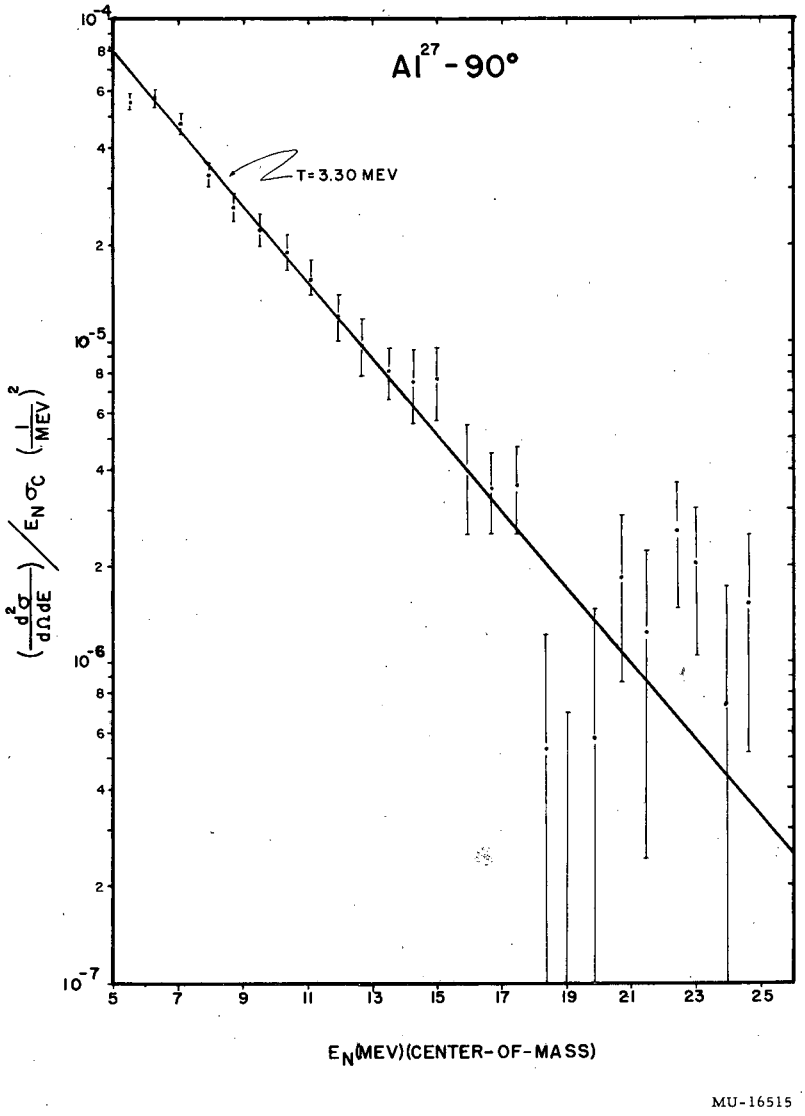

Fig. 34. Plot of $\ln (d^2\sigma/d\,dE)/E_N\sigma_C$ versus neutron energy for Al^{27} at 90° (lab). Values for σ_C were taken from Blatt and Weisskopf, using a value of $R = 1.3 \times 10^{-13} A^{1/3}$ cm. Errors shown are statistical probable errors. The slope was determined from the data between 5 and 12 Mev.

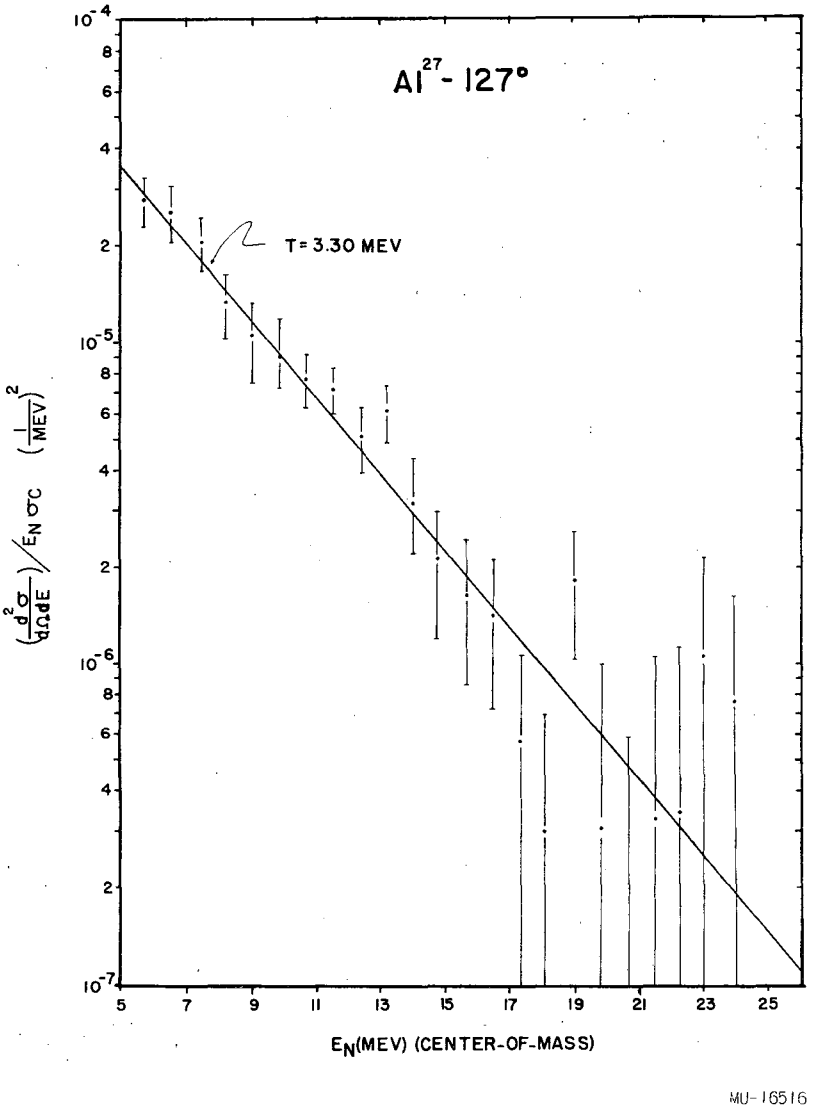

Fig. 35. Plot of $\ln (d^2\sigma/d\,dE)/E_N\sigma_C$ versus neutron energy for Al^{27} at 127° (lab). Values for σ_C were taken from Blatt and Weisskopf, using a value of $R = 1.3 \times 10^{-13} A^{1/3}$ cm. Errors shown are statistical probable errors. The slope was determined from the data between 5 and 12 Mev.

compound nucleus into a region of many overlapping levels, the angular distributions predicted by the statistical model will be symmetric about 90°.[4] The 30-Mev proton bombardment of Al^{27} leads to the compound nucleus Si^{28} excited to about 40 Mev, and hence the continuum criterion should be well satisfied. Furthermore, Hauser and Feshbach have pointed out that for high excitations of the residual nucleus, the angular distribution should be isotropic.[47] This should then be a case for the 5- to 10-Mev neutrons in this experiment, since the residual nucleus is then left with 15 to 20 Mev excitation. The spectra in Fig. 32 indicate, however, that the production is strongly peaked forward even at the lower emission energies.

It should be emphasized, however, that the (p,n) reaction is not the only possible--nor the most likely--neutron-producing reaction for the energy region we observe. Table VI lists the several possible reactions that may contribute to the spectra, along with their Q values and their 53° (lab) threshold energy. The Q values were obtained from Endt and Braams[48] or were calculated by using data from Wapstra[49] and Cameron.[50]

Table VI

Neutron-producing reactions from the proton bombardment of Al^{27}

Products of $Al^{27} + p \rightarrow$	Q (Mev)	Highest neutron energy(53°) (Mev)
$Si^{27} + n$	-5.610	25.6
$Al^{26} + p + n$	-13.049	18.0
$Mg^{23} + \alpha + n$	-14.93	16.1
$Si^{26} + 2n$	-16.27	14.7
$Mg^{25} + 2p + n$	-19.59	11.2

As can be seen in Fig. 32, the production of neutrons is peaked forward for both the region of the two-body final state (Si^{27} + n) above 18 Mev and the region of the three-body final state below 18 Mev. Hence it would appear that both types of reactions proceed primarily through a direct-interaction mechanism.

In order to compare the temperatures computed from our data with those from previous experiments on aluminum, a table given by Gugelot has been used.[51] Added to his table are the results from a 23-Mev (p, n) experiment by Cohen[14] and also the results of our work. In Table VII we have listed: the type of reaction involved; E_{max}, which was the maximum energy with which a particle can be emitted; $\Delta\epsilon$, the energy interval of the emitted particle over which T was computed; and ΔE, equal to the interval of the residual excitation energy after emission of a particle with kinetic energy in the interval $\Delta\epsilon$.

Table VII

Temperatures determined from aluminum bombardments

Reaction	E_{max} (Mev)	$\Delta\epsilon$ (Mev)	ΔE (Mev)	T (Mev)	Reference
Al(n, n)	13	1-2	12-9	1.0	13
Al(n, n)	14	1-4	13-10	1.1	52
Al(p, p)	17	5-7 8-12	12-10 9-5	1.3 2.7	51
Al)p, p)	28	10-25	18-3	3-6.5	53
Al(p, n)	11	2-5	9-6	1.3(0°)	12
Al(p, n)	17	~3	~14	1.34 (0°) 1.1 (90°) 1.05 (150°)	14
		~10	~7	2.6 (0°) 2.2 (90°) 1.9 (150°)	
Al(p, n)	25	5-12	20-13	4.3 (53°) 3.3 (90°) 3.3 (127°)	this paper

The other work in our energy region was the (p,p) reaction by Britten.[53] The temperatures listed above for this reaction must have been estimated by Gugelot,[51] since Britten did not determine them in his paper. Since his spectra contained much structure, the temperature estimates are certainly crude.

The two other (p,n) experiments on aluminum yielded lower temperatures than did our experiment, as would be expected for lower bombarding energies. However, Cohen's work indicated a higher temperature for the higher-energy neutrons leaving a less excited residual nucleus.[14] Cohen did not measure the energy spectrum but used the activation method with threshold detectors to measure the angular distribution of neutrons in two energy ranges. The temperatures were inferred from the ratio of the two angular distributions. The angular distributions measured by Cohen were peaked forward for neutron-emission energy greater than 9.5 Mev; the ratios of 53°:90°:127° intensities were approximately 6:3:2. This is quite similar to our results at our higher bombarding energy.

The temperature data in Table VII have been plotted versus the residual-nucleus excitation and also versus the emitted-particle energy in Fig. 36A and B, respectively. The statistical picture of the nucleus would predict a higher temperature for a higher excitation energy of the residual nucleus. The data, although sketchy, suggest an increase with the emitted particle energy. This could, once again, be a direct-interaction effect resulting in energy spectra that do no fall off as fast as a "Maxwellian" distribution would for the higher emission energies. Such an effect would result in higher temperatures computed from the higher-energy emitted particles.

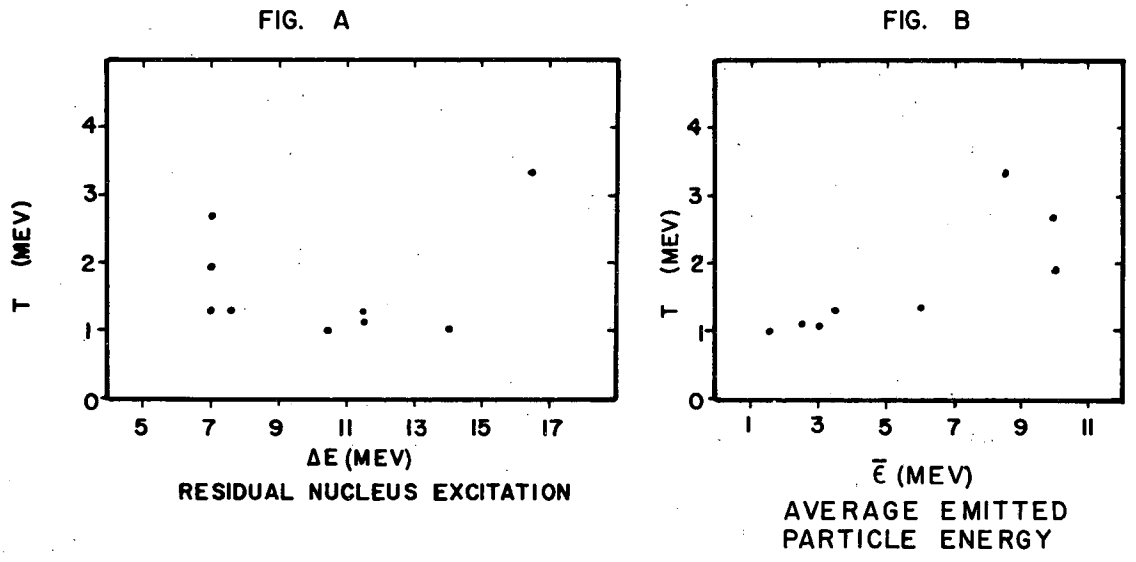

Fig. 36. A. Graph of the temperature data in Table VII for aluminum versus ΔE, the excitation of the residual nucleus (Al^{27} or Si^{27}).

B. Graph of the same data versus $\bar{\epsilon}$, the average energy of the emitted particle.

VI. SUMMARY

The neutron spectra for energies greater than 5 Mev from the 31.5-Mev proton bombardment of Be^9, N^{14}, and Al^{27} have been measured at three angles with the 4-inch hydrogen bubble chamber as a neutron spectrometer. The forward production of the emitted neutrons and the shape of the energy distribution, especially at the forward angle, seem to indicate that the important mechanism for neutron production at this energy is that of a direct-interaction type, i.e., an interaction in which the outgoing neutron is emitted before the available energy has been shared to a large degree with other nucleons in the nucleus. This appears to be true for the heaviest element bombarded, Al^{27}, for which the compound model could apply. In this case, the forward production was more than twice as large as the yield measured at our backward angle.

The energy spectra for the two lighter targets appear to indicate the existence of several new levels in the residual nuclei, O^{14} and B^9, as well as some previously observed ones. Several of the new levels that were possibly observed for the B^9 have energies in good agreement with the mirror-nucleus predictions.

The hydrogen bubble chamber, when coupled to a fast data-processing system, appears to be a useful neutron spectrometer with good resolution and high efficiency. Its usefulness will be enhanced when it is used with particle accelerators whose duty cycle is more comparable to that of the bubble chamber. It should be noted that the 4-inch chamber was not designed for neutron spectroscopy, but was actually a prototype instrument built for testing experimental features to be used in the larger bubble chambers. An instrument designed with neutron measurements in mind should have better temperature regulation and stability, less material in the immediate vicinity of the liquid hydrogen, and, if possible, a 90° stereo angle for the camera in order to obtain a more accurate reconstruction of the tracks in real space. Electronic instruments for data reduction are being developed at this laboratory which, for problems as simple as recoil-proton analysis, could obviate the need for a human reader. These systems should be able to read and analyze a stereo pair of photographs faster than the bubble chamber can go through an expansion cycle.

ACKNOWLEDGMENTS

I wish to express my sincere appreciation to Professor Burton J. Moyer for his advice and support during the course of this long experiment. Mr. Hoyt A. Bostick collaborated closely during all phases of this experiment and made a simultaneous investigation of the neutron spectra of several medium-weight elements. I am also indebted to Dr. Charles N. Waddell, who was instrumental in the planning and execution of this experiment and with whom many stimulating discussions were held.

The experiment could not have been accomplished without the aid of the Bubble Chamber Group under the direction of Professor Luis W. Alvarez; in particular, Mr. Arnold Schwemin, who was responsible for the successful operation of the 4-inch chamber during the experiment, effected several modifications in the chamber which made it suitable for use as a neutron spectrometer. As always, there was complete cooperation and helpful assistance from the linear accelerator crew under the direction of Mr. James Sirois.

A vital part of this experiment was the data-analysis equipment. Much of this equipment was designed by Mr. Arthur W. Barnes, who was also responsible for the continued operation of the OSCAR. The tedious job of reading the film was carried out by Dr. Graham P. Conroy, Dr. Farhang Zabee, Miss Betty Blaine, Mr. Robert Brians, Mr. James Peck, and Mr. William Wadman. I would also like to thank Mr. Kent Curtis, who wrote the initial IBM-650 program and who was always helpful in providing me with information about programming techniques.

This work was done under the auspices of the U.S. Atomic Energy Commission.

APPENDICES

A. Multiple-Scattering Effects on the $H^3(d, n)He^4$ Neutron Spectrum

Because of the necessity of degrading the energy of the incident deuterons from 4 Mev down to 2 Mev in order to insure that the deuterons would stop in the tritium-titanium target, a 36.7-mg/cm^2 gold foil was placed in front of the target. The direction of the incident deuterons passing through this foil could be changed by multiple Coulomb scattering. In order to calculate the effects of this Coulomb scattering on the resultant neutron spectrum, it was necessary to calculate the following quantities:

1. The mean-square projected scattering angle for the gold and tritium-titanium.
2. The energy loss of deuterons in tritium-titanium from 2 Mev down to zero energy.
3. The relative yield of neutrons as a function of deuteron energy for the $H^3(d, n)He^4$ reaction.

It was the projection of the mean-square scattering angle $\overline{\theta^2}$ on the plane determined by the beam line and the neutron collimator axis that measured the distortion of the neutron spectrum, since the bubble chamber detected neutrons at only one azimuthal scattering angle. The projection of the mean-square scattering angle $\overline{\theta_p^2}$ is related to the mean-square scattering angle $\overline{\theta^2}$ by[54]

$$\overline{\theta^2}_p = 1/2\ \overline{\theta^2} \quad . \tag{A-1}$$

Since the foils were rather thick, it was necessary to divide the target into many layers and calculate the mean-square scattering angle $\overline{\theta_i^2}$ for each energy bite $E_i + dE$. We then took, for the total mean-square angle $\overline{\theta^2}$,[55]

$$\overline{\theta^2} = \sum_i \overline{\theta^2}_i \quad , \tag{A-2}$$

where

$$\overline{\theta^2}_i = \frac{2\pi Z^2 (m Y_0)^2 d_i}{A E_i^2} \ln \frac{E_i}{m a^2 Z^{4/3}} \quad , \tag{A-3}$$

where

Z = charge of target nucleus,

m = rest energy of electron, in Mev,

Y_0 = classical radius of electron,

α = fine-structure constant,

d_i = areal density of ith layer of target,

E_i = energy of deuteron in ith layer.

For gold we had, therefore,

$$\overline{\theta^2}_i(\mathrm{Au}) = 2.463 \frac{d_i}{E_i^2} \ln (109.4\, E_i) , \qquad \text{(A-4)}$$

and for titanium,

$$\overline{\theta^2}_i(\mathrm{Ti}) = 0.7840 \frac{d_i}{E_i^2} \ln (595.0\, E_i) . \qquad \text{(A-5)}$$

The gold target was treated in eight layers, each of deuteron-energy decrease of 0.25 Mev. In order to find the areal density of each layer, the stopping power of gold was approximated by that for lead as given in Aron et al.[33] It was found that the mean-square scattering angle of the deuterons after being degraded from 4 Mev to 2 Mev by the gold target was $14^\circ\ 10'$, and hence the projected angle was 10°.

In order to make a similar calculation for tritiated titanium, it was necessary to determine the rate of energy loss of deuterons from 2 Mev to zero energy. Empirical data in this energy range were given by Allison and Warshaw for hydrogen, aluminum, and copper.[56] By use of a method outlined in a paper by Benveniste and Zenger,[57] the stopping power of tritium-titanium was calculated for a ratio of tritium to titanium of 0.787. The result of this calculation of the stopping power is shown in Fig. 37.

With the use of the latter data and with Eq. (A-5), the mean-square scattering angles for deuterons in tritium-titanium were computed by dividing the target into nineteen layers, of 0.2-Mev thickness from 2 Mev to 1 Mev, of 0.1-Mev thickness from 1 Mev to 0.4 Mev, and of 0.05-Mev thickness from 0.4 Mev to 0 Mev. The result in the form of the projected root-mean-square scattering angle versus deuteron energy is shown in Fig. 38.

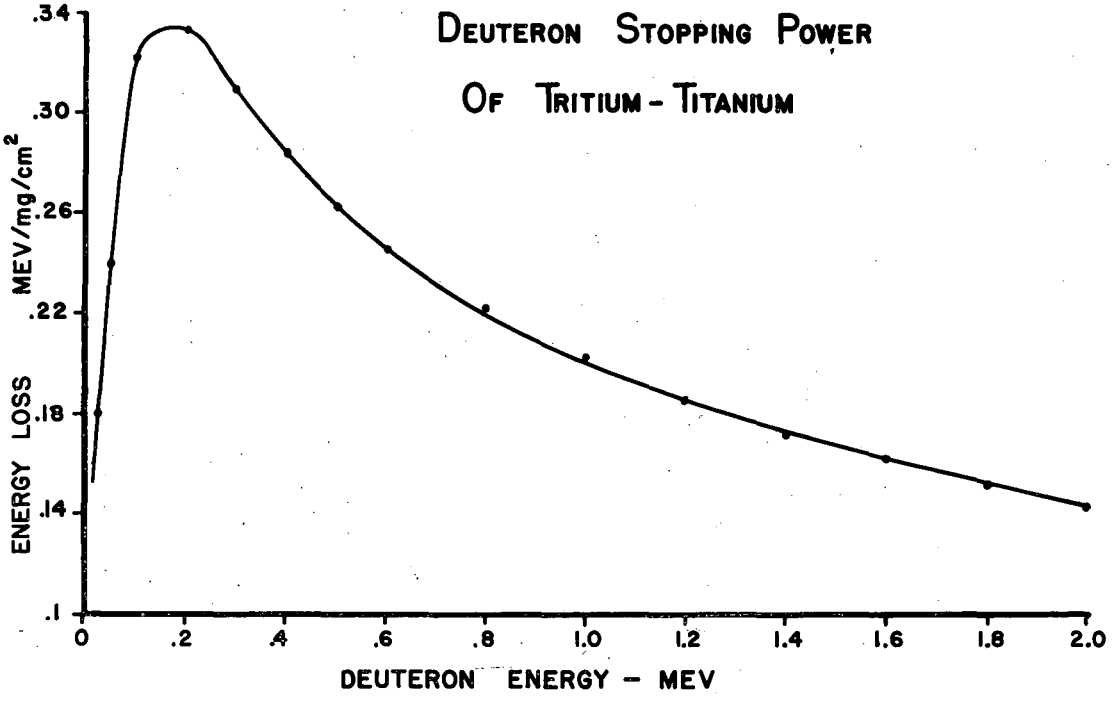

Fig. 37. Stopping power of tritium-titanium (0.787 ratio) for deuterons.

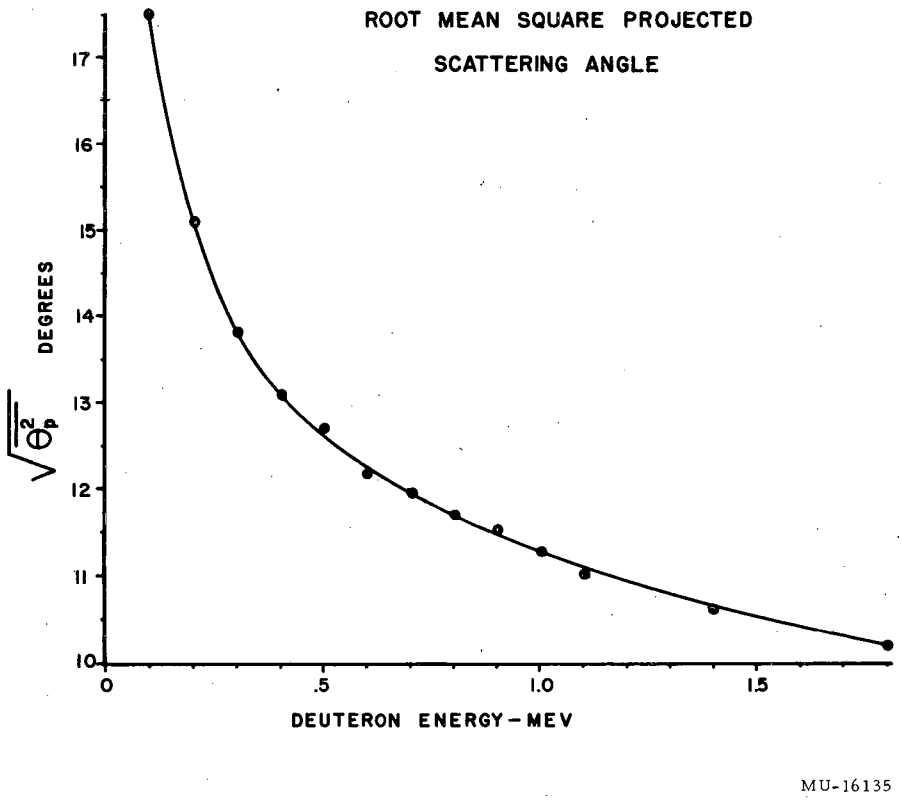

Fig. 38. Root-mean-square projected scattering angle for deuterons in tritium-titanium.

The stopping-power curve for tritium-titanium was also used with the data for the $H^3(d, n)He^4$ cross section as given by Fowler and Brolley[32] to calculate the relative yield of neutrons as a function of deuteron energy for our tritium-titanium target. This curve is shown in Fig. 39.

In the calculation of the source spectrum, it was assumed that in the ith layer, where the projected mean-square scattering angle was $\overline{\theta^2}_{ip}$, the deuteron distribution was described by:

$$P_i(\theta_p)d\theta_p = \frac{1}{\sqrt{2\pi}} \exp - \frac{\theta_p^2}{\overline{\theta^2}_{ip}} \qquad \text{(A-6)}$$

Fowler and Brolley's report also contained a tabulation of the neutron lab energy versus deuteron lab energy and angle for the $H^3(d, n)He^4$ reaction.[32] Angular bites for the ith level corresponding to deuteron energy E_i and a neutron energy width of 0.2 Mev were determined from this table. The relative number of deuterons in each angular bite was then determined from the distribution given in Eq. (A-6). The product of this number and the cross section for the reaction at this energy gave the relative number of neutrons produced in the corresponding energy band. By repeating this process for 13 layers of the tritium-titanium target, and summing the yields of neutrons in each energy band, a source spectrum of neutrons emitted at 90° from the deuteron beam was obtained. This curve, which is shown in Fig. 17 (Curve B), indicates that the effect of multiple scattering of the deuterons in the gold foil and target caused the source spectrum to have a full width at half maximum of 0.6 Mev instead of 0.1 Mev (Fig. 17, Curve A).

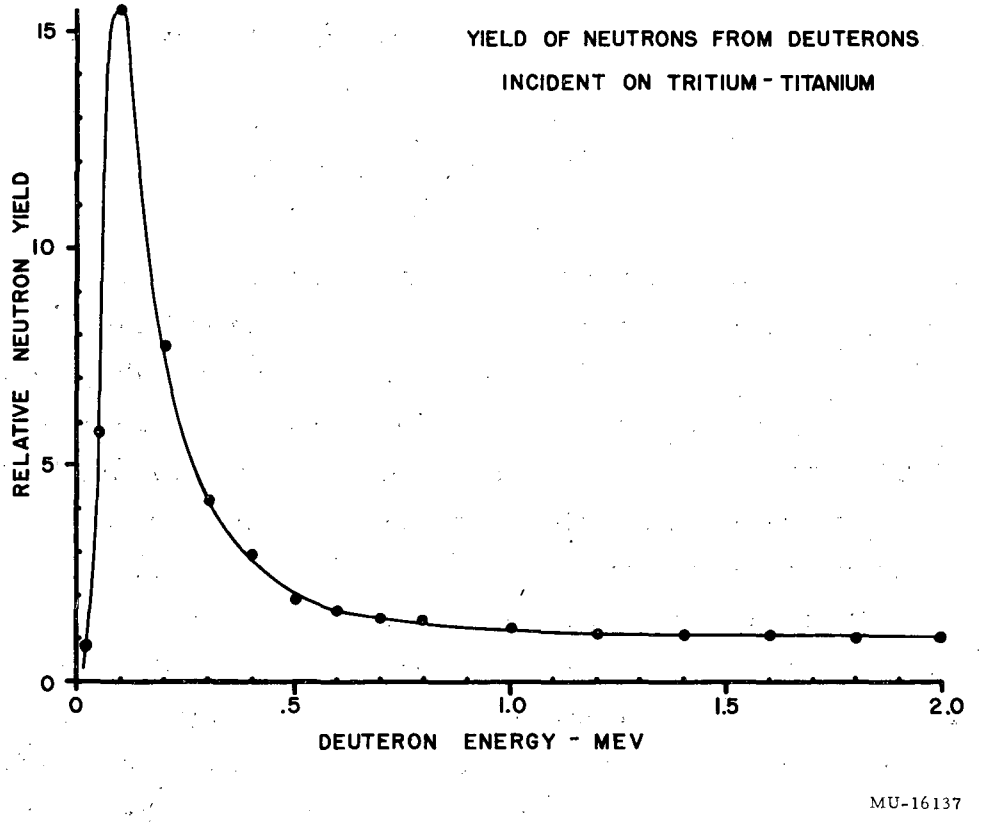

Fig. 39. Calculated relative yield of neutrons as a function of deuteron energy within a tritium-titanium target.

B. Reconstruction of Tracks from Measurement of Stereo Pictures

The three-dimensional position of a point in the hydrogen bubble chamber was represented in our stereo pictures by two two-dimensional projected points. This section outlines the calculation that was made by the IBM 650 in order to determine the length and angle of a track in real space from the coordinate information on the master and track cards.

Figure 40 is a sketch of the optical geometry of the chamber. The twin lenses of the stereo camera were mounted vertically and were parallel. Their centers were separated by a distance ΔL equal to 3.5 inches. The lenses were approximately 18 inches from the front surface of the hydrogen. The coordinate system that was used had X as the axis through the two lenses, Y as the direction of the incoming neutron, and Z as the axis parallel to the lens axis. The origin of this axis system was chosen so that the fiducial mark I on the inner surface of the front glass of the bubble chamber had the real-space coordinates 2.54 cm, 2.54 cm, 0. The Z axis therefore measured the depth into the chamber from the front glass to the back glass. In this system the top lens had the coordinates X_T, Y_T and the bottom lens had the coordinates X_B, Y_B, where $Y_B = Y_T$.

Consider a point r in the chamber whose real-space coordinates were X_r, Y_r, Z_r. As shown in Fig. 40, Lens T (top lens) would see the projected X value of X_{rT}; Lens B would observe X_{rB}; X_r would lie somewhere between X_{rT} and X_{rB}. Similarly Lens T would observe the projected Y value as Y_{rT}. Lens B would observe the same Y projection coordinate as Lens T, and hence would give no new information about the Y coordinate.

In Fig. 40, we see that because of refraction a reconstruction of the Z position from X_{rT} and X_{rB} would be in error and would give us the value ξ_r. However, it was assumed that this refractive effect would be linear, and a correction was made for it based on the apparent depth ξ_p of a point p in the chamber whose real depth Zp was known.

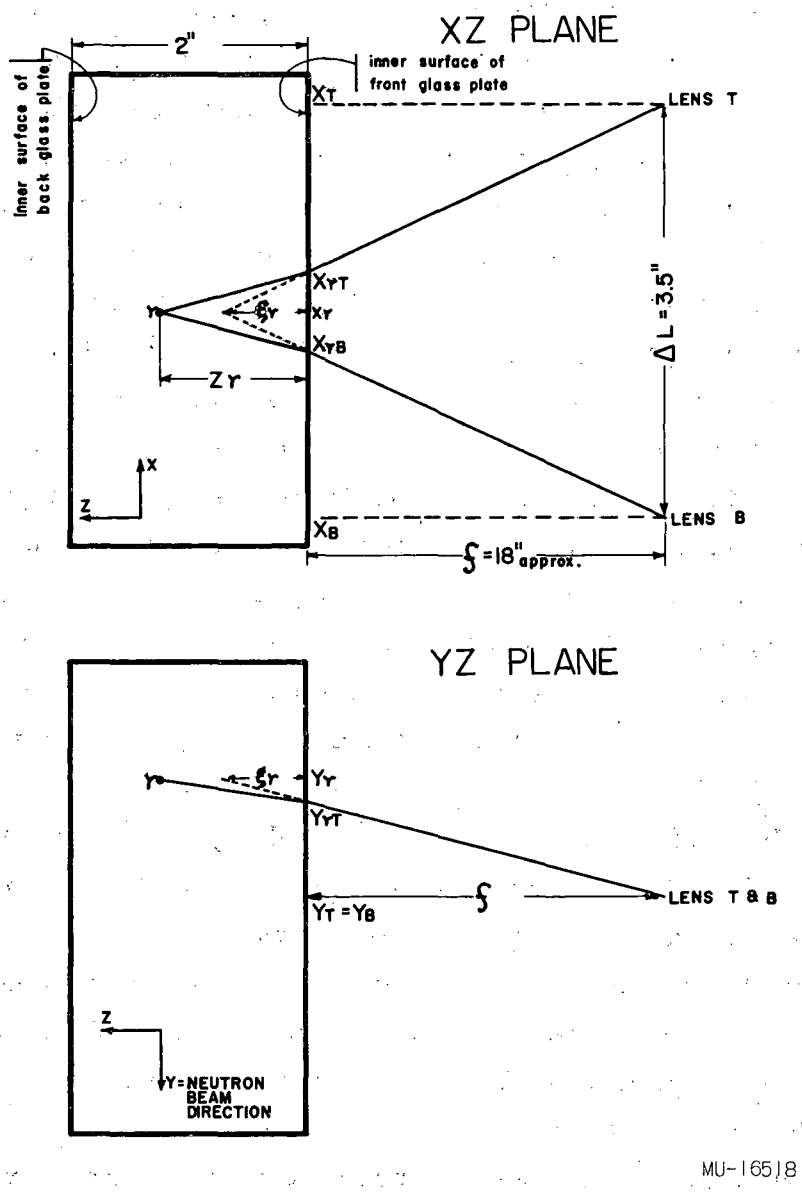

Fig. 40. Optical geometry of the two-lens stereo photography system used with the 4-inch bubble chamber.

Simple plane geometry was used to find the X_r, Y_r, and ξ_r from the measured projected coordinates X_{rT}, X_{rB}, and Y_{rT}. Thus X_r could be found from the relationship

$$X_r = R(X_{rT}\,\Delta L - X_T\,\Delta X_r), \tag{B-1}$$

where

$$L = X_T - X_B,$$

$$X_r = X_{rT} - X_{rB},$$

$$R = \frac{1}{\Delta L - \Delta X_r}.$$

Also ξ_r, the apparent depth in the chamber, was given by

$$\xi_r = f\Delta X_r\,\Delta R, \tag{B-2}$$

where

f = distance from lenses to chamber.

Knowing ξ_r, one could now find Y_r,

$$Y_r = \frac{\xi_r}{f}(Y_{rT} - Y_T) + Y_{rT}. \tag{B-3}$$

Finally, Z_r could be found from

$$Z_r = G_z\,\xi_r, \tag{B-4}$$

where G_z was determined in the following way. A point in the chamber whose real-space position was well known was measured. The point p chosen was a fiducial mark on the inner surface of the back glass whose Z coordinate was known to be 2.54 cm (the distance between the two glass plates). By applying our equations, we found the ξ_p that corresponded to this known Z_p and hence determined G_z. This Z "magnification factor" resulting from refraction was then used in the determination of the Z coordinate of any point in the chamber.

Four other magnification factors were also used in the calculation. They were necessary because the reader was measuring an image projected to four times its actual size. These four magnification factors corresponded to the expansion of the X and Y scales in the top and bottom views. They were determined from a measurement of the separation of the fiducial marks as projected on the OSCAR screen. This method removed differences in magnification between the stereo projection lenses.

It was now easy to calculate the pertinent characteristics of a track. Suppose we had a track rs, where r was the beginning of the proton recoil and s was the end. By the above method we could determine $X_r Y_r Z_r$ and $X_s Y_s Z_s$. Acceptance criteria for the track were now applied. Since the track had to begin within the "sensitive volume" cylinder, the following relationship had to hold for an accepted track:

$$(X_r - a)^2 + (Z_r - c)^2 \leq R^2 , \qquad \text{(B-5)}$$

where a, c, and R defined the axis and diameter of the cylinder. If this relationship was not satisfied, the track was rejected and a new track was computed. Since a track had to end before a certain plane in the chamber, we had

$$Y_s \leq E, \qquad \text{(B-6)}$$

where E defined the end of the sensitive-volume cylinder. If this criterion was not satisfied, the computation would continue, but the track answer card would contain a specific rejection code number. The IBM 650 could now determine the length, l, from

$$l = \sqrt{(X_s - X_r)^2 + (Y_s - Y_r)^2 + (Z_s - Z_r)^2} . \qquad \text{(B-7)}$$

The corresponding proton energy, E_p, was determined from the range l of the track from a range-energy table inserted into the IBM 650 memory. The polar angle, θ, was determined from

$$\cos \theta = \frac{Y_s - Y_r}{l} . \qquad \text{(B-8)}$$

A track was rejected for energy spectra if θ was greater than 30^{o}. Such a track would be completely computed, but its track answer card would contain a specific rejection code number. The azimuthal angle, ϕ, was computed from

$$\tan \phi = \frac{X_s - X_r}{Z_s - Z_r} . \qquad \text{(B-9)}$$

Finally, the energy E_n of the incident neutron was calculated from

$$E_n = \frac{E_p}{\cos^2 \theta} .$$

The quantities 1, E_p, θ, ϕ, E_n, and $d = Y_r$ were part of the output of the IBM 650 and were punched onto an IBM card. Since d represented the Y coordinate of the start of the recoil track, it was possible to change the effective length of the sensitive-volume cylinder during the compilation of the energy spectra if it were so desired.

C. Calculation of the Efficiency Correction

In calculating the absolute efficiency of the bubble chamber as a neutron detector, we considered the variation of the n-p cross section with energy, the decrease of the neutron flux in passage through the hydrogen, the acceptance of recoils no greater than 30°, and the loss of recoils because they ended beyond the limits of the sensitive volume (plane KL in Fig. 22).

Figure 41 is a sketch of the cross section of the sensitive-volume cylinder. We considered a beam of N_0 neutrons of energy E_n impinging on the front (left) of the sensitive-volume cylinder. We divided the cylinder into two sections. Section 2 had a length $R(0^{\circ}, E_n)$ equal to the range of a 0° proton recoil, i.e., a proton of energy E_n equal to the energy of the incident neutron. Thus from Eq. (10) we have

$$R(0^{\circ}, E_n) = a\, E_n{}^{x}, \qquad \text{(C-1)}$$

where R is in centimeters, E_n is in Mev, $a = 0.0126$, and $x = 1.84$. Because the length of Section 2 was chosen in this way, any recoil originating in Section 1 from a neutron of energy E_n would end before line KL and would not be rejected for this reason.

The steps of this calculation were:

1. Consider a given neutron energy E_n and divide the sensitive volume into two parts: Section 1 of length L-R; and Section 2 of length R, where $R \equiv R(0^{\circ}, E_n)$.
2. Calculate the efficiency of Section 1, considering the probability of the formation of a proton recoil and the rejection of recoils at angles greater than 30°.
3. Calculate the efficiency of Section 2 by determining, in addition to the above two considerations, the additional loss of tracks because of extension beyond the end of the chamber.

The number of recoils that would occur in Section 1 because of the incidence of N_0 neutrons of energy E_n was $N_0(E_n)\ \left[1-\exp-(L-R)/\lambda\right]$, where $\lambda(E_n) = 1/d\,\sigma_T(E_n)$ is the neutron mean free path, $\sigma_T(E_n)$ is the total n-p cross section for neutrons of energy E_n, and d is the density

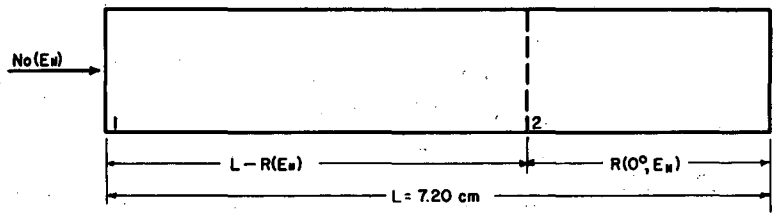

Figure A

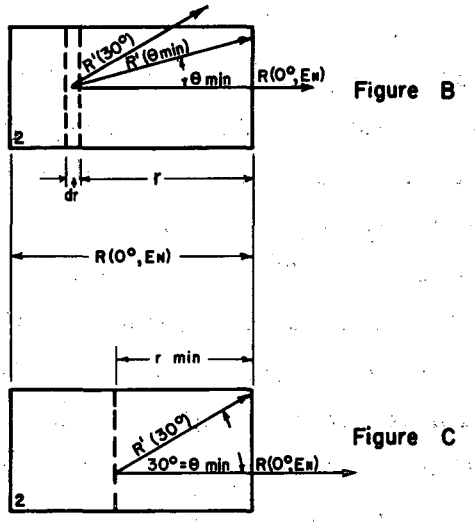

Figure B

Figure C

MU-16519

Fig. 41. Diagrams of the acceptable "sensitive volume" of the bubble chamber, illustrating the calculation of the efficiency of the spectrometer.

of liquid hydrogen. The data for $\sigma_T(E_n)$ were taken from Hughes and Harvey.[58] Of this total number of recoils, only those of angle less than 30^o were accepted for the spectra. The fraction, F_{30^o}, of recoils at angles less than 30^o was given by

$$F_{30^o}(E_n) = \frac{\int_{0^o}^{30^o} \frac{d\sigma}{d\theta}(E_n)\, d\theta}{\int_{0^o}^{90^o} \frac{d\sigma}{d\theta}(E_n)\, d\theta} , \qquad (C\text{-}2)$$

where $d\sigma/d\theta(E_n)$ is the n-p differential scattering cross section in the laboratory system. At energies less than 10 Mev the n-p scattering is isotropic in the center-of-mass system and hence $d\sigma/d\theta \sim \sin 2\theta$. For this case, $F_{30^o} = 0.25$, i.e., one-fourth of all recoils were at angles less than 30^o and hence were accepted.

However, at energies greater than 10 Mev, the c.m. scattering becomes increasingly anisotropic. For this region, Gammel has constructed a semiempirical formula based on interference of S and D waves.[19] The interference term should vary as E^2 and approach the measured value at 90 Mev. The resulting formula for the laboratory-system differential scattering cross section at lab. angle θ is

$$\frac{d\sigma}{d\theta}(\theta, E_n) = \sigma_T(E_n) \sin 2\theta \left\{ \frac{1 + 2\left(\frac{E_n}{90}\right)^2 \cos^2 2\theta}{1 + 2/3\left(\frac{E_n}{90}\right)^2} \right\} . \qquad (C\text{-}3)$$

The term in brackets is the correction to the low-energy differential scattering. By using Eq. (C-3), we get

$$F_{30^o}(E_n) = \frac{6 + 7\left(\frac{E_n}{90}\right)^2}{24 + 16\left(\frac{E_n}{90}\right)^2} . \qquad (C\text{-}4)$$

At 10 Mev, this relationship gave a value for $F_{30^o}(10\ \text{Mev})$ that was less than 1% greater than 0.25. At 25 Mev, $F_{30^o}(25\ \text{Mev})$ was only 4% greater than 0.25.

Finally, the number $n_1(E_n)$ of acceptable recoils produced in Section 1 by N_0 neutrons of energy E_n was

$$n_1(E_n) = N_0(E_n)\ (1-\exp-(L-R)/\lambda)F_{30^o}(E_n). \qquad (C-5)$$

We then calculated the number $n_2(E_n)$ of acceptable recoils generated in Section 2 because of the $N_0 \exp -(L-R)/\lambda$ neutrons that had survived passage through Section 1. Figure 41 (B and C) illustrates the r coordinate system that was set up to measure distance in Section 2 from the end of Section 2. Consider a recoil track produced in some element dr at r (Fig. 40 B). If the track went straight forward, it would end beyond Section 2 and would be rejected. In fact it would be rejected unless it recoiled at an angle greater than the angle θ_{min}, where θ_{min} was a function of r and was given by

$$\theta_{min} = \arccos \left(\frac{r}{R}\right)^{\left(\frac{1}{2x+1}\right)} \qquad (C-6)$$

Equation (C-6) follows from the relationships

$$R'(\theta_{min}) = aE^x{}_p(\theta_{min}) = a(E_n \cos^2\theta_{min})^x = R(\cos\theta_{min})^{2x}$$

and

$$\frac{r}{R'(\theta_{min})} = \cos\theta_{min},$$

where $R'(\theta_{min})$ is the range of a recoil proton at angle θ_{min}.

Since the track would also be rejected if its angle were greater than 30^o, it was necessary to find the fraction $F_{30^o}(r, E_n)$ of recoils generated at r in dr that would lie between $\theta_{min}(r)$ and 30^o. This was given by

$$F_{30^o}(r, E_n) = \frac{\int_{\theta_{min}(r)}^{30^o} \frac{d\sigma}{d\theta}(E_n)\, d\theta}{\int_{0^o}^{90^o} \frac{d\sigma}{d\theta}(E_n)\, d\theta}, \qquad \text{(C-7)}$$

where $d\sigma/d\theta$ was given by Eq. (C-3). The number of recoils generated in dr at r was $N_0 \left[\exp - (L-R)/\lambda\right] dr/\lambda$. The number of acceptable recoils generated in dr was therefore $N_0 \left[\exp -(L-R)/\lambda\right] \times F_{30^o}(r, E_n)\, dr/\lambda$. The total number of acceptable recoils generated in Section 2 was then

$$n_2(E_n) = \frac{N_0}{\lambda} \int_{r_{min}}^{R} \left[\exp - (L-R)/\lambda\right] F_{30^o}(r, E_n)\, dr. \qquad \text{(C-8)}$$

The lower limit of r_{min} was used instead of 0 because at $r = r_{min}$, $\theta_{min} = 30^o$. Hence, between $r = 0$ and $r = r_{min}$ no acceptable tracks were produced. This is shown in Fig. 41C. The determining condition for r_{min} was

$$r_{min} = R\, (\cos 30^o)^{2x+1}.$$

The total number of acceptable recoils produced in the sensitive-volume cylinder from N_0 neutrons of energy E_n impinging on it was given by

$$n(E_n) = n_1(E_n) + n_2(E_n). \qquad \text{(C-9)}$$

The absolute efficiency $\varepsilon(E_n)$ for detecting neutrons of energy E_n was therefore

$$\varepsilon(E_n) = n(E_n)/N_0(E_n) = \left\{1 - \exp -(L - R(E_n))/\lambda(E_n)\right\} F_{30^o}(E_n)$$
$$+ \lambda(E_n)^{-1} \exp -L/\lambda(E_n) \int_{r_{min}}^{R} \left[\exp r/\lambda(E_n)\right] F_{30^o}(r, E_n)\, dr. \qquad \text{(C-10)}$$

The integral was evaluated by expanding the exponential into a power series (four terms were sufficient) and integrating each term. If one neglected the exponential decrease of the flux in Section 2 in this calculation the integration could be easily carried out and the result would be in error by 2% at 25 Mev and less at lower energies. The efficiency factor $\mathcal{E}$ was evaluated as a function of neutron energy, and the raw energy spectra were corrected in an IBM 650 calculation by a factor of $1/\mathcal{E}(E_n)$ in order to get the source spectra. Figure 23 is a graph of the absolute efficiency versus neutron energy as calculated from Eq. (C-10).

REFERENCES

1. N. Bohr, Nature 137, 344 (1936).
2. J.M. Blatt and V.F. Weiskopf, Theoretical Nuclear Physics (Wiley, New York, 1952).
3. V.F. Weiskopf, Phys. Rev. 52, 295 (1937).
4. L. Wolfenstein, Phys. Rev. 82, 690 (1951).
5. Eisberg, Gugelot, and Porter (Eds.), Statistical Aspects of the Nucleus, BNL-331, April 1955.
6. B.L. Cohen, Phys. Rev. 92, 1245 (1953).
7. Cohen, Newman, Charpie, and Handley, Phys. Rev. 94, 620 (1954).
8. B.L. Cohen and E. Newman, Phys. Rev. 99, 718 (1955).
9. Cohen, Newman, and Handley, Phys. Rev. 99, 723 (1955).
10. E.B. Paul and R.L. Clarke, Can. J. Phys. 31, 267 (1953).
11. B.L. Cohen, Phys. Rev. 108, 768 (1957).
12. P.C. Gugelot, Phys. Rev. 81, 51 (1951).
13. E. Graves and L. Rosen, Phys. Rev. 89, 343 (1953).
14. B.L. Cohen, Phys. Rev. 98, 49 (1955).
15. D.M. Thomson, Proc. Phys. Soc. (London) A69, 447 (1956).
16. Austern, Butler, and McManus, Phys. Rev. 92, 350 (1953).
17. S.T. Butler, Proc. Roy. Soc. (London) A208, 559 (1951).
18. F. Ajzenberg and T. Lauritsen, Revs. Modern Phys. 27, 77 (1955).
19. C.H. Johnson and C.C. Trail, Rev. Sci. Instr. 27, 468 (1950).
20. F.L. Ribe and J.D. Seagrave, Phys. Rev. 94, 934 (1954).
21. Bame, Haddad, Perry, and Smith, Rev. Sci. Instr. 28, 997 (1957).
22. Marshall R. Cleland, An Evaluation Study of a Fast Neutron Spectrometer, NBS-2036, Oct. 1952.
23. George P. Millburn, Neutron Yields from Thick Targets Bombarded by 18- and 32-Mev Protons (thesis), UCRL-3320, Feb. 1956; Tai, Millburn, Kaplan, and Moyer, Phys. Rev. 109, 2086 (1958).
24. We are indebted to Mr. Daniel O'Connell of this laboratory for the preparation of the evaporated melamine target.
25. Chemical analysis indicated that the melamine target was 65.05% nitrogen (by weight) instead of the expected 66.7%. The difference was attributed to an acrylic which was sprayed on the foil before stripping in order to give it strength.

26. Charles N. Waddell, Gamma Transitions from the 15-Mev Level in C^{12} (thesis), UCRL-3901, August 1957.

27. Harry C. Dittler and Thomas F. Gerecke, Liquid Hydrogen Bubble Chambers (thesis), UCRL-2985, May 1955.
D. Parmentier and P. Schwemin, Rev. Sci. Instr. 26, 954 (1955).

28. Dudley B. Chelton and Douglas B. Mann, Cryogenic Data Book, UCRL-3421, May 1956.

29. John L. Need, The Mechanism of the Reaction $C^{12} + p \rightarrow p + 3\alpha$ at 32 Mev (thesis), UCRL-2806, Dec. 1954.

30. Linlor, Kerns, and Mark, Rev. Sci. Instr. 28, 535 (1957).

31. The tritium-titanium target was prepared by, and kindly loaned to us by, Mr. Jack K. Hum of the UCRL, Livermore.

32. J.L. Fowler and J.E. Brolley, Jr., Revs. Modern Phys. 28, 117 (1956).

33. Aron, Hoffman, and Williams, Range-Energy Curves, AECU-663 1949.

34. M. Lynn Stevenson, "Estimated Density of Superheated Normal Liquid Hydrogen", UCRL Engineering Note M13A, Dec. 12, 1956.

35. F. Ajzenberg and W. Franzen, Phys. Rev. 94, 409 (1954).

36. Sherr, Muether, and White, Phys. Rev. 75, 282 (1949).

37. R. Scherr and J.B. Gerhart, Phys. Rev. 91, 909 (1953).

38. J.R. Penning and F.A. Schmidt, Bull. Am. Phys. Soc. 29, No. 1, 42 (1954).

39. Bromley, Almqvist, Gove, Litherland, Paul, and Ferguson, Phys. Rev. 105, 957 (1957).

40. E.P. Wigner, Phys. Rev. 51, 106 (1937).

41. D.R. Inglis, Revs. Modern Phys. 25, 390 (1953).

42. T. Lauritsen and F. Ajzenberg-Selove, "Energy Levels of the Light Nuclei," American Institute of Physics Handbook (McGraw-Hill, New York, 1957), in Ch. 8, p. 56.

43. F. Ajzenberg and W.W. Buechner, Phys. Rev. 91, 674 (1953).

44. Marion, Bonner, and Cook, Phys. Rev. 100, 91 (1955).

45. D. Kurath, Phys. Rev. 101, 216 (1956).

46. R.G. Summers-Gill, Phys. Rev. 109, 1591 (1958).

47. W. Hauser and H. Feshbach, Phys. Rev. 87, 366 (1952).
48. P.M. Endt and C.M. Braams, Revs. Modern Phys. 29, 683 (1957).
49. A.H. Wapstra, Physica 21, 367 (1955).
50. A.G.W. Cameron, A Revised Semi-Empirical Mass Formula, CRP-690, 1957.
51. P.C. Gugelot, Phys. Rev. 93, 425 (1954).
52. B.G. Whitmore and G.E. Dennis, Phys. Rev. 84, 296 (1951).
53. R. Britten, Phys. Rev. 88, 283 (1952).
54. B. Rossi, High Energy Particles (Prentice-Hall, New York, 1952).
55. Orear, Rosenfeld, and Schluter, Nuclear Physics, Revised Ed. (University of Chicago Press, Chicago, 1953).
56. S.K. Allison and S.D. Warshaw, Revs. Modern Phys. 25, 779 (1953).
57. Jack Benveniste and Jerry Zenger, Information on the Neutrons Produced in the $H^3(d,n)He^4$ Reaction, UCRL-4266, Jan. 1954.
58. D.J. Hughes and J.A. Harvey, Neutron Cross Sections, BNL-325, July 1955.